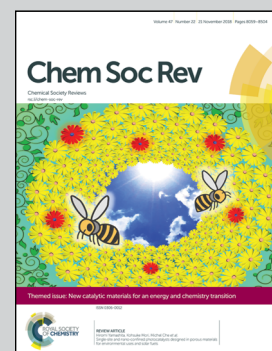


Featuring work from the research groups of Prof. Kwangyeol Lee (Korea University and Institute for Basic Science) and Prof. Sang Hoon Joo (Ulsan National Institute of Science and Technology), Republic of Korea.

Hollow nanoparticles as emerging electrocatalysts for renewable energy conversion reactions

Hollow structured nanocatalysts show great potential as next generation electrocatalysts for future renewable and sustainable energy conversion technologies.

## As featured in:



See Sang Hoon Joo,  
Kwangyeol Lee et al.,  
*Chem. Soc. Rev.*, 2018, **47**, 8173.



Cite this: *Chem. Soc. Rev.*, 2018,  
47, 8173

## Hollow nanoparticles as emerging electrocatalysts for renewable energy conversion reactions

Jongsik Park, †<sup>a</sup> Taehyun Kwon, †<sup>ab</sup> Jun Kim, †<sup>ab</sup> Haneul Jin, †<sup>ab</sup> Ho Young Kim, <sup>c</sup> Byeongyoon Kim, <sup>ab</sup> Sang Hoon Joo \*<sup>c</sup> and Kwangyeol Lee \*<sup>ab</sup>

While the realization of clean and sustainable energy conversion systems primarily requires the development of highly efficient catalysts, one of the main issues had been designing the structure of the catalysts to fulfill minimum cost as well as maximum performance. Until now, noble metal-based nanocatalysts had shown outstanding performances toward the oxygen reduction reaction (ORR), oxygen evolution reaction (OER), and hydrogen evolution reaction (HER). However, the scarcity and high cost of them impeded their practical use. Recently, hollow nanostructures including nanocages and nanoframes had emerged as a burgeoning class of promising electrocatalysts. The hollow nanostructures could expose a high proportion of active surfaces while saving the amounts of expensive noble metals. In this review, we introduced recent advances in the synthetic methodologies for generating noble metal-based hollow nanostructures based on thermodynamic and kinetic approaches. We summarized electrocatalytic applications of hollow nanostructures toward the ORR, OER, and HER. We next provided strategies that could endow structural robustness to the flimsy structural nature of hollow structures. Finally, we concluded this review with perspectives to facilitate the development of hollow nanostructure-based catalysts for energy applications.

Received 27th April 2018

DOI: 10.1039/c8cs00336j

rsc.li/chem-soc-rev

<sup>a</sup> Department of Chemistry, Korea University, Seoul 02841, Republic of Korea.

E-mail: kylee1@korea.ac.kr

<sup>b</sup> Center for Molecular Spectroscopy and Dynamics, Institute for Basic Science (IBS), Seoul 02841, Republic of Korea

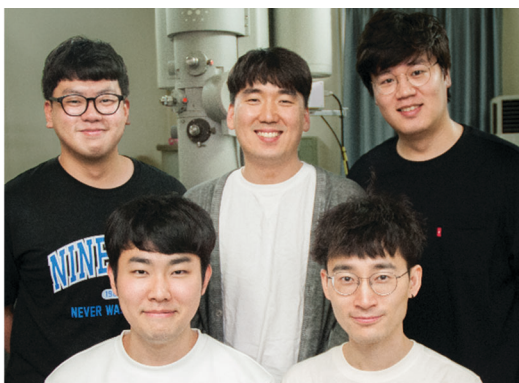
<sup>c</sup> School of Energy and Chemical Engineering, Ulsan National Institute of Science and Technology (UNIST), 50 UNIST-gil, Ulsan 44919, Republic of Korea.

E-mail: shjoo@unist.ac.kr

† These authors contributed equally.

## 1. Introduction

Global warming and climate change issues arising from fossil fuel usage pose formidable challenges to the preservation of the already fragile global eco-system and the maintenance of human quality of life.<sup>1,2</sup> These environmental issues, coupled with the ever-increasing global energy needs, call for the development of



Front line: Taehyun Kwon, Jun Kim; Back line: Dr Jongsik Park, Haneul Jin, Byeongyoon Kim (from left to right)

water splitting reaction mechanism on the heterogeneous catalyst surfaces. B. K. focuses on the development of functional nanomaterials for electrocatalytic water splitting and biomedical applications.

Jongsik Park received his PhD degree in inorganic chemistry from Korea University (South Korea) in 2018. Since March 2018, he has been working as a post-doc researcher at Korea University. His current research interests include the rational synthesis of asymmetric heterostructures and functional nanomaterials for energy conversion.

Taehyun Kwon, Jun Kim, Haneul Jin, and Byeongyoon Kim are currently pursuing their PhD degree under the supervision of Prof. Kwangyeol Lee in the Department of Chemistry, Korea University. T. K. is interested in the design of nanostructured catalysts and their potential applications in electrolytic water splitting and CO<sub>2</sub> conversion. J. K. is interested in designing functional nanomaterials based on non-noble metals for energy conversion/storage and plasmonics. H. J. is interested in the development of synthetic methods for phase-controlled nano-catalysts and investigation of

innovative and disruptive future energy technologies that can secure a sustainable energy future.<sup>3–5</sup> At the forefront of clean and sustainable energy technology development lie fuel cell and water splitting technologies, and the key to their success is the development of active and durable electrocatalysts for the constituent oxygen reduction reaction (ORR), oxygen evolution reaction (OER), and hydrogen evolution reaction (HER).<sup>6–9</sup> Thus far, these important electrochemical reactions have been most effectively catalyzed by precious metal-based nanocatalysts whose high cost severely hinders their widespread adoption in commercial applications.<sup>10</sup> Recently, intimate collaboration between theoretical and experimental chemists has provided understanding of the detailed thermodynamic aspects of these electrochemical reactions on the surface of electrocatalysts.<sup>9,11–14</sup> Based on these efforts, multi-directional research into the design of advanced electrocatalysts has begun.<sup>15,16</sup> The most popular approach has been the preparation of noble metal based alloy nanocatalysts, which enable a degree of control over the subtle balance between the binding and desorption of the reaction intermediates *via* d-band engineering.<sup>17–19</sup> Nanoparticle facet control and the structural design concept of core–shell



**Ho Young Kim**

*Ho Young Kim (BS 2015) is currently pursuing his PhD under the supervision of Prof. Sang Hoon Joo at the Department of Energy and Chemical Engineering, UNIST. His research interests include the development of noble metal-based electrocatalysts for energy conversion reactions.*



**Sang Hoon Joo**

*His research group focuses on electrocatalysts for energy conversion reactions. He received the TJ Park Junior Faculty Fellowship (2010), the Knowledge Creation Award (2011), and the KCS Award in Materials Chemistry (2016).*

morphology are further tools to fine-tune the surface energy of nanocatalysts.<sup>20–22</sup> Facet-controlled nanoparticles exhibit different catalytic activities and selectivities from those of spherical nanoparticles due to the differences in facet-dependent surface energy states.<sup>20,21</sup> Additionally, lattice mismatch between the different phases in a core–shell structure creates tensile strain or compressive strain on the surface atoms.<sup>22–24</sup> The nature of this strain is critical to the energy states of the surface atoms and thereby their catalytic properties.

On the other hand, the catalytic events occurring on the surface of nanocatalysts are intrinsically heterogeneous.<sup>25</sup> Therefore, increasing the number of active sites and the overall surface area of a nanocatalyst would be of immense value in boosting the catalytic activity. From this logic, high dispersion of metal atoms on supporting material is crucial for fabricating the efficient heterogeneous electrocatalysts because all catalysis events occurred on the surface of a catalyst particle.<sup>16,26</sup> To date, the impregnation reduction method or functionalization of the carbon surface are regarded as effective methods to prepare the noble metal nanoparticles on carbon carriers,<sup>27,28</sup> however, these preparation methodologies have been limited when we developed rationally designed complex nanostructures by various different strategies. Alternatively, several groups adopted the incipient-wetness procedure in order to prepare the heterogeneous catalysts with high dispersion.<sup>29–31</sup> While the above-described approaches allow for enhanced electrocatalytic activity as well as reduced noble metals content, they are all based on solid nanoparticles, in which a significant fraction of the noble metal atoms are buried under the surface. The past few years have witnessed the development of hollow nanostructures as a novel nanocatalyst design motif.<sup>32–34</sup> In general, the term “frames” refers to nanostructures comprised of only edges without facets; such structures can allow external reactants to access the interior of the nanostructures. The term “cages” is used for nanostructures whose side facets have large cavities. These terms have been hardly differentiated, so we have re-defined the term “hollow” to include both “frames”



**Kwangyeol Lee**

*Professor Kwangyeol Lee (born 1971) obtained his PhD degree (1997) in Chemistry from the University of Illinois at Urbana-Champaign. After fulfilling his military obligation, he joined Korea University in 2003 as a chemistry faculty member, before being appointed as a professor. He is the recipient of the 2009 Wiley-KCS Young Scholar Award. His current interests are on the development of synthetic methodologies for nanoscale materials, the application of nanomaterials in biomedical fields, and the development of nanotechnologies to support the environment by creating sustainable energy sources.*

and “cages” in this review. Hollow nanostructures can provide a multitude of advantages for catalysis over solid nanoparticle catalysts. They can expose very high fraction of surface sites, have strain-induced highly reactive surfaces, and allow for increased collision frequency by confining reactants within nanoscale spaces. Furthermore, hollow nanoparticles would require significantly lower amounts of expensive noble metals, representing a noble-metal economic design. Hollow nanostructures can have metal alloy compositions, enabling very high catalytic activities. However, a major drawback of hollow nanostructures, namely, their lack of structural robustness during catalysis, has also been noted.<sup>35,36</sup> Intense research efforts have been directed towards fortifying flimsy hollow nanostructures, and some promising outcomes in the development of highly active yet robust electrocatalysts have been reported.<sup>35–38</sup>

Herein, we aim to summarize recent advances in nanoframe-based electrocatalysts, including related nanocages, for the ORR, OER, and HER. The synthetic concepts for nanoframes and nanocages will be described along with the synthetic toolkits available, followed by a description of the overall performance of the nanoframe and nanocage catalysts toward specific electrocatalytic reactions as compared to those of nanocatalysts of different structural types. Recent research efforts to enhance the structural robustness and catalytic activity of nanoframe and nanocage catalysts will then be described. Finally, a concluding summary and suggestions for further study directions will be presented.

## 2. Synthetic strategies for hollow nanostructures

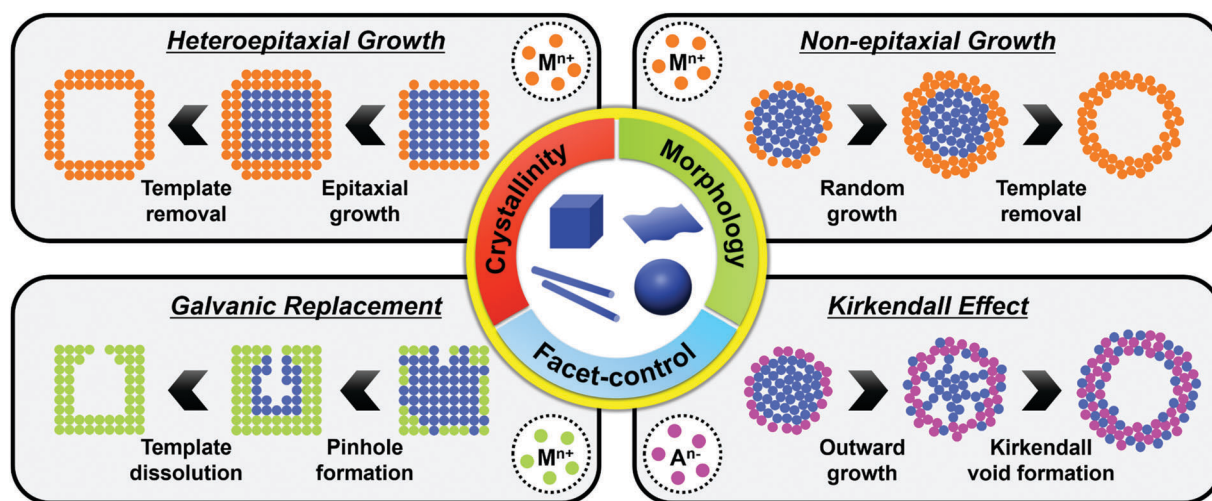
The synthesis of hollow nanostructures largely consists of three steps: the synthesis of a template, the formation of over-layers such as shell or frame structures on the template, and the removal of the template. The template, which can be

either pre-synthesized or prepared *in situ*, plays a crucial role in the synthesis of hollow nanostructures in that it determines the final morphology of the hollow nanostructure and affects its atomic composition. While the synthetic methodologies used for hollow nanostructures vary according to the type of template material, the types of reactions used with a pre-synthesized template are different from those used on an *in situ* formed template. Since the pre-synthesized templates are already thermodynamically stable, heteroepitaxial growth, galvanic replacement, and nanoscale Kirkendall effect processes are feasible with pre-synthesized templates as presented in Scheme 1. However, *in situ* formed templates require delicate kinetic control of the decomposition of several precursors so that the template will be formed significantly ahead of the deposition of over-layers. Without such delicate kinetic control, only simple alloys containing all the components in the reaction vessel would be formed, and none of the many material design concepts, such as phase mixing/segregation and metastability-empowered etching to produce hollow structures, would be possible.

### 2.1. Pre-synthesized template-mediated synthesis: thermodynamic approach

Pre-synthesized templates have a clear advantage over *in situ* formed templates in that (1) their morphologies are very well defined, (2) the types of material used in these template are much more diverse than those of *in situ* formed templates, and (3) the types of reactions used to grow the over-layer can be finely tuned. In this section, reactions involving pre-synthesized templates of various materials are reviewed to provide a glimpse of the rich diversity and potential of employing pre-synthesized templates to produce hollow structures.

**2.1.1. Heteroepitaxial/non-epitaxial growth.** The growth of a hetero-phase on a template and subsequent removal of the template produces hollow structures in a fail-proof fashion.



**Scheme 1** Representative schematic diagram of synthetic methodologies to hollow nanostructures by using various pre-synthesized templates. The physical and chemical properties of resulting hollow nanostructures are heavily dependent on various factors, such as crystallinity, morphology, dimensionality, and exposed facets, of the engaged templates.

The selective removal of the template requires a reaction condition that selectively destabilizes the template while preserving the newly formed phase.

Heteroepitaxial growth on a crystalline template is highly dependent on the crystal structure and lattice parameters of the exposed facets of the template, and minimization of the lattice mismatch between the template and hetero-species is the key to successful hetero-growth on the template.<sup>39–43</sup> Facet-controlled Pd nanoparticles with cubic and octahedral morphologies of cubes and octahedrons have been employed in the synthesis of hollow Ru, Rh, Pt, and Ir nanostructures.<sup>44–56</sup> Snead *et al.* grew Rh on Pd nanocubes and synthesized PdRh nanoboxes or Rh nanoframeworks in reductive or oxidative conditions, respectively (Fig. 1a).<sup>47</sup> Similarly, Zhang *et al.* reported the synthesis of Pt-based nanocages *via* Pt overgrowth on Pd nanocubes and octahedrons and the subsequent removal of Pd *via* etching. The growth of Pt on Pd nanocrystal templates occurred epitaxially so that the synthesized Pt-based nanocages inherited the {100} or {111} facets of the cubic or octahedral Pd nanocrystals, respectively (Fig. 1b).<sup>50</sup> Ye *et al.* used truncated Pd octahedral nanocrystals to grow Ru epitaxially (Fig. 1c).<sup>53</sup> While Ru itself prefers a hcp structure, the epitaxially grown Ru phase exhibited a fcc structure with {100} and {111} facets due to the presence of the fcc Pd template, and the fcc Ru nanoframe remained intact after the removal of the Pd core *via* etching. Concave Pt was used for the heteroepitaxial growth of fcc Ru and Rh phases.<sup>56</sup> The selective growth of Ru and Rh on the {111} vertices of the Pt nanocube template was induced by capping the {100} facets of the Pt nanocubes with CO molecules. The synthesized octahedral Ru and Rh nanoboxes

showed fcc Ru{111} and Rh{111} facets, respectively, whose atom packing motif was inherited from Pt{111}.<sup>56</sup>

Non-epitaxial growth often occurs on polycrystalline or amorphous template materials, and the crystal structures of the resulting over-layers do not conform to the crystal structure of the underlying template materials.<sup>57–65</sup> The growth of the over-layer begins with the random adsorption of hetero-species on the template by surface functionalization/modification or electrostatic interaction.<sup>66–71</sup> Since this growth mechanism proceeds regardless of lattice mismatch, a wide range of materials including carbonaceous materials,<sup>58–62</sup> silica<sup>63–65</sup> and metal compounds<sup>66–71</sup> can be used as a template for these hetero-species. Consequently, the morphology of the resulting hollow nanostructures is more closely related to the morphology of the templates employed than their atomic arrangements and lattice parameters. Many research groups have reported hollow nanostructures with various morphologies and compositions by template-mediated non-epitaxial growth as shown in Fig. 2. Yu *et al.* reported many different forms of hollow micro- and nanostructures with various compositions obtained by this method.<sup>57</sup> Recently, they reported a cooperative assembly-directed method to synthesize TiO<sub>2</sub> nanoshells from various template materials including metals, metal oxides, polymers, carbon, and metal-organic frameworks (Fig. 2a).<sup>72</sup> A mixture of titanium isopropoxide, hexadecylamine surfactants, and ammonia form inorganic-organic composites to coat the template nanoparticles; the coated nanoparticles can then be treated solvothermally to yield either amorphous or crystalline TiO<sub>2</sub> nanoshells. In addition to single-shelled hollow nanostructures, the number of reports on multi-shelled hollow nanostructures

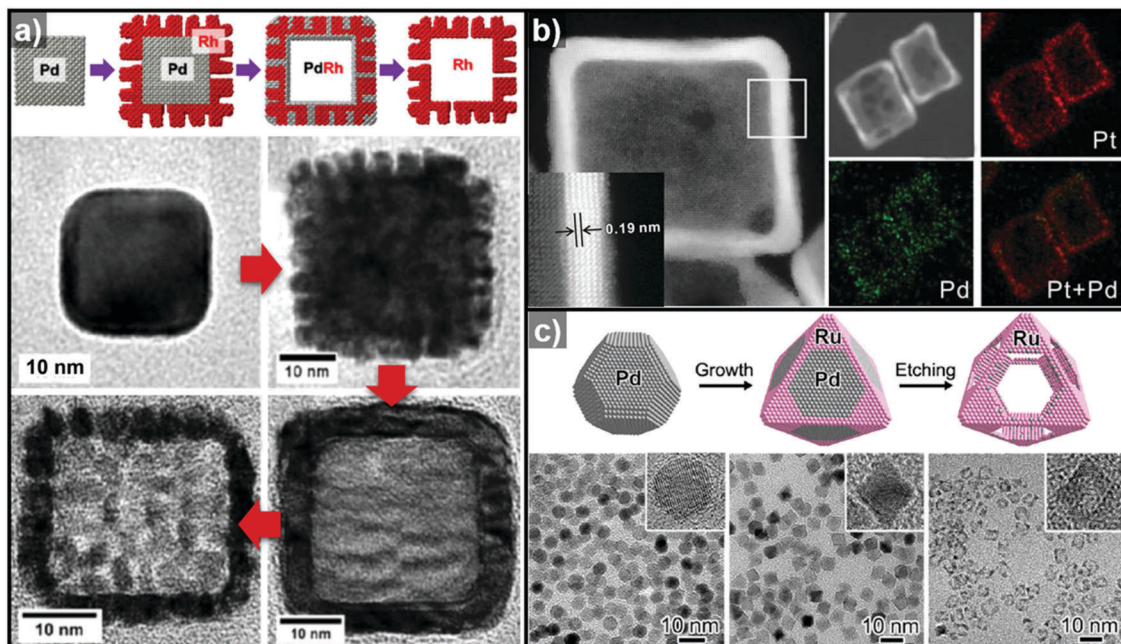


Fig. 1 (a) Schematic diagram of the synthesis of PdRh nanoboxes and Rh nanocages using Pd nanocrystals as templates, and corresponding TEM images for each step. Reproduced with permission from ref. 47. Copyright 2013 American Chemical Society. (b) HAADF-STEM and elemental mapping images of PdPt nanocages. Reproduced with permission from ref. 50. Copyright 2015 AAAS. (c) Schematic diagram of the synthesis of Ru nanocages and TEM images for each step with magnified images in the insets. Reproduced with permission from ref. 53. Copyright 2016 American Chemical Society.

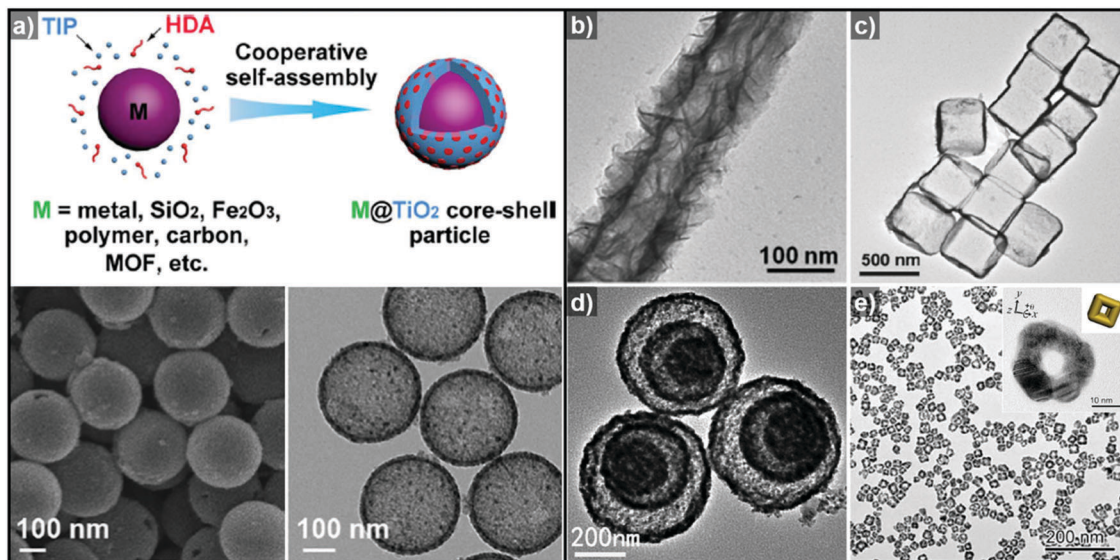


Fig. 2 (a) Schematic diagram of the synthesis of M@TiO<sub>2</sub> core–shell nanoparticles, and SEM (bottom left) and TEM (bottom right) images of hollow TiO<sub>2</sub> nanoparticles. Reproduced with permission from ref. 72. Copyright 2016 AAAS. TEM images of (b) hollow TiO<sub>2</sub> nanotube (reproduced with permission from ref. 70. Copyright 2015 – Published by the Royal Society of Chemistry), (c) SnO<sub>2</sub> nanoboxes (reproduced with permission from ref. 68. Copyright 2011 American Chemical Society), (d) hollow Co<sub>3</sub>O<sub>4</sub> multi-shells (reproduced with permission from ref. 60. Copyright 2013 Wiley-VCH), and (e) Au nanoframes (reproduced with permission from ref. 71. Copyright 2015 American Chemical Society).

is increasing in recent years.<sup>58,60,61</sup> Wang *et al.* demonstrated the precisely controlled synthesis of hollow Co<sub>3</sub>O<sub>4</sub> microspheres ranging from single-shelled to quadruple-shelled based on carbonaceous microsphere (CMS) as templates (Fig. 2d).<sup>60</sup> By controlling the degree of hydration of the cobalt ions, the reaction temperature, and the porosity of the CMS templates, the diffusion rate and depth of the cobalt ions into the CMS templates can be fine-tuned, which ultimately enabled the controlled synthesis of single-, double-, triple- and quadruple-shelled Co<sub>3</sub>O<sub>4</sub> hollow microspheres. Besides metal oxides and other compounds, synthesis of metallic hollow nanostructures is also feasible by non-epitaxial growth. Zhang *et al.* reported the synthesis of Au nanoframes by non-epitaxial growth on AgI nanocrystals by non-epitaxial growth (Fig. 2e).<sup>71</sup> Unlike many examples of template-mediated growth of metal nanostructures, the as-grown Au nanoframes had no correlation in crystal structure with AgI nanocrystal templates, indicating that the growth of Au occurred in non-epitaxial manner. Furthermore, owing to the significant lattice mismatch between Au and the AgI nanocrystals, the growth of Au proceeded in a way that the resulting Au nanoframes were polycrystalline because each Au domains prefer different growing orientation depending on the lattice structure of underlying AgI nanocrystals.

**2.1.2. Kirkendall effect and anion exchange.** Metal nanoparticles can react with oxygen, sulfur, phosphorus, and selenium to form metal compounds. When these elements react with a metallic surface, they become anions, which occupy a large space and thereby move sluggishly within the nanoparticle matrix. Additionally, there is a continuous driving force to convert the metal atoms into cations. In order to satiate this driving force, the relatively smaller metal atoms must diffuse outward as depicted in Scheme 1. Consequently, the metal ions diffuse

outward more rapidly to further react with the anionic species, and the template, which is the core, is consumed to create what is called the Kirkendall void.<sup>73</sup> During the reaction, the experimental conditions can be fine-tuned to adjust the degree of shell formation so that the reaction can be stopped at the core–shell stage or can be made to proceed to the completely hollow nanostructures.

The very first nanoscale Kirkendall effect was demonstrated by Yin *et al.* who reported the formation of hollow nanocrystals of various phases, including Co<sub>3</sub>S<sub>4</sub>, Co<sub>9</sub>S<sub>8</sub>, CoO and CoSe, by reacting Co nanoparticles with corresponding main group elements.<sup>74,75</sup> Cabot *et al.* also reported the synthesis of hollow iron oxide nanoparticles by oxidizing iron nanoparticles.<sup>76</sup> In the same year, Peng *et al.* showed a similar result by annealing Fe nanoparticles under oxidative condition to synthesize core–shell–void Fe–Fe<sub>3</sub>O<sub>4</sub> and hollow Fe<sub>3</sub>O<sub>4</sub> nanoparticles (Fig. 3a).<sup>77</sup> Chiang *et al.* reported the Kirkendall effect-induced synthesis of hollow Ni<sub>2</sub>P and Co<sub>2</sub>P nanoparticles by reacting corresponding metal nanoparticles with trioctylphosphine.<sup>78</sup>

Alternatively, anion exchange can also be used to form hollow nanoparticles. When metal oxides are used as templates, the exchange with larger anions is often accompanied by the Kirkendall effect. Park *et al.* reacted ZnO nanoparticles with hexamethyl-disilathiane to form ZnO@ZnS yolk–shell and completely hollow ZnS nanoparticles.<sup>79</sup> As the anion exchange reaction between oxygen and sulfur proceeded, the outward migration of Zn<sup>2+</sup> ions continued until the ZnO core was completely consumed due to the faster diffusion rate of the Zn<sup>2+</sup> ions, which are smaller than S<sup>2-</sup>. Kuo *et al.* reacted cubic and octahedral Cu<sub>2</sub>O nanoparticle templates with Na<sub>2</sub>S to form a Cu<sub>2</sub>S shell and then removed the Cu<sub>2</sub>O phase *via* acid-etching to form Cu<sub>2</sub>S boxes (Fig. 3b).<sup>80</sup> Kim *et al.* recently reported the

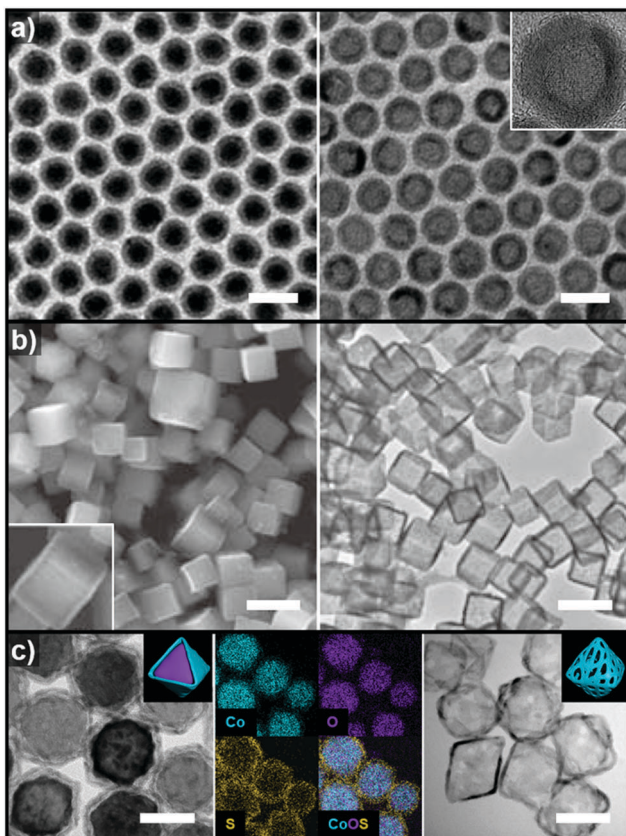


Fig. 3 (a) TEM images of Fe@Fe<sub>3</sub>O<sub>4</sub> core–shell and hollow Fe<sub>3</sub>O<sub>4</sub> nanoparticles. Reproduced with permission from ref. 77. Copyright 2007 Wiley–VCH. (b) SEM and TEM images of Cu<sub>2</sub>S nanocages. Reproduced with permission from ref. 80. Copyright 2011 Wiley–VCH. (c) TEM and elemental mapping images of CoO@Co<sub>x</sub>S<sub>y</sub> core–shell nanoparticles and TEM image of Co<sub>3</sub>S<sub>4</sub> nanocages. Reproduced with permission from ref. 81. Copyright 2017 Royal Society of Chemistry. All scale bars are 50 nm.

synthesis of mixed cobalt–nickel sulfide (Co<sub>x</sub>Ni<sub>y</sub>S<sub>z</sub>) nanocages using octahedral CoO nanoparticles as templates (Fig. 3c).<sup>81</sup> As the surface of the CoO templates reacted with activated sulfur atoms in 1-octadecene, the smaller size of the Co<sup>2+</sup> compared to S<sup>2-</sup> facilitated the outward diffusion of Co<sup>2+</sup> to form a Kirkendall void at the interface between the CoO core and the Co<sub>x</sub>S<sub>y</sub> shell. The Co<sub>x</sub>S<sub>y</sub> nanocages, obtained by acid etching of the CoO core, could further undergo a cation exchange reaction with Ni<sup>2+</sup> to form mixed cobalt–nickel sulfide (Co<sub>x</sub>Ni<sub>y</sub>S<sub>z</sub>) nanocages.

**2.1.3. Galvanic replacement reaction.** Galvanic replacement, an electrochemical process in which the oxidation of one metal is effected by another metal ion with higher reduction potential, is another powerful and essential synthetic tool applicable to various types of metal and metal compound templates. The selection of appropriate redox pairs is crucial for a successful galvanic replacement reaction.

Additionally, it is quite common for the oxidized template to be removed during a galvanic replacement reaction to form hollow reaction products at the end of the reaction.

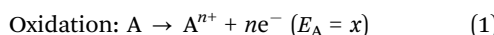


Table 1 Reduction potential of commonly used transition metals (ref. 82)

Reduction reaction	$E^\circ$ (V vs. SHE)
Mn <sup>2+</sup> + 2e <sup>-</sup> → Mn	-1.19
Zn <sup>2+</sup> + 2e <sup>-</sup> → Zn	-0.76
Fe <sup>2+</sup> + 2e <sup>-</sup> → Fe	-0.45
Co <sup>2+</sup> + 2e <sup>-</sup> → Co	-0.28
Ni <sup>2+</sup> + 2e <sup>-</sup> → Ni	-0.26
Cu <sup>2+</sup> + 2e <sup>-</sup> → Cu	+0.34
Rh <sup>3+</sup> + 3e <sup>-</sup> → Rh	+0.76
Pd <sup>2+</sup> + 2e <sup>-</sup> → Pd	+0.95
Ag <sup>+</sup> + e <sup>-</sup> → Ag	+0.80
Ir <sup>3+</sup> + 3e <sup>-</sup> → Ir	+1.16
Pt <sup>2+</sup> + 2e <sup>-</sup> → Pt	+1.18
Au <sup>3+</sup> + 3e <sup>-</sup> → Au	+1.50

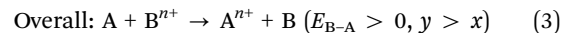
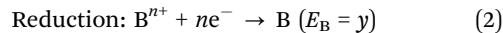


Table 1 shows the reduction potentials of various non-noble and noble metals that are commonly used in galvanic replacement reactions.<sup>82</sup> The most extensively studied redox pair is the Au–Ag system.<sup>83–89</sup> The first example of the use of a nanoscale galvanic replacement to synthesize hollow nanostructures was demonstrated by Y. Xia *et al.*<sup>83</sup> Using Ag nanoparticles and nanowires as sacrificial templates, they reported a general synthetic route to various hollow nanostructures by introducing Au<sup>3+</sup>, Pt<sup>2+</sup>, and Pd<sup>2+</sup> salt precursors. Two or three Ag atoms are involved in the reduction of one Pd, Pt, or Au cation, which is conducive to the formation of hollow nanostructures and the complete dissolution of the Ag templates into soluble species. In subsequent works, they used slightly truncated Ag nanocubes as sacrificial templates to form Au nanoboxes.<sup>84</sup> It is noteworthy that the galvanic replacement occurred preferentially on the facets with high surface free energy. Because the surface free energy of metals with an fcc crystal structure generally decreases in the order of  $\gamma_{\{110\}} > \gamma_{\{100\}} > \gamma_{\{111\}}$ ,<sup>90</sup> the facets, on which the galvanic replacement reaction would occur, for particular metal nanocrystals can be predicted. However, it is also feasible to make the reaction occur only on the desired facets by capping the undesired facets.<sup>91</sup>

In addition to facet selectivity, various phenomena such as alloying/dealloying and the Kirkendall effect can be coupled with galvanic replacement to add further diversity to the elemental composition and architecture of the hollow nanostructures.<sup>92</sup> González *et al.* reported simultaneous or sequential galvanic replacement and Kirkendall effect using Ag nanocubes to synthesize complex hollow nanostructures of Au–Ag, Ag–Pd, and Au–Ag–Pd (Fig. 4a).<sup>93</sup> The initial Au deposition on the Ag nanocube *via* galvanic replacement reaction results in the formation of pinholes, which enable the dissolution of the inner portion of Ag nanocube. As the reaction continues, Au deposition on the interior surface of the cavity occurs, so that a thin Ag layer is enclosed between two Au shells. At this stage, both Galvanic replacement and Kirkendall effect are in action simultaneously due to the faster diffusion rate of Ag<sup>+</sup> ions, leading to the formation of a Kirkendall void between the two Au shells. They also demonstrated a sequential galvanic replacement and

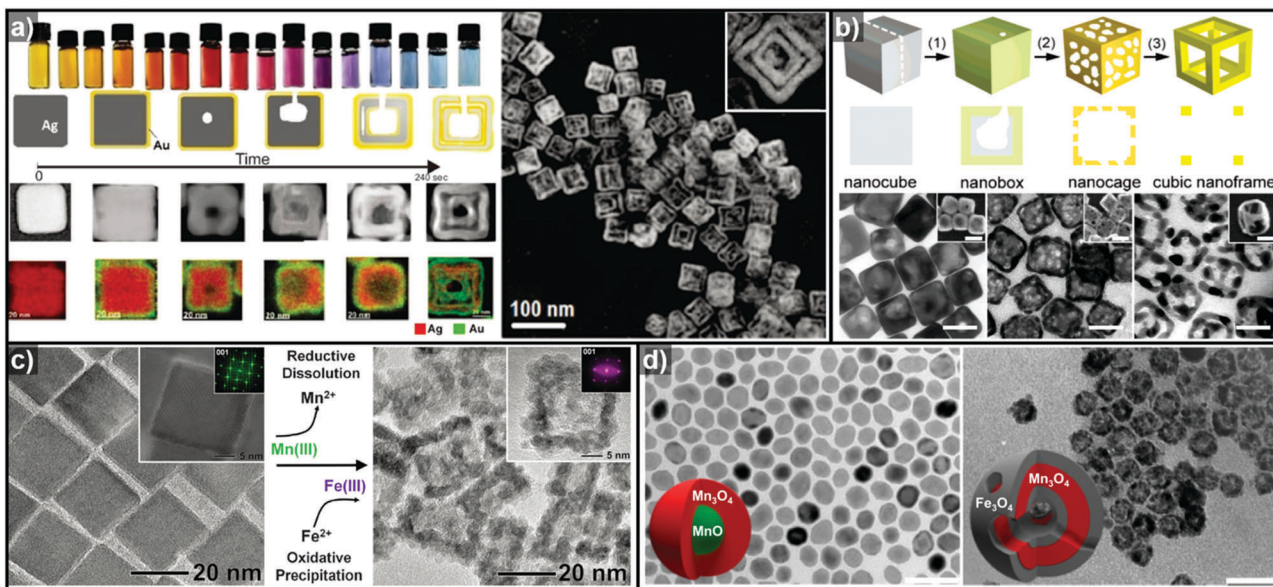


Fig. 4 (a) Images of optical and morphological evolution of AuAg double-walled nanoboxes and HAADF-STEM image of AuAg double-walled nanoboxes. Reproduced with permission from ref. 93. Copyright 2011 AAAS. (b) Schematic diagrams of Au-Ag nanocages and Au nanoframes from Ag nanocubes and the corresponding TEM images. Reproduced with permission from ref. 88. Copyright 2007 American Chemical Society. (c) TEM images showing  $\text{Fe}_2\text{O}_3$  nanocages (right) synthesized from  $\text{Mn}_3\text{O}_4$  nanocrystals (left). Reproduced with permission from ref. 98. Copyright 2013 AAAS. (d) TEM images of hollow  $\text{Mn}_3\text{O}_4/\text{Fe}_3\text{O}_4$  hetero-nanostructures synthesized from  $\text{MnO}@\text{Mn}_3\text{O}_4$  core-shell nanoparticles. Reproduced with permission from ref. 100. Copyright 2016 American Chemical Society.

Kirkendall effect in which an Ag nanocube first undergoes a galvanic replacement reaction with Pd, and then the addition of Au promotes the formation of cavities, primarily driven by the Kirkendall effect. Lu and Sun *et al.* demonstrated the fabrication of Au/Ag nanocages and Au nanoframes by combining a galvanic replacement reaction and the selective removal, or dealloying, of Ag (Fig. 4b).<sup>88,89</sup> In the initial stage, when Au deposition occurs on the Ag templates, the Au-Ag alloying process is favoured owing to the stronger bonding between Au and Ag as compared to Ag-Ag and Au-Au, and the low energy barrier for interdiffusion between Ag and Au. The overall reaction process can be kinetically controlled to stop at Au-Ag nanocages or to form Au nanoframes *via* further etching process. In the case of Pt, due to the Pt-Pt bonding being stronger than Pt-Ag bonding, the growth of Pt islands on the Ag template is more favoured than alloying.<sup>92</sup>

In addition to Au and Ag, various other transition metals can be coupled for the galvanic replacement reaction. Hong *et al.* synthesized Pd-Pt nanocages and hollow dendritic nanostructures based on octahedral and cubic Pd nanocrystals by controlling the concentration of the reducing agent.<sup>94</sup> While the formation of hollow nanostructure was attributed to galvanic replacement reaction between the Pd nanocrystals and Pt precursors, the reduction of the Pt precursor also occurs to form Pt branches on the Pd nanocrystals in the presence of increased concentrations of the reductant. Interestingly, the dissolved Pd ions are also reduced due to the high concentration of reductant, resulting in the eventual formation of hollow Pd-Pt dendritic nanostructures.

Liu *et al.* used cubic Pd nanocrystals as sacrificial templates to synthesize hollow Pd-Ir alloy nanostructures.<sup>95</sup> In the initial

stage of the reaction, the galvanic replacement reaction dominates to deposit Ir by preferentially oxidizing Pd atoms on the vertices of the Pd nanocubes to form Pd@Ir core-shell octapod nanostructures. As the reaction continues, the co-reduction of Ir ions and the dissolved Pd ions occurs simultaneously with galvanic replacement, leading to the formation of Pd-Ir alloy nanocages. Cu is another excellent template material with a relatively low reduction potential and high alloying capability.<sup>96,97</sup> Recently, Han *et al.* reported a wet chemistry synthetic route to Cu-based binary hollow nanostructures by controlling the balance between galvanic replacement and the reduction kinetics of the precursors.<sup>97</sup> They incorporated a variety of metal species (M = Ru, Rh, Pd, Os, Ir and Pt) into the Cu nanocrystal template to synthesize hollow bimetallic CuM nanostructures with well-defined morphologies. At lower temperature, the galvanic replacement reaction predominates and the original morphology of the Cu template is preserved. However, at higher reaction temperatures, the reduction of the dissolved Cu ions also occurs to facilitate the alloying of Cu and M, which in turn leads to hollow nanostructures with a significantly different morphology from that of the original template.

Thus far, the most used templates for galvanic replacement have been metals with low reduction potentials that can be easily oxidized by other metal ions. However, there are several cases where metal oxides have been used as templates where the metal ion species of the templates possess multiple oxidation states. Oh *et al.* demonstrated the first galvanic replacement reaction in metal oxide nanocrystals (Fig. 4c), using  $\text{Mn}_3\text{O}_4$  nanocrystals as templates for galvanic replacement with  $\text{Fe}^{2+}$  ions.<sup>98</sup> As the reductive dissolution of  $\text{Mn}^{3+}$  to  $\text{Mn}^{2+}$

occurs, the oxidative precipitation of  $\text{Fe}^{3+}$  from  $\text{Fe}^{2+}$  proceeds to yield hollow  $\gamma\text{-Fe}_2\text{O}_3$  nanocages (Fig. 4d). Susman *et al.* reported the pH-dependent galvanic replacement of  $\text{Cu}_2\text{O}$  nanocrystals with Au or Pd cations to synthesize hollow Au or Pd nanocages.<sup>99</sup> At lower pH, the separate and independent nucleation processes of Au or Pd are more favoured due to the higher degree of protonation of the  $\text{Cu}_2\text{O}$  surface, which changes the surface charge. However, at relatively higher pH, growth process is more favoured than nucleation. This facilitates the deposition of a uniform coating of Au or Pd on the  $\text{Cu}_2\text{O}$  templates to form  $\text{Cu}_2\text{O}@\text{M}$  ( $\text{M} = \text{Au}$  or  $\text{Pd}$ ) core–shell nanocrystals, which yield hollow metal nanocages after etching of the  $\text{Cu}_2\text{O}$  core. Recently, López-Ortega *et al.* also reported the synthesis of hollow  $\text{Mn}_3\text{O}_4/\text{Fe}_3\text{O}_4$  hetero-nanostructures from  $\text{MnO}@\text{Mn}_3\text{O}_4$  core–shell seeds using either a trace amount of  $\text{H}_2\text{O}$  or an organic oxidizing agent.<sup>100</sup> In the presence of an oxidizing agent, the  $\text{MnO}$  core is oxidized to  $\text{Mn}_3\text{O}_4$ , and simultaneously,  $\text{Mn}^{3+}$  is reduced to  $\text{Mn}^{2+}$  as  $\text{Fe}^{2+}$  is deposited to form  $\text{Fe}_3\text{O}_4$  as shown in Fig. 4d.

## 2.2. *In situ* formed template-mediated synthesis: kinetic approach

Recently, the synthesis of hollow structures from *in situ* formed templates has undergone great advances. While the obvious advantage of using *in situ* formed templates would be the ease of synthesis, the intricate play between alloying and dealloying also makes this synthetic approach very enticing. In order to ensure the selective *in situ* formation of the template, fine control of the decomposition kinetics of the multiple metal precursors is required.

Yoon *et al.* reported the sequential decomposition of Cu and Ir precursors, to form  $\text{CuIr}$  octahedral nanocrystals with a Cu-rich core and Ir-rich shell.<sup>101</sup> It is tempting to explain the core–shell structure by the fact that the thermal decomposition of the Cu precursor occurs faster than that of the Ir precursor. However, the immiscibility between Ir and Cu also aided the formation of the core–shell structure in this case. In general, the final compositional distribution and morphology of the nanoparticles cannot be solely attributed to kinetic considerations, since kinetically-formed nanoparticles can undergo changes in compositional distribution and morphology due to thermodynamic factors such as mixing enthalpy, phase segregation, surface energy, and reduction potentials.<sup>36–38,102–104</sup> One of the most important thermodynamic factors in the synthesis of multicomponent alloy nanoparticles is the enthalpy of mixing, which represents the miscibility of the multiple components.<sup>105,106</sup> The enthalpy of mixing values are available for various solid solution phases, and can be used to explain the tendencies of miscibility and composition changes in bulk materials. However, the experimental results for many nanoscale materials do not agree with the miscibility predicted from the enthalpy of mixing.<sup>104,105,107–109</sup> For example, Huang *et al.* reported the solid–solution alloying of Ru and Cu in nanoscale, which are completely immiscible in bulk (Fig. 5a).<sup>107</sup> While an hcp structure is favored for Ru, which is immiscible with Cu, fcc structured Ru can be stabilized at the nanoscale and can

mix with Cu, unlike the bulk materials. Due to the distinctly different mixing behavior at the nanoscale and in the bulk state, great efforts have been made to understand the compositional stability of multicomponent nanoparticles.<sup>110–112</sup>

Many researchers also have made a large effort to predict the phase segregation behavior in nanoscale, which largely depends on nanoparticle size, shape and composition.<sup>113–116</sup> Xiong *et al.* reported the calculation of alloying ability bimetallic system such as Cu–Ag, Au–Ni, Ag–Pt and Au–Pt, all of which are immiscible in bulk.<sup>113</sup> Based on their calculation result, Cu–Ag system, for example, showed remarkable drop down of formation enthalpy with decreasing size. For  $\text{Cu}_{0.5}\text{Ag}_{0.5}$  nanoparticles, the formation enthalpy turns positive (immiscible) to negative (miscible) when the particle size reduces below 3.1 nm.<sup>117–119</sup> On the contrary, initially-formed nanoscale alloy undergo phase segregation behavior by various parameters such as temperature, atmosphere, nanoparticle size *etc.*<sup>117,120–123</sup> For instance, Guisbiers *et al.* reported theoretical calculation and corresponding experimental results of alloy formation and phase segregation behaviors of bimetallic Cu–Ni nanoparticles, which is completely miscible system in bulk phase.<sup>117</sup> Under elevated temperature with appropriate heat treatment, Cu and Ni easily forms solid solution alloy nanoparticles. However, by decreasing the temperature, the miscibility gap between Cu and Ni was generated, and subsequent phase segregation of Ni toward nanoparticle surface occurred. Their calculation results also showed that the miscibility temperature of Cu–Ni pair is increased with larger particle size and increased number of facets. By their calculation results phase segregation behavior of Cu–Ni solid solution nanoparticle can be predicted, which is transformed to core–shell or Janus structure by nanoparticle size or shape.

The presence of multiple metal precursors could easily lead to the formation of alloy nanoparticles, thwarting attempts to form multi-component structures with a well-defined radial distribution. Therefore, the phase segregation phenomena of alloy nanoparticles are often exploited in the synthesis of hollow nanostructures based on *in situ* formed template nanoparticles.<sup>37,124,125</sup> Phase segregation at the surface of a multimetallic nanoparticle is caused by the difference in the surface energies of the metal components.<sup>120</sup> Numerous parameters contribute to the driving force which affects the degree of segregation or the alloying process. The metal–metal binding energies, for example, the energies of the A–A, B–B, and A–B bonds in an AB bimetallic nanoparticle system, are linked to the phase segregation phenomenon.<sup>120–123</sup> When the A–B bonds are stronger than any other bonds, the nanoparticles gradually form the AB alloy phase. Second, the discrepancy between the surface energies of different metals can also affect the phase segregation.<sup>120,122,123,126,127</sup> The element with lower surface energy migrates to the surface to gain thermodynamic stability.<sup>120</sup> Third, the strain caused by the lattice mismatch driven by the difference in the atomic radii of the elements can induce phase segregation.<sup>23,128,129</sup> The mismatch causes an increase in the strain energy, resulting in phase segregation in the nanoparticles. The presence of adsorbents or surface

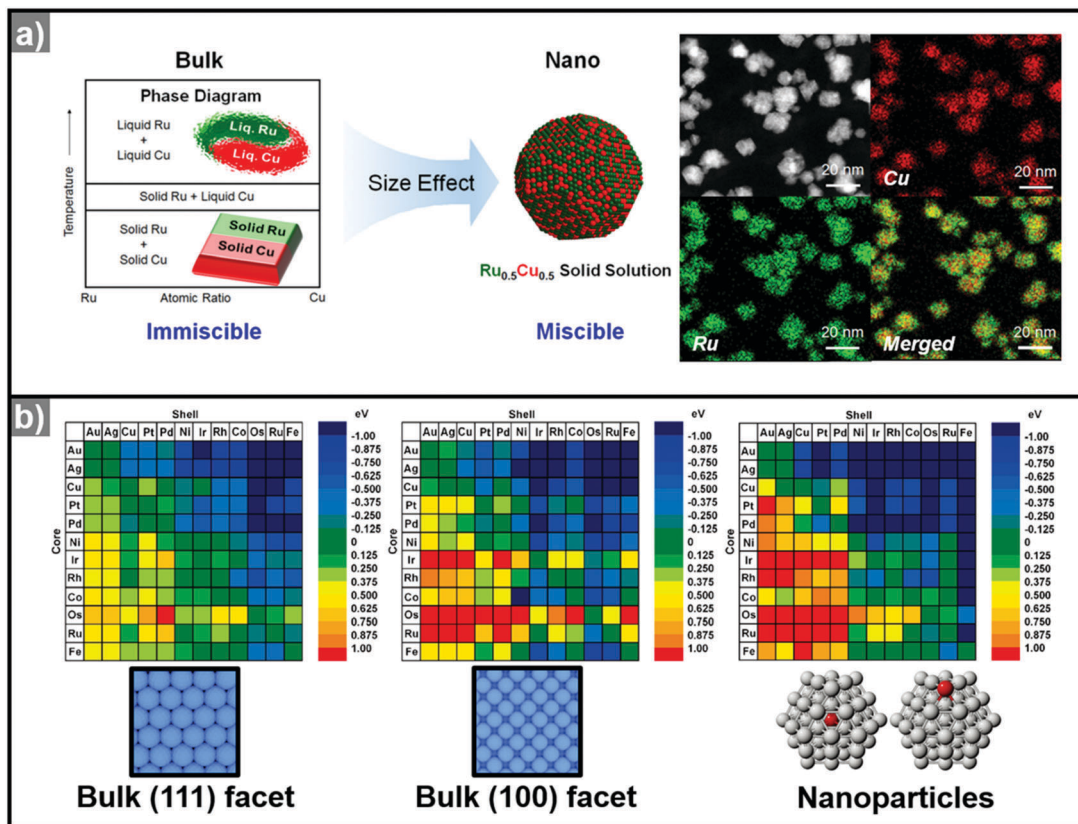


Fig. 5 (a) (left) Schematic representation of Ru–Cu solid solution alloy NPs within the nano-size dimension. Ru and Cu are immiscible in bulk state. (right) HAADF-STEM image and its corresponding EDX elemental mapping analysis of RuCu solid solution alloy NPs. Reproduced with permission from ref. 107. Copyright 2017 American Chemical Society. (b) Color-coded matrix of segregation energies for impurities in 55-atom NPs composed of 12 late-transition metals. Color towards the blue end indicates a stable core/shell structure, as depicted in the matrix. Conversely, color towards the red end indicates that the core/shell structure is reversed. The matrix located at left and center related to the (111) and (100) surfaces, the matrix at the right is related to the cluster. Reproduced with permission from ref. 112 Copyright 2009, American Chemical Society.

binding moieties can also induce phase segregation behavior.<sup>120,128–132</sup> Core elements can be drawn to the surface when adsorbents and surface binding moieties favor binding with them. Tao *et al.* reported a notable example of phase segregation induced by surrounding gas conditions in a PdRh nanoparticle.<sup>133</sup> Because Pd atoms prefer to bind to gaseous CO, the Pd@Rh core shell structure can be transformed into Rh@Pd. On the other hand, without CO (in the presence of only NO), the Rh@Pd nanoparticles revert to the Pd@Rh composition because of the surface energy of Rh is lower than that of Pd.

The use of computational methods to understand the phase segregation behavior of multi-component nanoparticles has also been explored recently.<sup>112,134</sup> Wang *et al.* predicted the trends of core-shell preferences for binary alloy nanoparticles.<sup>112</sup> Based on a DFT method, they calculated the segregation energies of each metal combination. Fig. 5b shows that the surface segregation tendencies depend on the exposed atomic arrangements or regio-specific active sites. Therefore, the phase segregation phenomena in the three-dimensional nanostructures would be different from those in conventional zero-dimension nanoparticles. In short, the migration and the change in surface composition could be controlled through understanding of the phase segregation phenomena.

Moreover, facet control of alloy nanoparticles can add further diversity to phase mixing and segregation. Facet-controlled nanoparticles exhibit distinctive surface structural features, namely, vertices, edges, and facets, which have different surface energies.<sup>20,135,136</sup> While the thermodynamics of atom migration within an alloy nanoparticle is governed by the expression  $\Delta G = \Delta H - T\Delta S$ , the  $\Delta S$  terms are notably different among these surface structural features and therefore the surface alloying can be different from one surface structure to another.<sup>120,121,126,137</sup> For example, large atoms within an alloy nanoparticle would migrate to the vertices and edges where the free space can best accommodate larger atoms.<sup>120,126,128,129</sup> When the vertices and edges have a very robust composition and the facet center consists of a phase that is unstable in a caustic medium, nanoframe can be obtained by etching. Furthermore, when phase segregation occurs in an alloy nanoparticle, new interfaces are generated between the segregated phases.<sup>120,121</sup> These grain boundaries are intrinsically unstable due to lattice mismatch and structural defects, and can serve as effective passages for atom movement, thus greatly facilitating intra-nanoparticle diffusion processes.<sup>37,102,125</sup> While phase segregation confined to the surface gives rise to single-layered nanoframes, the presence of intra-nanoparticle diffusion passages can produce structurally-fortified nanoframes.<sup>37,38</sup>

Thus, hollow nanostructures such as nanocages and nano-frames with well-defined morphologies can be fabricated only when the initial formation of template nanoparticles occurs quickly and the final multicomponent nanoparticle has a compositional arrangement that allows easy etching of the template phase. Cu and Ni are excellent template materials for the one-pot, wet-chemical synthesis of hollow nanostructures, since the decomposition temperatures of these metal precursors are quite low, allowing the fast formation of the template nanoparticles, and they can easily be removed by etching. For example, Yoon *et al.* reported the one-step synthesis of octahedral Cu-doped Ru nanocages *via* both kinetic and thermodynamic approaches.<sup>103</sup> The co-decomposition of the Cu and Ru precursors resulted in the formation of Cu-rich template nanoparticles during the initial stage and the subsequent growth of Ru on the Cu-rich nanoparticles. However, the unstable nature of the Cu phase in the presence of bromide ions resulted in the *in situ* dissolution of the Cu-rich phase at the core to give a hollow nanocage structure. In short, the fast decomposition kinetics of the Cu precursor and the metastable nature of the Cu nanoparticles enabled a one-pot approach to hollow Ru nanostructures. Other hollow nanostructures based on noble-metals such as Pt, Pd, Ir, and Rh could also be prepared by exploiting the metastable nature of Cu as a template.<sup>104,138–141</sup> A similar strategy using metastable Ni is also applicable to the formation of hollow noble metal nanostructures.<sup>37,142–146</sup> For example, Hwang *et al.* reported the thermal co-decomposition of Ni and Ru precursors to give Ni@Ru core-shell nano-sandwiches, which can be subsequently treated with acid to yield hollow nanobox structures.<sup>145</sup> The faster decomposition kinetics of the Ni precursor enabled the formation of a Ni core and a Ru shell. Also, many researchers exploited *in situ* generated Ni nanoparticles prepared from Bönnemann synthesis or polyol methods for sacrificial templates for Pt-based alloy hollow nanostructures.<sup>147–154</sup> For instance, Bae *et al.* reported one-pot synthesis of carbon-supported PtNi hollow nanoparticles *via* fast reduction of NiCl<sub>2</sub> precursor by NaBH<sub>4</sub>, followed by galvanic replacement of Pt.<sup>147</sup> Moreover, Chattot *et al.* also reported atomic-scale snapshots of the formation, growth and hollowing out mechanisms *via* scanning transmission electron microscopy (STEM), energy-dispersive X-ray spectroscopy (EDX), operando wide-angle and small-angle X-ray scattering (WAXS and SAXS) techniques.<sup>154,155</sup> Their study revealed that Ni-rich nanoparticles embedded in a Ni<sub>x</sub>B<sub>y</sub>O<sub>z</sub> shell were formed first, and the combined reaction of galvanic replacement and nano-scale Kirkendall effect resulted the formation of Ni-rich core@Pt-rich shell nanoparticles, and finally formed PtNi hollow nanoparticles. More than Cu and Ni, other first-row transition metal such as Co, Fe, and Zn also can conduct similar role as an *in situ* formed sacrificial templates.<sup>150,156–158</sup>

As stated previously, the presence of adsorbents or surface binding moieties can also induce phase segregation behavior in multicomponent nanoparticles, which in turn enables the fabrication of hollow nanostructures. For example, Oh *et al.* demonstrated the phase segregation behavior of octahedral Pt@Ni core@shell nanoparticles under a CO atmosphere.<sup>37</sup>

The CO atmosphere induces the outward migration of Pt from the core towards the  $\langle 100 \rangle$  (vertex) direction rather than the  $\langle 111 \rangle$  (facet) and  $\langle 110 \rangle$  (edge) directions. The site-specific energy level difference was induced by the adsorption of CO molecules on the surface, resulting in geometrically precise phase segregation in the octahedral PtNi nanoparticles. The resulting dealloyed nanoparticle has Pt-rich edges and core with a Cartesian coordinate-like morphology. The removal of the Ni component *via* acid treatment resulted in an octahedral nanoframe structure with Cartesian coordinates.

In summary, the initially formed multicomponent nanoparticles can undergo further compositional and morphological changes due to a number of thermodynamic parameters, and the selective destabilization of certain components and the removal of metastable phases can lead to the formation of hollow nanostructures (Fig. 6).

### 3. Electrocatalytic application of hollow nanostructures

Clean energy sources and sustainable energy production methods are urgently needed to prevent severe environmental problems. Hydrogen has received a great deal of attention as a promising energy source in fuel cells due to its high energy density. Hydrogen fuel cells are operated by two complementary redox reactions: the hydrogen oxidation reaction (HOR) at the anode and the ORR at the cathode, and produce electricity and pure water without any pollutants.<sup>17,159,160</sup> On the other hand, water electrolyzers, in which the electrode reactions comprise the OER at the anode and HER at the cathode, represent an attractive method to produce pure hydrogen in a carbon-neutral manner when coupled with renewable energy sources.<sup>4,161,162</sup> While there is great potential for these technologies to provide at least a partial solution to rapidly worsening environmental problems, the cost of electricity for the production of hydrogen and the efficiency of the fuel cells are formidable obstacles that must be overcome in order for these technologies to penetrate the mainstream energy market.<sup>15,161,163–165</sup> Both technologies require the development of highly active and durable catalysts that far surpass the performance of state-of-the-art catalysts; accordingly, great research efforts are being focused upon the development of catalysts with new design concepts and excellent performances.<sup>162,166</sup>

Catalytic activity can be enhanced by (1) increasing the number of catalytic events on a given catalyst and (2) enhancing the intrinsic catalytic activity of the catalyst. Increasing the surface area has been an effective strategy to increase the number of catalytic events, and can be accomplished by decreasing the particle size of the heterogeneous catalysts and by forming highly open catalyst morphologies such as hollow nanocages and nano-frames. On the other hand, the intrinsic activity can be improved by controlling the surface energy, which depends on the chemical composition, structural disorders, defects and coordination nature of the surface and exposed facets. Furthermore, several recent researches underlined the calculation results of the relationship between catalytic activity and surface coordination number.<sup>11,167</sup>

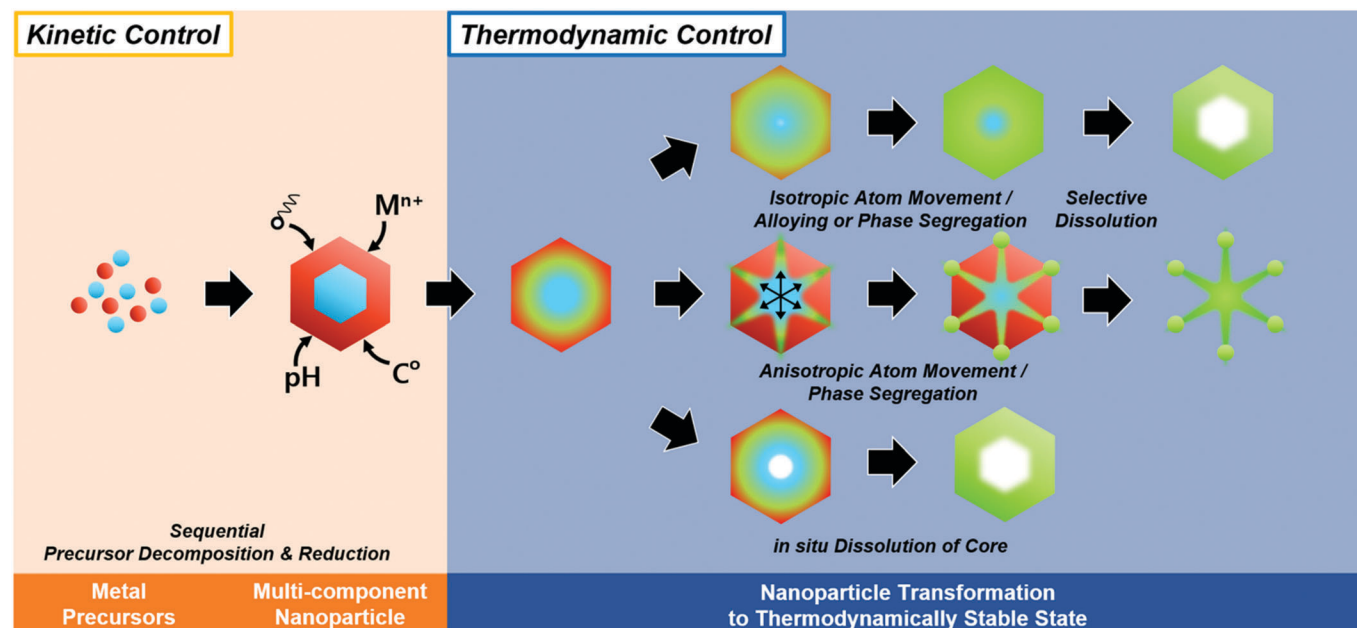


Fig. 6 Schematic illustration of *in situ* formed template-mediated synthetic approach toward hollow nanostructures with kinetic and thermodynamic control.

By calculation results from Calle-Vallejo *et al.*, concave surface geometry with higher coordination number than convex surface is predicted to show better oxygen reduction reaction.<sup>167</sup> Unlike solid nanoparticle surface, hollow nanostructures are prone to have concave surface in their interior, which can show higher electrocatalytic activity than solid nanoparticles, which have only convex surface. Asset *et al.* reported experimental identification method of concave and convex catalytic surface *via* electrochemical CO-stripping method.<sup>155,168,169</sup> Also, they experimentally demonstrated specific activity of concave catalytic surface is more active than convex catalytic surface.<sup>155</sup> Moreover, hollow nanoparticles easily tend to have structural disorders or defects in their structure, which are usually generated during the dissolution of the core component.<sup>170–172</sup> Combining these together, hollow nanoparticles have high intrinsically active catalytic surface as well as increased catalytic surface area. Therefore, there has been intense research interest in the fabrication of hollow nanostructured catalysts with controlled surface compositions and crystal facets.<sup>47,50,81</sup>

### 3.1. Fuel cell electrode reactions

**3.1.1. Oxygen reduction reaction.** Proton exchange membrane fuel cell (PEMFC) technology has a multitude of advantages over other fuel cell technologies including high power density, low operating temperature, short start-up time, and system design.<sup>159,160</sup> At the anode of the PEMFC, hydrogen is oxidized to produce protons and electrons ( $\text{H}_2 \rightarrow 2\text{H}^+ + 2\text{e}^-$ , HOR). At the cathode, oxygen is reduced by protons and electrons transferred from the anode to produce water ( $1/2\text{O}_2 + 2\text{H}^+ + 2\text{e}^- \rightarrow \text{H}_2\text{O}$ , ORR). The reaction rate of the ORR is six or more orders of magnitude slower than that of the HOR, and therefore the ORR determines the overall rate of fuel cell reactions.<sup>160</sup>

Since PEMFCs are operated in strongly acidic media, the catalysts on the electrodes are inevitably subjected to a highly corrosive acidic environment. Therefore, platinum-based electrocatalysts, which are highly active as well as considerably stable under acidic conditions, have been widely studied for the ORR in past decades.<sup>159,173,174</sup>

**3.1.1.1. Brief summary of recent advances in Pt-based ORR electrocatalyst.** Pt-based ORR electrocatalysts have a long history, and therefore numerous excellent reviews are available in this field (Fig. 7).<sup>6,17,159,160,173–175</sup> In this section, a brief overview of the developments in Pt-based electrocatalysts during the last decade is given. Investigation of the ORR activity of single crystalline Pt electrodes, such as Pt(111), Pt(100), Pt(110), *etc.*, clearly revealed a strong relationship between the catalytic activity and the surface energy.<sup>176,177</sup> Motivated by this model catalyst study, the synthesis of facet-controlled Pt nanoparticles

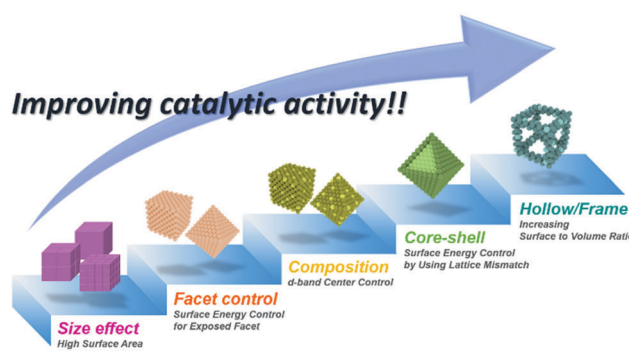


Fig. 7 Schematic illustration of brief history of the development of Pt-based ORR electrocatalysts (modified from ref. 5. Copyright 2016 AAAS).

with particular shapes was attempted in order to exploit the structural effects of nanoparticle catalysts. For instance, octahedral Pt nanoparticles enclosed by {111} facets were found to be more active for the ORR than cubic Pt nanoparticles with {100} facets using a perchloric acid electrolyte, which is consistent with the results from bulk single crystalline Pt electrodes.<sup>177,178</sup> Moreover, enhanced activity was observed in Pt nanoparticles enclosed by high-index facets, which have a high density of low coordinated sites on surface features such as steps, kinks, and ledges, leading to a high surface energy.<sup>179–190</sup> For example, Yu *et al.* reported Pt concave nanocubes, enclosed with high-index facets such as {510}, {720} and {830} showed 3.1 to 4.1-fold improved ORR specific activity compared to Pt nanocubes enclosed with {100} facets.<sup>190</sup>

Another mainstream approach to fabricate superior ORR catalysts has been the development of Pt-based alloy nanoparticles, because the incorporation of a transition metal into a Pt-based catalyst can result in high ORR activity.<sup>191–194</sup> Alloying Pt with other transition metals such as Ni, Co, Fe, Cu, Ag, Au, and Pd induces compressive strain on the nanoparticle surface due to shorter Pt–Pt distances, thereby downshifting the d-band center of Pt.<sup>17,178,182,195,196</sup> The downshift of the Pt d-band weakens the adsorption of OH species, which are intermediates of the ORR, thereby facilitating the dissociation of H<sub>2</sub>O molecules from the catalyst surface to eventually increase the ORR reaction rate.<sup>18,192,196–199</sup> Stamenkovic *et al.* demonstrated that alloying Pt with transition metals can decrease the adsorption energy of oxygen on the top Pt layer of Pt<sub>3</sub>M (M = Ti, V, Fe, Co, Ni) alloys. The ORR activities followed the order Pt < Pt<sub>3</sub>Ti < Pt<sub>3</sub>V < Pt<sub>3</sub>Ni < Pt<sub>3</sub>Fe ≈ Pt<sub>3</sub>Co, demonstrating a volcano relationship.<sup>18</sup> However, the transition metal atoms on the surface of a Pt-based alloy catalyst usually undergo dissolution, resulting in low chemical stability for the catalyst.<sup>200,201</sup> More specifically, the dissolution of the transition metal from a Pt–M alloy results in a change in the surface composition and an increase in the surface roughness of the catalyst, therefore altering the initial ORR activity of the alloy electrocatalyst.<sup>17,200,202–204</sup> In 2009, Strasser *et al.* demonstrated that the electrochemical treatment of PtCu alloy nanoparticles results in preferential dissolution of the Cu component, forming dealloyed nanoparticles with a thin Pt skin over the PtCu alloy.<sup>202</sup> Wang *et al.* also reported the electrochemical dealloying of PtCu<sub>3</sub> intermetallic alloy nanoparticles. Fine tuning of the electrochemical cycling parameters resulted in dealloyed nanoparticles with various morphologies, such as solid or sponge-like nanoparticles with a Pt-rich shell, which showed enhanced ORR activity compared to the initial PtCu alloy nanoparticles.<sup>203</sup>

Whether the dissolution process improves or deteriorates the catalyst performance, the stability of the catalyst surface represents an important challenge in ORR electrocatalysts. In order to reinforce the surface of Pt-based alloy electrocatalysts, thermal treatments in which the non-noble metal atoms migrate to the sublayers of the catalyst have been used to form Pt-skin type surfaces.<sup>130,205–207</sup> The outward migration of the Pt atoms and inward migration of the transition metals create a reinforced surface, which can overcome the problems caused

by surface structure changes induced by transition metal dissolution.<sup>17,131,208</sup> Wang *et al.* reported the evolution of a Pt skin surface from PtNi alloy nanoparticles due to phase segregation by acid and thermal treatment.<sup>209</sup> The acid treatment of the PtNi alloy nanoparticles results in the formation of a Pt-skeleton on the nanoparticles. Subsequent thermal annealing of the acid-treated nanoparticles results in the formation of a multilayered Pt-skin on the nanoparticles, which showed enhanced ORR activity compared to Pt/C and PtNi alloy nanoparticles. In 2016, the *in situ* TEM observation of thermal facet healing of octahedral PtNi was reported.<sup>210</sup> Gan *et al.* characterized the *in situ* annealing of Pt<sub>1.5</sub>Ni nanoparticles from room temperature to 800 °C using transition electron microscopy (TEM). They observed the diffusion of Pt atoms from the corners toward the concave Ni-rich {111} facet. Based on these studies, the thermal treatment of Pt–M alloy nanoparticles results in outward atomic diffusion and phase segregation of Pt atoms.

The phase segregation between Pt and other metal atoms in Pt-based alloys can be also induced by acid leaching,<sup>120,211,212</sup> the binding of small molecules or ligands,<sup>37,130,213,214</sup> and applied potentials during electrochemical process<sup>142,202,204</sup> among other methods. Since the reversible core–shell phase reconstruction of RhPd binary nanoparticles by an oxidative or reductive atmosphere was reported in 2008,<sup>133</sup> the phase conversion of Pt-based alloy nanoparticles by changing the surrounding atmosphere has been widely studied. Ahmadi *et al.* reported the phase segregation behavior of Pt<sub>0.5</sub>Ni<sub>0.5</sub> octahedral nanoparticles during thermal annealing under vacuum, H<sub>2</sub>, and O<sub>2</sub> atmospheres *via* AFM and XPS.<sup>213</sup> The vacuum and O<sub>2</sub> atmospheres induced outward Ni migration at lower temperatures (<300 °C), resulting in the formation of Ni oxides at the surface. On the other hand, the H<sub>2</sub> atmosphere restricted Ni segregation to the surface at low temperatures due to the reduction of surface oxide species. Furthermore, they also demonstrated the effect of a CO atmosphere on the atomic diffusion behavior in octahedral PtNi nanoparticles during thermal treatment.<sup>214</sup> CO treatment at room temperature before annealing enhanced the thermal stability of the PtNi nanoparticles against coarsening. On the other hand, the presence of CO during annealing resulted the formation of Ni(CO)<sub>4</sub> species, which induced an initial phase segregation of Ni at temperatures below 400 °C. In the case of PtCo nanoparticles, the adsorbed CO molecules also induced phase segregation of Pt atoms at the nanoparticle surface.<sup>130</sup>

**3.1.1.2. Hollow Pt-based electrocatalysts *via* pre-synthesized templates.** In addition to the efforts to enhance their intrinsic catalytic properties, attempts to improve the inherent surface area of Pt-based electrocatalysts have also been carried out. One effective strategy to maximize the surface area of the catalyst is the formation of nanostructured electrocatalysts with a hollow interior. In general, the formation of hollow Pt-based catalysts is accomplished by the template-mediated growth of Pt atoms and subsequent removal of the template by acid etching or thermal annealing.<sup>51,52,54,215</sup> Wang *et al.* reported the synthesis of hollow dendritic Pt nanoparticles by chemical etching of

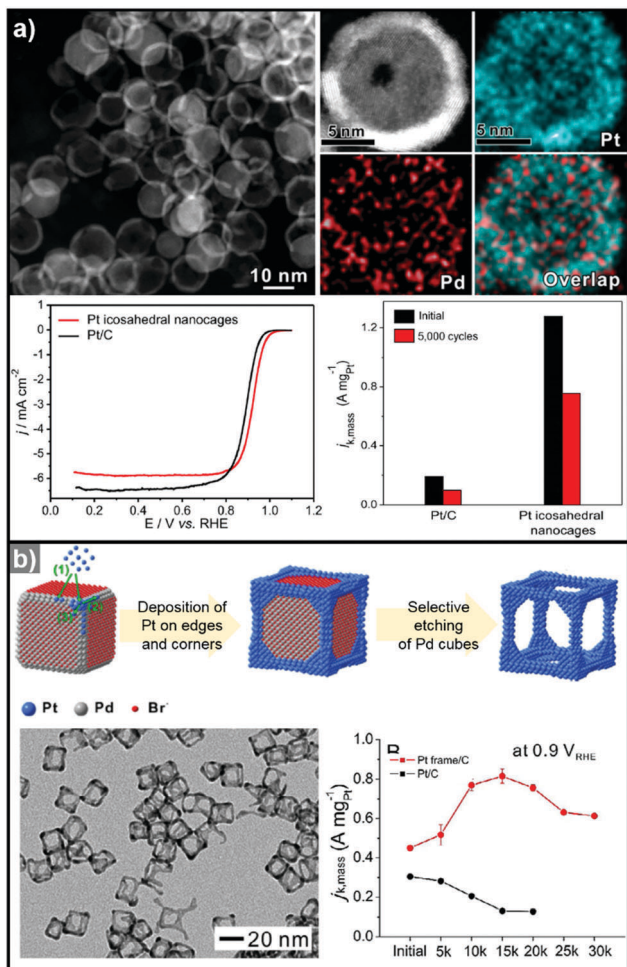


Fig. 8 Examples on hollow Pt-based nanostructures utilizing pre-synthesized templates. (a) PdPt icosahedral nanocage. (upper) HAADF-STEM image and its corresponding EDX elemental mapping image of Pt icosahedral nanocages. (lower) ORR polarization curves and mass activity comparison of Pt icosahedral nanocages and commercial Pt/C catalysts. Reproduced with permission from ref. 51. Copyright 2016 American Chemical Society. (b) Pt cubic nanoframe. (upper) Schematic illustration of the formation process of Pt cubic nanoframes. (lower) TEM image of Pt cubic nanoframes and ORR mass activity change of catalysts after different numbers of cycles of repeated potential sweeping during an accelerated durability test. Reproduced with permission from ref. 52. Copyright 2016 Wiley-VCH.

dendritic Pd@Pt core–shell nanoparticles.<sup>215</sup> Wang *et al.* reported the synthesis of icosahedral nanocages with an ultrathin Pt wall *via* the selective removal of the Pd component from Pd@Pt core–shell icosahedra utilizing  $\text{FeCl}_3$  and  $\text{KBr}$  (Fig. 8a).<sup>51</sup> The resulting nanocages exhibited a multiply twinned structure and a high surface area, and showed a 4-fold enhancement in ORR mass activity over the commercial catalyst Pt/C. Additionally, Park *et al.* demonstrated the synthesis of cubic Pt nanoframes utilizing cubic Pd nanoparticles as a template (Fig. 8b).<sup>52</sup> The site selective coverage of  $\text{Br}^-$  ions induces the selective deposition of Pt atoms on the edges and corners, and the Pt cubic nanoframes can then be obtained by selective removal of the Pd cubes using acid and  $\text{H}_2\text{O}_2$ . The resulting Pt cubic nanoframe showed an 8-fold enhancement in ORR mass activity over 15 000 cycles compared to Pt/C.

Galvanic replacement has also been successfully exploited for the preparation of hollow Pt-based nanostructures.<sup>50,94,97,151,216,217</sup> Hong *et al.* demonstrated fine control of the galvanic replacement reaction between Pd and Pt to form Pd–Pt nanoparticles with core–shell, dendritic, and cage morphologies.<sup>94</sup> They utilized octahedral and cubic Pd nanocrystals as templates, and showed that the concentration of the reducing reagent dictates the exchange behavior between Pd and Pt. The octahedral Pd–Pt nanocages showed the greatest improvement in ORR performance among the various Pd–Pt nanocrystals. Moreover, Zhang *et al.* reported fine control of the thickness of Pt nanocages fabricated using Pd nanoparticles as a template.<sup>50</sup> The number of the Pt atoms grown on the Pd nanoparticles was tuned from 1 to 6 atomic layers by controlling the reaction conditions that affect the growth, diffusion, and dissolution behavior of the Pt and Pd atoms.

**3.1.1.3. Hollow Pt-based electrocatalysts *via* *in situ* formed templates.** The usage of pre-synthesized templates such as Pd and Ag nanoparticles in the synthesis of hollow nanostructures has several limitations: (1) the synthetic process inevitably requires multiple steps of template synthesis, shell growth, and template removal, which limits its practical use. (2) The majority of strategies utilizing pre-synthesized templates are based on noble metals such as Pd and Ag as sacrificial templates, wasting expensive materials. (3) The final morphology of the hollow nanocage and nanoframe structures is limited to the initial morphology of the pre-synthesized template. In order to overcome these disadvantages and to further explore the possibility of fine-tuning the surface energies and the nanoscale phase mixing and segregation, the *in situ* formation of nanotemplates has been investigated for the synthesis of novel hollow nanostructures.

The one-pot synthesis of binary PtNi nanoparticles has led to a wide variety of nanoparticle morphologies. Interestingly, these binary nanocrystals are metastable, allowing the formation of the nanocrystals *in situ*, phase segregation, and even the removal of the template to give rise to the hollow nanostructures to be accomplished in one step. In 2014, Chen *et al.* demonstrated a one-pot process to prepare PtNi nanoframes that involved the formation of a  $\text{PtNi}_3$  polyhedron, the *in situ* erosion of the core into PtNi, and finally, the formation of a rhombic dodecahedral  $\text{Pt}_3\text{Ni}$  nanoframe with an extraordinarily high surface area (Fig. 9a).<sup>143</sup> The open-framework structure showed a phase-segregated Pt–skin structure, and exhibited a 36-fold enhancement in ORR mass activity as compared to commercial Pt/C. Ding *et al.* reported the preparation of PtNi nanoframes with tetrahedral (THH) or rhombic dodecahedral (RD) morphologies.<sup>142</sup> The final morphology of the PtNi nanoparticles was controlled by the ratio of oleylamine and oleic acid, with higher oleic acid concentration resulting in the THH morphology. The THH and RD PtNi nanoframes were obtained by simple acetic acid treatment to remove the Ni template, and the PtNi THH nanoframe showed enhanced ORR activity, with 20.9 times higher mass activity than commercial Pt/C.

As mentioned above, three-dimensional polyhedral nanoparticles consist of vertexes, edges, and facets, each of which

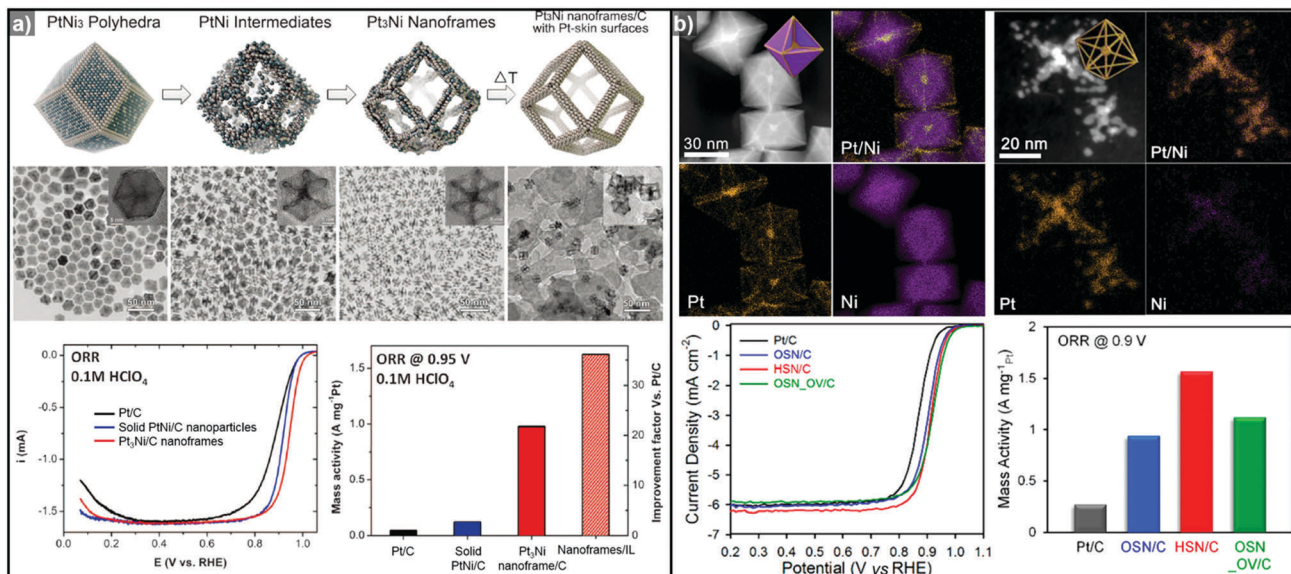


Fig. 9 Examples of  $\text{PtNi}$  nanoframes via *in situ* template-mediated methods. (a)  $\text{Pt}_3\text{Ni}$  rhombic dodecahedral nanoframes with thin Pt skin. (upper) Schematic illustration, TEM image of the formation process of  $\text{Pt}_3\text{Ni}$  rhombic dodecahedral nanoframes with thin Pt skin. (lower) ORR polarization curves and mass activities at 0.95 V vs. RHE of catalysts in 0.1 M  $\text{HClO}_4$  electrolyte. Reproduced with permission from ref. 143. Copyright 2014 AAAS. (b)  $\text{PtNi}$  octahedral nanoframe with Cartesian coordinates. (upper) HAADF-STEM image and corresponding EDX elemental mapping of  $\text{PtNi}$  octahedral nanoparticles and nanoframes with cartesian coordinates. (lower) ORR polarization curves and mass activities of catalysts at 0.9 V vs. RHE in 0.1 M  $\text{HClO}_4$  electrolyte. Reproduced with permission from ref. 37. Copyright 2015 American Chemical Society.

has a different energy state due to the difference in the number of coordinated adjacent atoms.<sup>218,219</sup> Therefore, phase segregation in three dimensional morphologies is more complicated than in a simple spherical nanoparticle. The complexity of the energy states in polyhedral nanoparticles enables site-specific phase segregation in Pt-based nanoparticles, and structurally advanced Pt-based hollow nanocages and nanoframes can be obtained by utilizing this phenomenon. In 2015, Oh *et al.* demonstrated the phase segregation behavior of an octahedral  $\text{Pt}@\text{Ni}$  core@shell nanoparticle under a CO atmosphere (Fig. 9b).<sup>37</sup> The presence of CO induces anisotropic phase segregation of Pt along  $\langle 100 \rangle$  directions, which forms Pt-based core with Cartesian coordinate-like morphology in  $\text{Pt}@\text{Ni}$  octahedral nanoparticle. The removal of the Ni component *via* acid treatment yielded an octahedral nanoframe structure with Cartesian coordinates, and this unique nanoframe showed improved ORR activity compared to commercial Pt/C. The anisotropic diffusion and growth of the Pt atoms in PtNi alloy nanoparticles with different morphologies were also reported by other groups. Niu *et al.* reported the anisotropic phase segregation and migration of Pt atoms during the synthesis of rhombic dodecahedral PtNi nanoframe structures.<sup>102,143</sup> During the formation process of the PtNi rhombic dodecahedra, the anisotropic growth and diffusion of Pt atoms were observed. In the initial stage of the synthesis, Pt-rich tetradecapods were formed in the core with their arms oriented towards the 14 vertices of the PtNi rhombic dodecahedra. The Pt atoms diffused outward and were relocated to the edges of PtNi rhombic dodecahedra, which could be further converted to rhombic dodecahedral nanoframe structures *via* the selective removal of Ni. Additionally, Wang *et al.* reported the preferential removal of the Ni component of

tetrahedrahedral (THH) PtNi nanoparticles using CO.<sup>144</sup> They suggested that Ni was preferentially removed from the  $\langle 100 \rangle$  direction using CO molecules; this process was facilitated by the lattice strain between the Pt thin shell and PtNi alloy core. The annealing of the PtNi THH nanoparticles in the presence of CO resulted in  $\text{Pt}_3\text{Ni}$  THH nanoframe structures that showed 8-fold greater ORR mass activity than commercial Pt/C.

*In situ* formed templates have also been used in PtCu systems. For instance, Zhang *et al.* reported the synthesis of five-fold-twinned PtCu nanoframes by a one-pot process.<sup>220</sup> The reaction process consisted of the *in situ* formation of a Cu-based five-fold twinned template and a subsequent Galvanic replacement process. The PtCu nanoframe catalysts showed higher ORR activity than commercial Pt/C and solid PtCu nanoparticles. Binary compositions such as PtCu<sup>221,222</sup> and PtCo<sup>124</sup> can also produce nanoframe structures with a rhombic dodecahedral morphology. The ORR activities of representative Pt-based electrocatalysts with and without hollow morphologies are summarized in Fig. 10 and Table 2.

**3.1.1.4. Limitations in Pt-based binary hollow nanostructures.** In general, Pt-based hollow nanostructures have shown much greater ORR catalytic activity in acidic electrolytes than commercial Pt/C. These catalysts benefit from both the high surface area and d-band center optimization of the PtM alloy composition. However, the ORR mass activity of hollow nanostructures is inferior to that of the world record catalyst, ultrafine jagged platinum nanowires ( $13.6 \text{ A mg}_{\text{Pt}}^{-1}$ ).<sup>223</sup> Moreover, due to their intrinsically high surface energies, nanoframe and nanocage structures are prone to collapse under the harsh acidic conditions used during electrocatalytic cycling.<sup>11,36,218,224</sup>

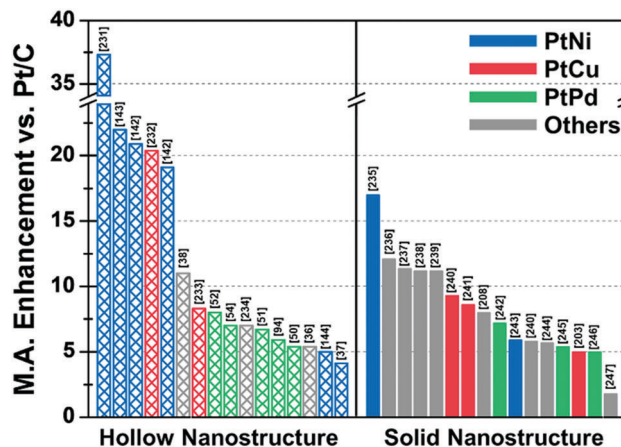


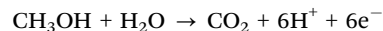
Fig. 10 Comparison of ORR mass activity enhancement vs. commercial Pt/C of various Pt-based multicomponent electrocatalysts. Detailed values of various catalysts are described in Table 2. References are denoted in the brackets.

Alloyed transition metal species such as Ni and Cu in the hollow nanostructures can dissolve during catalytic cycles, further complicating the issue of catalyst durability.<sup>201,224–226</sup> In short, although hollow-structured Pt-based ORR catalysts showed significant activity enhancement as compared to commercial Pt/C, there

are still great barriers to the further practical use of PEMFCs in terms of the performance and the structural and compositional stability of the catalysts. Further efforts are necessary to overcome the limitations of Pt-based hollow-structured ORR catalysts.

**3.1.2. Liquid fuel oxidation reaction.** The gaseous hydrogen fuel in PEMFCs can be replaced by liquid fuels such as methanol (direct methanol fuel cell, DMFC) and formic acid (direct formic acid fuel cell, DFAFC).<sup>227–229</sup> These liquid fuels are considered more suitable for small portable electronic devices due to their easily exchangeable fuel cartridges, high energy density, and fast charging rate.<sup>229,230</sup> In direct liquid fuel cells, the HOR reaction at the anode of PEMFCs is replaced by the methanol oxidation reaction (MOR) for DMFCs and the formic acid oxidation reaction (FAOR) for DFAFCs.

Methanol oxidation reaction (MOR):



Formic acid oxidation reaction (FAOR):



Despite the advantages described above, the practical use of the DMFC and DFAFC presents several challenges. The major

Table 2 Comparison of electrocatalytic activity of various Pt-based electrocatalysts toward ORR under 0.1 M  $\text{HClO}_4$

Structure	Catalyst	ECSA ( $\text{H}_{\text{upd}}$ ) ( $\text{m}^2 \text{g}_{\text{Pt}}^{-1}$ )	Mass activity @ 0.9 V vs. RHE ( $\text{A mg}_{\text{Pt}}^{-1}$ )	Mass activity enhancement vs. Pt/C	Specific activity @ 0.9 V vs. RHE ( $\text{mA cm}_{\text{Pt}}^{-2}$ )	Specific activity enhancement vs. Pt/C	Ref.
Hollow	Porous $\text{Pt}_3\text{Ni}_6$ NW/C-AA	66.8	5.6	37.3	8.38	38.4	231
	$\text{Pt}_3\text{Ni}$ RDH nanoframe/C	66 <sup>a</sup>	5.7	22	8.6	16	143
	PtNi THH nanoframe/C	45.3	2.95	20.9	6.37	25.9	142
	PtCu octopod nanoframe/C	54.8	3.26	20.4	5.98	21.4	232
	PtNi RDH nanoframe/C	54.6	2.69	19.1	4.93	19.9	142
	PtCu@PtCuNi dendrite@frame/C	33.8	2.48	11	7.33	16	38
	PtCu RDH nanoframe/C	53.9	1.08	8.3	1.7	2.3	233
	Pt cubic nanoframe/C (after 15k cycle)	70.1	0.82	8	1.17	2.9	52
	Pt icosahedral nanocage/C	45	1.12	7	2.48	10	54
	porous $\text{PtCuBiMn}$ nanosheet/C	28.6 <sup>a</sup>	0.69	7	2.41	10	234
	Pt icosahedral nanocage/C	36.6	1.28	6.7	3.5	10	51
	PdPt octahedral nanocage/C	40.3	1.2 <sup>c</sup>	5.9	2.98 <sup>c</sup>	6.7	94
	Pt octahedral nanocage/C	37.9	0.75	5.4	1.98	7.9	50
	Co–PtCu nanoframe/C	31	1.56	5.4	5.03	16.8	36
	PtNi THH nanoframe/C	18.4	0.47	5	2.55	8	144
	PtNi OSN_OV/C	28	1.12	4.1	4	11.1	37
Solid	9 nm $\text{Pt}_{2.5}\text{Ni}$ octahedra/C	31 <sup>b</sup>	3.3	17	10.6	81	235
	$\text{PtNi}_{0.56}\text{Pd}_{1.42}$ NWS/C	55.5	1.93	12.1	3.48	13.4	236
	$\text{PtPb}_{1.12}\text{Ni}_{0.14}$ octahedra/C	37.2	1.92	11.4	5.16	19.6	237
	$\text{Pd}_{0.42}\text{Ni}_{0.58}$ @Pt/C	42.1 <sup>b</sup>	1.45	11.2	0.61	2.7	238
	$\text{Pt}_2\text{CuNi}$ Oh/C	35.3	2.35	11.2	6.65	28.9	239
	$\text{Pt}_3\text{Cu}$ icosahedra/C	34.4	0.746	9.3 <sup>d</sup>	2.17	5.7 <sup>d</sup>	240
	PtCu octahedra/C	20 <sup>a</sup>	1.2	8.6	4.25	21.3	241
	Co@Pt nanoparticle/C	54	1.76	8	2.24	6.2	208
	Pd@ $\text{Pt}_{2.7\text{L}}$ icosahedra/C	47.1	0.64	7.2	1.36	7.8	242
	PtNi-Cl-2/C	37	1.01	5.9	2.69	13.5	243
	$\text{Pt}_3\text{Cu}$ octahedra/C	31.5	0.461	5.8 <sup>d</sup>	1.47	3.9 <sup>d</sup>	240
	$\text{PtFe}_{1.2}/\text{C}$	58.9	0.765	5.7	1.298	6.7	244
	Pd@ $\text{Pt}_{2.3\text{L}}$ /C	79	0.48	5.4	0.73	4.3	245
	Dealloyed $\text{PtCu}_3$ NP/C (after 100k cycle)	51.1	0.46	5	0.9	6	203
	Pd@Pt concave decahedra/C	95.9	1.6	5	1.66	4.6	246
	Ir@Pt nanoparticle/C	37	0.35	1.8	0.9	2.6	247

<sup>a</sup> Measured by CO-stripping method. <sup>b</sup> Measured by Cu under potential deposition method. <sup>c</sup> Mass and specific activity @ 0.85 V vs. RHE.

<sup>d</sup> Compared with Pt black.

problem is the partial oxidation of the liquid fuels, which results in sluggish oxidation reaction kinetics and also reduces the number of transferred electrons.<sup>228,230</sup> In the DMFC, less than 30% of the energy can be exploited as electricity.<sup>248</sup> Another major concern is the crossover of the fuel molecules from the anode to the cathode *via* diffusion through the proton exchange membrane in the cell.<sup>249–251</sup> This crossover phenomenon not only reduces the overall cell voltage, but also

contaminates the cathode electrocatalysts. The partial oxidation of liquid fuels produces carbon monoxide (CO), which strongly adsorbs onto the surface of cathode catalyst, deteriorating the ORR performance of the cathode during cell operation. This phenomenon is called CO-poisoning, and many studies have addressed this issue.<sup>230,250</sup>

Binary Pt-based alloy phases such as PtRu and PtCu are known to have CO-tolerant surfaces and thus show promising activity for the MOR.<sup>230,252–257</sup> The aforementioned strategies to fabricate hollow nanostructures have also been exploited to generate high-performance MOR catalysts.<sup>222,258</sup> Li *et al.* also demonstrated the preparation of a crystalline PtCu alloy with a porous nanotube structure with highly open structured surfaces using Cu nanowires as the template (Fig. 11a).<sup>259</sup> The porous PtCu nanotubes showed 5.5 and 10.3 times greater mass activity and specific activity, respectively, toward the MOR compared to commercial Pt/C, due to their three dimensional accessible surface. Xia *et al.* reported a one-pot synthetic method to prepare cubic PtCu<sub>3</sub> nanocages, which showed a higher oxidation current density (14.1 mA cm<sup>-2</sup>) than solid PtCu nanoparticles (8.4 mA cm<sup>-2</sup>) and commercial Pt catalysts (12.8 mA cm<sup>-2</sup>).<sup>260</sup> Moreover, the PtCu<sub>3</sub> nanocage catalysts generated less CO-poisoning surface energy states compared to commercial Pt catalysts, which is derived from electrochemical dealloying of PtCu<sub>3</sub> phase in initial stage of electrocatalysis. The MOR activities of representative Pt-based electrocatalysts with hollow interiors are summarized in Table 3.

On the other hand, Pd-based electrocatalysts are widely known to give the best performance for the FAOR.<sup>261,262</sup> DFAFC devices exploiting Pd-based catalysts can generate energy density performances comparable to those of DMFCs.<sup>227,263,264</sup> Therefore, the development of Pd-based nanocatalysts to enhance the catalytic activity of the FAOR has been actively pursued.<sup>265–267</sup> In particular, hollow nanostructures of Pd and Pd-based alloys have demonstrated improved FAOR activity compared to commercially available Pd/C catalysts.<sup>268–273</sup> For example, Wang *et al.* reported the synthesis of well-defined Pd nanoframes by controlling the rates of etching and the regrowth process (Fig. 11b).<sup>268</sup> The resulting octahedral Pd nanoframe catalyst showed a 7.5-fold increase in peak current density compared to a solid Pd octahedral nanoparticle catalyst. Liu *et al.* also reported the synthesis of hollow cubic PdAg alloy

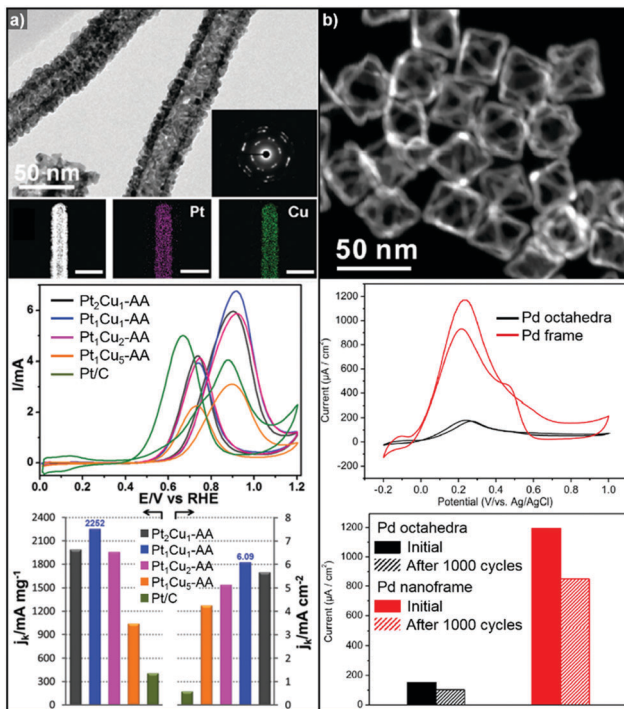


Fig. 11 Examples of MOR and FAOR electrocatalysts with hollow structures. (a) PtCu porous nanotube. (upper) TEM, HAADF-STEM image and corresponding EDX elemental mapping of PtCu porous nanotubes. (middle) Polarization curves of MOR of PtCu nanotube catalysts. (lower) MOR mass and specific activity comparison of catalysts. Reproduced with permission from ref. 259. Copyright 2017 Royal Society of Chemistry. (b) Pd octahedral nanoframes. (upper) TEM image of Pd octahedral nanoframes. (middle) Polarization curves of FAOR of Pd octahedra and nanoframes. (lower) FAOR current density comparison of Pd octahedra and nanoframes. Reproduced with permission from ref. 268. Copyright 2016 American Chemical Society.

Table 3 Comparison of electrocatalytic activity of various hollow Pt-based electrocatalysts toward MOR under acidic electrolyte

Catalyst	Electrolyte	ECSA (H <sub>upd</sub> ) (m <sup>2</sup> g <sub>Pt</sub> <sup>-1</sup> )	Mass activity @ 0.9 V vs. RHE (A mg <sub>Pt</sub> <sup>-1</sup> )	Mass activity enhancement vs. Pt/C	Specific activity @ 0.9 V vs. RHE (mA cm <sub>Pt</sub> <sup>-2</sup> )	Specific activity enhancement vs. Pt/C	Ref.
Concave PtCu <sub>2</sub> nanoframes/C	0.5 M H <sub>2</sub> SO <sub>4</sub> + 1.0 M CH <sub>3</sub> OH	44.5	3.36	7	7.5	7.2	247
Pt <sub>1</sub> Cu <sub>1</sub> nanotubes/C	0.5 M H <sub>2</sub> SO <sub>4</sub> + 1.0 M CH <sub>3</sub> OH	38	2.25	5.5	6.09	10.3	259
PtPd dendritic nanocages/C	0.5 M H <sub>2</sub> SO <sub>4</sub> + 1.0 M CH <sub>3</sub> OH	—	0.58	5.27 <sup>a</sup>	1.36	2.67 <sup>a</sup>	215
Hollow-PtCu/C	0.5 M H <sub>2</sub> SO <sub>4</sub> + 1.0 M CH <sub>3</sub> OH	—	0.89	3.74	1.77	4.46	258
Co–PtCu RDH nanoframes/C	0.1 M HClO <sub>4</sub> + 1.0 M CH <sub>3</sub> OH	31	4.11	3.7	13.3	9.7	36
PtNi RDH nanoframes/C	0.1 M HClO <sub>4</sub> + 0.2 M CH <sub>3</sub> OH	54.6	1.04	3.25	1.9	3.39	142
PtNi THH nanoframes/C	0.1 M HClO <sub>4</sub> + 0.2 M CH <sub>3</sub> OH	45.3	0.84	2.63	2.19	3.91	142
PtCu RDH nanoframes/C	0.1 M HClO <sub>4</sub> + 1.0 M CH <sub>3</sub> OH	41.3	0.98	1.72	2.35	2.77	222

<sup>a</sup> Compared with Pt black.

nanocages by galvanic exchange utilizing Ag nanocubes as the template.<sup>269</sup> The cubic PdAg nanocages showed improved electrocatalytic FAOR activity and enhanced CO-tolerance, which stem from the high surface area and significant change in the adsorption energy of the intermediates in the PdAg alloy system. Huang *et al.* also reported one-pot synthesis of hollow PdPt alloy nanocubes *via* galvanic replacement reaction of Pt toward *in situ* formed Pd nanocubes.<sup>274</sup> The reduction rate of Pt and diffusion rate of Pd atoms were fine-controlled by halide ligands and reaction temperature, which resulted hollow nanocube structure with PdPt alloy phase. The hollow PdPt nanocube showed two-fold enhancement of FAOR current density compared to PdPt solid nanocube.

### 3.2. Electrolytic water splitting reactions

**3.2.1. Oxygen evolution reaction (OER).** The water splitting reaction involves the OER ( $O_2 + 4H^+ + 4e^- \rightarrow 2H_2O$ ) and the HER ( $2H^+ + 2e^- \rightarrow H_2$ ), and requires a theoretical potential of 1.23 V (HER at 0 V and OER at 1.23 V *vs.* reversible hydrogen electrode; RHE). The OER involves the transfer of four electrons and has slower reaction kinetics than the HER, which renders the development of highly active OER catalysts one of the most important challenges in water electrolyzer technologies.<sup>9,275</sup> Similar to the ORR, proposed OER mechanisms commonly involve the formation of surface metal oxide/hydroxide complexes. While Pt-based catalysts show great performance in the ORR, they exhibit only marginal catalytic activity in the OER. In the high potential range of the OER (generally, over 1.8 V in state-of-the-art electrolyzers), metals including Pt are oxidized to form other phases which have different surface structures and energies and can be dissolved into the reaction solution as ionic complexes. On the other hand, metal oxides have been used as OER catalysts due to their high stability under the OER operating conditions.<sup>276–279</sup> Representative OER catalysts include  $IrO_2$  and  $RuO_2$  in acidic electrolytes, and oxides or oxyhydroxides of transition metals (Ni, Co, and Fe) in alkaline electrolytes.<sup>280–284</sup> For alkaline water electrolyzers, highly active, cost-effective catalysts based on transition metals have been identified. Song *et al.* reported the synthesis of NiFe, NiCo, and CoCo double layered hydroxide (LDH) nanosheets by exfoliating bulk hydroxides *via* a topochemical approach using various anions ( $Br^-$  and  $CO_3^{2-}$ ).<sup>285</sup> The exfoliated LDH nanosheets exhibited different OER activities ( $NiFe > NiCo > CoCo$ ) in 1 M KOH solution, and showed 4.5-, 3.4-, and 2.6-fold higher current density than  $IrO_2$  at 300 mV of overpotential due to the combination of a large surface area and numerous active sites. Furthermore, Zhang *et al.* developed gelled metal oxyhydroxides (W, Co, and Fe) with exceptionally high OER activities by tuning the OH adsorption energies of binary and ternary oxyhydroxide materials.<sup>286</sup> The gelled FeCoW oxyhydroxide (G-FeCoW) showed excellent catalytic activity and required only 191 mV of overpotential to reach  $10\text{ mA cm}^{-2}$ , and remained stable over 500 hours of reaction. These results show that transition metal based catalysts are very promising for alkaline water electrolysis, with affordable prices and good stability in alkaline solution.

Only a limited number of catalysts can operate stably in water electrolysis using acidic electrolytes, which are relevant to PEM water electrolyzers (PEMWES).  $IrO_2$  and  $RuO_2$  have shown the most pronounced catalytic activity for the OER.<sup>287–291</sup> Similar to other catalytic reactions, the OER benefits from increased surface area of catalysts. Accordingly, a few OER catalysts with hollow structures have been developed. Wang *et al.* synthesized hollow NiIr nanocrystals with Ir:Ni ratios of  $Ni_{2.76}Ir$ ,  $Ni_{2.53}Ir$ ,  $Ni_{1.43}Ir$ , and  $Ni_{0.93}Ir$  *via* Ni template mediated Ir growth.<sup>292</sup> The as-synthesized NiIr nanocrystals were oxidized electrochemically to form Ni-doped  $IrO_x$  nanocrystals.<sup>293</sup> The  $Ni_{2.53}Ir$  nanocrystal contained the greatest amount of active Ir sites among the prepared samples and exhibited the best OER activity, in part due to the large active surface area and the Ni dopant, which optimized surface d-band structure for oxygen evolution. Jin *et al.* reported the synthesis of IrNi alloyed nanoframe structures by growing Ir on Ni template, with the aid of a lanthanide metal complex as a passivation agent on the facets of the Ni template (Fig. 12a).<sup>294</sup> The site-selective growth of Ir on the edge and corner regions of the template induced the formation of an Ir-based frame structure, which is obtained by acid etching of the Ni template. The synthesized IrNi nanoframe showed twice the surface area of commercial Ir/C as informed by CO stripping analysis, and demonstrated much better OER activity than Ir/C.

Cu can also serve as a good template material for the formation of hollow structured OER catalysts due to its metastable nature.<sup>55,103</sup> Park *et al.* reported the synthesis of a truncated octahedral RhCu nanoframe using Cu as the template material.<sup>104</sup> The truncated octahedral RhCu nanoframes had three times the surface area of  $Cu@Rh$  core-shell nano-octahedrons, and showed more than twice the mass activity for the OER. Furthermore, Wang *et al.* reported the OER activities of a series of IrCu nanocages with various Ir:Cu ratios ( $Cu_{0.66}Ir$ ,  $Cu_{0.86}Ir$ ,  $Cu_{0.95}Ir$ ,  $Cu_{1.11}Ir$ ,  $Cu_{1.41}Ir$ , and  $Cu_{2.04}Ir$ ).<sup>295</sup> The  $Cu_{1.11}Ir$  nanocage showed the best OER performance among the compared catalysts in 0.05 M  $H_2SO_4$ , with 1.2 and 2.65 times higher mass activity than  $Cu_{1.41}Ir$  and Ir black, respectively. Evaluation of the Ir(III–IV) redox peak current indicated that the  $Cu_{1.11}Ir$  nanocage had the highest number of active Ir sites among the composition-controlled samples. This was responsible for the enhanced OER activity, thereby demonstrating the effectiveness of a hollow morphology in boosting catalytic activity for the OER.

Ternary alloy systems based on hollow/frame structures have also been developed by template-mediated syntheses. Feng *et al.* synthesized IrCo, IrNi, and IrCoNi hollow nanoparticles by etching solid particles of IrCo, IrNi, and IrCoNi using  $Fe^{3+}$  ions (Fig. 12b).<sup>296</sup> They demonstrated transition-metal dependent OER activity enhancement by comparing the calculated binding energies of OH, O, and OOH on the IrCoNi and Ir surfaces. When Ir is alloyed with transition metals, the stable binding of oxygen on pure Ir becomes weaker, with the binding energies following the order  $IrCoNi < IrCo < IrNi < Ir$ . The hollow IrCoNi structures showed the best OER activity. Kwon *et al.* demonstrated that a transition metal dopant can serve as a morphology engineering agent as well as a catalysis promoter.<sup>297</sup> The Cu core component of an octahedral  $Cu@Ir$

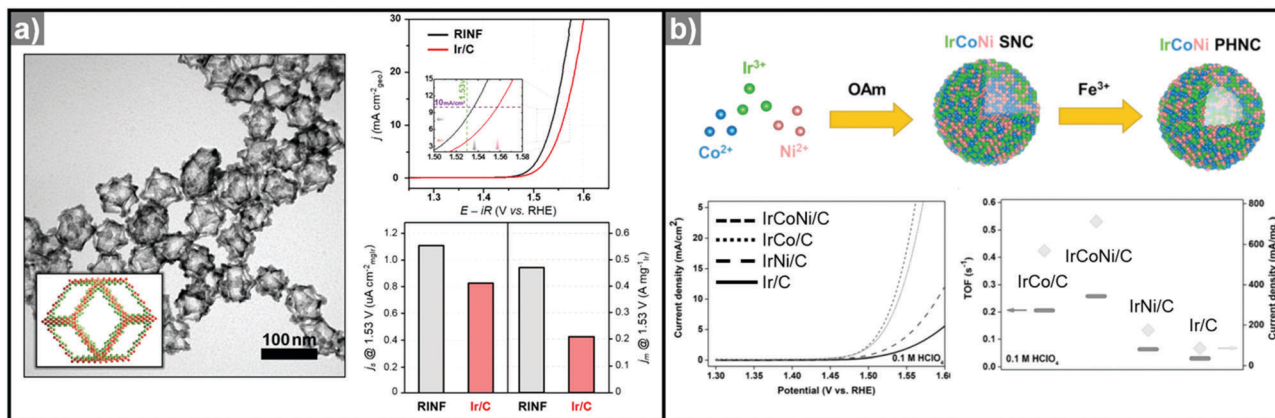


Fig. 12 (a) TEM image of IrNi nanoframe with graphical model in the inset and comparison of its OER activity with Ir/C (right; up). Specific activity and mass activity of IrNi nanoframe and commercial Ir/C are compared at 1.53 V (right; down). Reproduced with permission from ref. 294. Copyright 2017 Elsevier. (b) Scheme for the synthesis of IrCoNi multimetallic porous hollow nanocrystals and comparison of their OER activities (down; left) and turnover frequency (TOF) values and current densities of OER normalized to the mass of Ir (down right). Reproduced with permission from ref. 296. Copyright 2017 Wiley-VCH.

core–shell nanoparticle could not be leached due to the impermeable nature of the Ir shell.<sup>101</sup> This impermeable shell could be made permeable *via* the introduction of cobalt as a dopant in the synthesis, which allowed the deposition of Ir as well as Co in the shell layer on the Cu core.<sup>297</sup> Upon etching, the majority of the Co atoms in the shell layer were removed, and consequently the Cu core could be removed by the penetration of the etchant into the core. The resulting Co–IrCu nanocages showed a large active surface area and high OER activity. Park *et al.* also synthesized double nanoframe and single nanoframe structures of IrNiCu *via* precise control of the reduction rates of multiple precursors.<sup>298</sup> The synthesized double and single nanoframe structures exhibited surface areas almost three-fold and two-fold larger than that of Ir/C, respectively. The IrNiCu double nanoframe exhibited better OER activity than the single nanoframe and Ir/C, which demonstrates the straightforward advantage of increased surface area in driving high OER activity. The OER activities of representative Ir-based electrocatalysts with and without hollow morphologies are summarized in Table 4 and Fig. 13.

**3.2.2. Hydrogen evolution reaction.** The major research thrust in the development of HER catalysts lies in finding cost-effective and stable alternatives to Pt catalysts. Some metal sulfide and metal phosphide materials have shown promising HER activities and stabilities. For example, Ni<sub>5</sub>P<sub>4</sub> nanocrystals exhibited similar HER performance to that of Pt/C in 1 M H<sub>2</sub>SO<sub>4</sub> with a negligible overpotential,<sup>304</sup> and structurally engineered MoS<sub>2</sub> nanosheets exhibited great activity and stability for the HER.<sup>305–309</sup> There are very few examples of hollow or framework-like sulfide/phosphide HER catalysts. Yoon *et al.* reported the synthesis of a facet-controlled hollow Rh<sub>2</sub>S<sub>3</sub> hexagonal nanoprisms by a one-pot synthetic method using Cu<sub>1.94</sub>S as an *in situ* generated template.<sup>310</sup> The hollow Rh<sub>2</sub>S<sub>3</sub> nanoprism showed high HER activity and durability in an acidic electrolyte due to the intrinsic active sites on Rh<sub>2</sub>S<sub>3</sub>. Interestingly, the HER activity was further enhanced during the cycling test because of the dissolution of residual Cu from the catalyst, maximizing the active surface sites. Liu *et al.* reported the synthesis of a Co phosphide hollow polyhedron by the phosphidation of a

Table 4 Comparison of OER activity of Ir-based hollow/solid electrocatalysts under acidic electrolyte

Structure	Catalyst	Electrolyte	Ir loading ( $\mu\text{g cm}^{-2}$ )	Overpotential (mV @ 10 mA cm $^{-2}$ )	Mass activity ( $\text{A mg}_{\text{Pt}}^{-1}$ @ 300 mV)	Ref.
Hollow	Co–IrCu ONC/C	0.1 M HClO <sub>4</sub>	20	293	0.64	297
	IrNiCu DNF/C	0.1 M HClO <sub>4</sub>	20	303	0.46	298
	IrNiCu SNF/C	0.1 M HClO <sub>4</sub>	20	306	0.4	298
	IrNi–RF/C	0.1 M HClO <sub>4</sub>	15.8	313.6	0.47	294
	IrCoNi PHNC/C	0.1 M HClO <sub>4</sub>	10	303	0.72	296
	Cu <sub>1.11</sub> Ir	0.05 M H <sub>2</sub> SO <sub>4</sub>	140	286	0.1	295
Solid	Ni <sub>2.53</sub> Ir NC	0.05 M H <sub>2</sub> SO <sub>4</sub>	10	302	0.11	292
	Ir–Ni TL/C	0.05 M H <sub>2</sub> SO <sub>4</sub>	2	350 (@ 5 mA cm $^{-2}$ )	1.2 (@ 280 mV)	299
	IrNi NP	0.05 M H <sub>2</sub> SO <sub>4</sub>	2	370 (@ 5 mA cm $^{-2}$ )	0.49 (@ 280 mV)	299
	IrNiO <sub>x</sub> /Meso-ATO-180	0.05 M H <sub>2</sub> SO <sub>4</sub>	10.2	330	0.1	293
	Cu–IrO <sub>2</sub>	0.1 M HClO <sub>4</sub>	140	351	0.05 (@ 350 mV)	300
	Ir-ND/ATO (at 280 mV)	0.05 M H <sub>2</sub> SO <sub>4</sub>	10.2	400	0.18	301
	IrO <sub>x</sub> /ATO	0.05 M H <sub>2</sub> SO <sub>4</sub>	10.2	360	0.1	279
	DO–IrNi <sub>3.3</sub>	0.1 M HClO <sub>4</sub>	10.2	310	0.62	302
	IrO <sub>x</sub> –Ir	0.5 M H <sub>2</sub> SO <sub>4</sub>	133	290	0.1	303

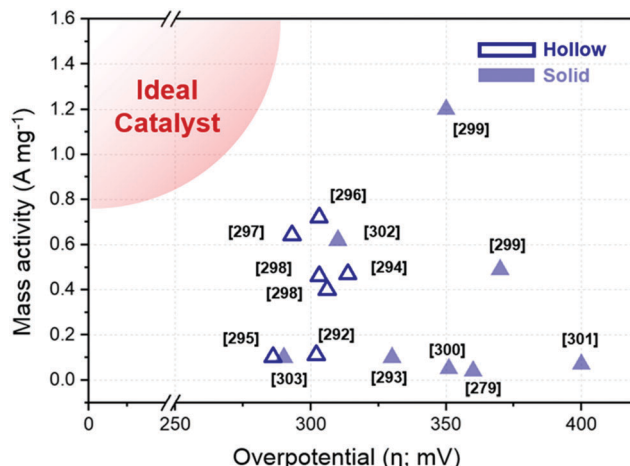


Fig. 13 Comparison of overpotential and mass activity of Ir based OER catalysts in terms of morphology (hollow or solid) in acidic electrolyte. Detailed values of various catalysts are described in Table 4. References are denoted in the brackets.

Co-containing zeolitic imidazolate framework (ZIF-67) at 250 °C for 2 hours. The resulting hollow CoP polyhedrons exhibited good HER activity with an overpotential of 159 mV at 10 mA cm<sup>-2</sup>.<sup>311</sup> Popczun and Callejas *et al.* reported a solvothermal synthetic method to produce hollow CoP<sup>312</sup> and FeP<sup>313</sup> nanoparticles at a very high temperature of 300–340 °C. The hollow morphology was formed by the phosphidation of *in situ* formed metal nanoparticles *via* the Kirkendall effect. The resulting hollow metal phosphide nanocatalysts exhibited excellent HER activities in 0.5 M H<sub>2</sub>SO<sub>4</sub> with an overpotential of less than 100 mV to reach a current density of 10 mA cm<sup>-2</sup>. An attempt to form hollow structures with abundant active sites was undertaken using Cu<sub>7</sub>S<sub>4</sub> as an *in situ* template.<sup>314</sup> Xu *et al.* reported ultra-small donut-shaped Cu<sub>7</sub>S<sub>4</sub>@MoS<sub>2</sub> nanoframe structures with numerous active MoS<sub>2</sub> edge sites. The hetero-nanoframe catalysts showed high HER activity with a current density of 200 mA cm<sup>-2</sup> at an overpotential of 206 mV.<sup>314</sup>

Noble metal based hollow or frame-like nanocrystals with HER activity comparable to that of Pt/C in an acidic electrolyte have also been reported.<sup>125,275,276</sup> Zhang *et al.* demonstrated the synthesis of necklace-like hollow Ni<sub>x</sub>Ru<sub>y</sub> nanoalloys by the galvanic replacement of Ni nanochain template nanoparticles with Ru and the Kirkendall effect.<sup>315</sup> Among a number of studied compositions, Ni<sub>43</sub>Ru<sub>57</sub> nanoalloys required the lowest overpotential, with 41 mV of overpotential at a current density of 10 mA cm<sup>-2</sup> and a Tafel slope value (31 mV dec<sup>-1</sup>) comparable to commercial Pt/C. Furthermore, Yoon *et al.* showed the promising HER activity of metallic Ru supported on copper sulfide nanoplates in alkaline electrolyte.<sup>316</sup> In addition to the synthesis of non-Pt metal catalysts, the strategy of using Pt based alloys to lower the Pt content can be used to achieve cost reduction for catalyst synthesis while meeting catalyst performance requirements. Oh *et al.* reported the preparation and catalytic activities of PtNiCo and PtNi nano-hexapods, which showed lower overpotentials and 7 and 6 times higher exchange current densities than commercial Pt/C, respectively.<sup>125</sup> The PtNiCo

hexapods showed better performance than the PtNi hexapods due to the synergistic effect of Ni and Co in tuning the surface formation energy of Pt-OH<sub>ad</sub>. Also, Cao *et al.* reported the preparation and catalytic activity of monocrystalline PtNi branched nanocages, which showed lower overpotentials and 2.5 times higher mass current density than commercial Pt/C at 100 mV overpotential.<sup>317</sup> The enhanced alkaline HER activity of PtNi branched nanocage stems from large surface area and synergistic effect of Pt-Ni(OH)<sub>2</sub>, which facilitates the dissociation of H<sub>2</sub>O and the formation of H<sub>ad</sub> species on the catalyst.

#### 4. The issue of catalyst stability during the electrocatalysis

As described in the preceding sections, hollow nanoparticles with cage and frame structures can provide an avenue to highly active nanocatalysts. However, prolonged electrochemical operation can cause serious stability issues in hollow nanocatalysts, leading to unreliable catalytic performance.<sup>18,218,318,319</sup> It can also induce unwanted phase segregation in the alloy nanoparticle, exposing certain phases with higher stability under electrocatalysis conditions. This can potentially lead to the leaching of certain constituent metal species from the dealloyed nanoparticle, leading to the formation of an electrochemically inactive nanocatalyst.

As a representative example of the nanocatalyst stability issue, in 2013, Cui *et al.* discovered that shape-controlled PtNi alloy nanoparticles form Pt-rich domains along their active sites such as corners and edges during electrocatalysis, whereas their Ni atoms are segregated to the facets.<sup>218</sup> The selectively leached Ni phases at the facets induced the formation of a concave facet structure, providing more active sites than the solid PtNi alloy nanoparticles. However, the authors also suggested that the collapse of the near-surface alloy structure in the Ni-rich octahedrons affects the surface adsorption of oxygen in a detrimental way and thus finally degrades the ORR catalytic activity. Escudero-Escribano *et al.* suggested that Pt overlayers are formed on the alloy nanoparticle surface during electrocycling tests even in Pt-based alloys synthesized through the sputter cleaning method.<sup>318</sup> With repeated cycling, the structural features of nanocatalysts can be altered because leachable metal phases become segregated in the core due to their dissolution at the surface. Furthermore, this structural degradation can cause a decrease in the electrochemically active surface area (ECSA), resulting in catalytic activities inferior to those measured at an initial stage. Mayrhofer and Stamenkovic *et al.* reported that the long-term stability of Pt-based bimetallic nanoparticles could affect the agglomeration of the particles and the leaching of the non-noble metal components.<sup>18,319</sup> They compared the surface compositions of used and unleached Pt<sub>3</sub>Co nanoparticles after the cycling test. The dynamic oxidizing conditions induced the segregation of Co at the surface, while Pt was segregated at the surface under a reducing CO atmosphere, which is used in the synthetic conditions.

The unit cell transformation of noble metal catalysts during electrocatalysis is also regarded as a critical factor in the decrease of their structural stability, and is mainly observed in the OER.<sup>279,298</sup> Among the noble metal based water splitting electrocatalysts, Ir- and Ru-based oxide catalysts exhibit the highest electrocatalytic activities toward the OER.<sup>9,280,320</sup> Recently, electrochemically oxidized Ir nanoparticles were demonstrated to have superior stability and activity to metallic Ir and thermally oxidized  $\text{IrO}_2$  nanoparticles.<sup>321</sup> The difference in catalytic activity was ascribed to the altered corrosion mechanism. The thermally oxidized  $\text{IrO}_2$  nanoparticles showed drastic dissolution in acidic media before 0.9 V vs. RHE. At OER relevant potentials, both air-oxidized and thermally oxidized Ir nanoparticles were dissolved, predominantly through the formation of unstable  $\text{Ir}^{(IV)}$  species. In contrast, the electrochemical oxidation of Ir nanoparticles formed the stable  $\text{Ir}^{(III)}$  species, which has ability to be reduced. The inevitable oxidation from Ir to  $\text{IrO}_x$  during the oxidation process poses a serious obstacle to attempts to utilize Ir or Ru-based metal nanoframes as OER catalysts. The three-dimensional morphologies of Ir or Ru alloy-based nanoframes might be destroyed during long-term stability test, because the unit cell structures of Ir(cubic) and  $\text{IrO}_x$  (rutile) are drastically different.

While there are cases in which electrochemical operation actually improves the catalytic performance of alloy nanocatalysts, the surface composition changes of alloy systems and the deformation of hollow or cage nanostructures are, in general, formidable obstacles to the development of active and durable catalysts. In order to solve the problems associated with the structural and compositional changes of nanocatalysts,

several ingenuous strategies have emerged, as described in the following sections.

#### 4.1. Multimetallic nanocrystals

Preservation of the structural integrity of innately unstable nanoframes during electrochemical operation is a daunting challenge. In order to endow such materials with stability, the introduction of an additional metal dopant has recently been attempted.<sup>35,288,322</sup> The introduction of a dopant into noble metal-based alloy nanoparticles not only obstructs atomic rearrangement during electrocatalysis but also produces robust ternary or quaternary alloy phases that are remarkably stable toward fuel cell and water splitting applications.

**4.1.1. Dopant inhibiting unwanted phase segregation during electrocatalysis.** Doping strategies have been widely investigated in electrocatalysis, because they can introduce additional functionality to the exposed surfaces of nanoparticles.<sup>323,324</sup> However, the presence of a dopant changes the electronic structure of the catalyst surface, and the resulting surface energy change might induce unwanted atomic rearrangement in the alloy nanoparticles during electrocatalysis.<sup>35,288,322</sup> In order to mitigate this phenomenon, several researchers have proposed alternative synthetic methodologies. In 2015, Huang *et al.* reported the synthesis of transition metal (Mo)-doped  $\text{Pt}_3\text{Ni}$  octahedral nanoparticles that exhibit high electrocatalytic performance toward the ORR (Fig. 14a).<sup>322</sup> They proposed that the Mo atoms prefer to be segregated at the edges or vertices of the octahedral  $\text{Pt}_3\text{Ni}$  nanoparticles, thereby stabilizing both Pt and Ni atoms against dissolution during the cycling test. Beermann *et al.* suggested that the addition of Rh into PtNi octahedral nano-

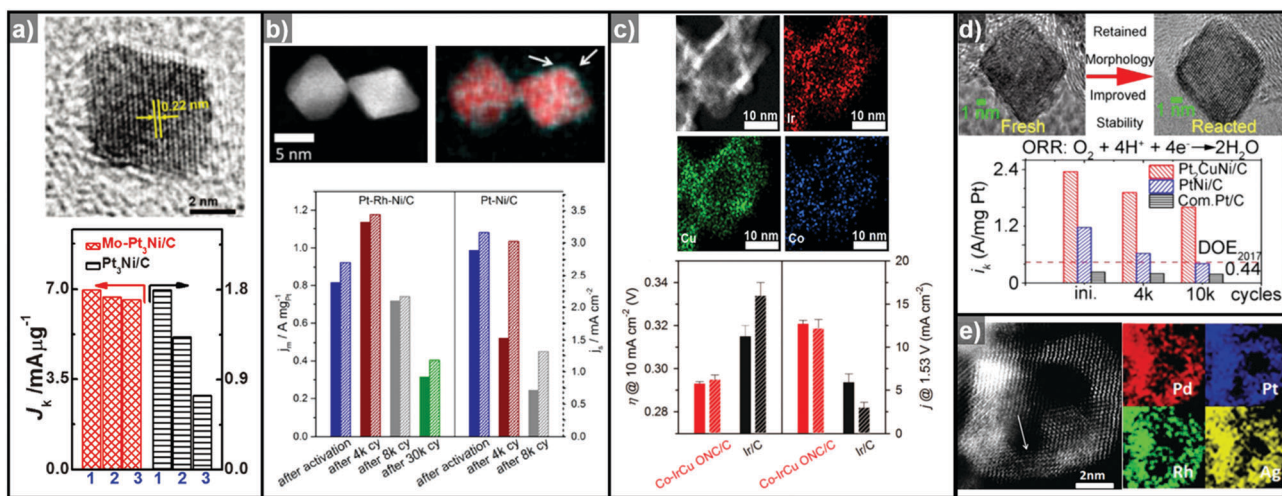


Fig. 14 Examples of multicomponent nanoparticles with high electrocatalytic stability, enabled by doping or alloying process. (a) TEM image of Mo-doped  $\text{Pt}_3\text{Ni}/\text{C}$  octahedra and its mass activity after electrocatalytic cycling test toward ORR. Reproduced with permission from ref. 322. Copyright 2015 AAAS. (b) TEM image and corresponding elemental mapping analysis of Rh-doped  $\text{PtNi}/\text{C}$  octahedra. The bar graphs indicate the mass activity and specific activity of Rh-doped  $\text{PtNi}/\text{C}$  octahedra. Reproduced with permission from ref. 35. Copyright 2016 American Chemical Society. (c) HAADF-STEM and corresponding elemental mapping analysis of Co-doped  $\text{IrCu}$  nanocage. (d) Bar graphs indicate the comparison of overpotentials to drive  $10 \text{ mA cm}^{-2}$  and current densities at 1.53 V (vs. RHE) between the samples. Reproduced with permission from ref. 297. Copyright 2017 Wiley-VCH. (e) TEM images of  $\text{Pt}_2\text{CuNi}/\text{C}$  octahedra before and after electrocatalysis. The enhanced electrocatalytic stability driven from the ternary alloy phase is described below the TEM images. Reproduced with permission from ref. 239. Copyright 2015 American Chemical Society. (e) STEM image and corresponding elemental mapping analysis of tetrametallic  $\text{PtPdRhAg}$  nanocages. Reproduced with permission from ref. 325. Copyright 2017 Wiley-VCH.

particle could enhance the electrocatalytic stability toward ORR (Fig. 14b).<sup>35</sup> Because the Rh dopants located at the surface of the nanostructures suppress the segregation of Pt at the surface, the diffusion of the Pt atoms during the electrocycling test is impeded, resulting in greater structural robustness for the PtNi nanoparticle. The octahedral morphology of Rh-doped PtNi remained unchanged even after 30 000 cycles, while the reference PtNi octahedral particles completely lost their shape under the same conditions. Oh *et al.* reported that Co atoms could also suppress the atomic migration of Pt atoms by alloying with Ni phase on the surface of PtNi octahedra.<sup>125</sup> Consequently, the Cartesian-coordinate-like hexapod shaped PtNiCo alloy nanostructures showed high electrocatalytic activity and stability toward the HER and ORR in alkaline media. Kwon *et al.* synthesized Co-doped IrCu hollow nano-frames that showed excellent electrocatalytic activity and long-term durability for the OER in acidic media (Fig. 14c).<sup>297</sup> The introduced Co dopant provides structural integrity to the surface iridium oxide under OER conditions. Similarly, Seitz *et al.* reported that the formation of highly active surface layers such as  $\text{IrO}_3$  or anatase  $\text{IrO}_2$  phases during strontium leaching produced electrocatalysts that were highly efficient and robust toward the OER.<sup>288</sup>

**4.1.2. Ternary and quaternary alloy phases for increased activity and stability.** Multimetallic alloys which have mainly been studied for their potential synergistic effects, can be obtained *via* the co-reduction of several metal precursors or the post-synthetic modification of bimetallic nanoparticles. Interestingly, these ternary and quaternary alloy phases can show drastically different electrocatalytic activities and stabilities compared to single component or binary alloy nanoparticles. Zhang *et al.* reported that octahedral  $\text{Pt}_2\text{CuNi}$  ternary nanocrystals retained 81.3% and 68.1% of their initial mass activity after 4000 and 10 000 cycles, respectively, while PtNi octahedral nanocrystals retained only 52.9% and 35.0% of their initial mass activity (Fig. 14d).<sup>239</sup> They attributed this improved stability to the uniform ternary alloy composition inhibiting the leaching of Ni and Cu. Saleem and Ud Din *et al.* demonstrated that tetrametallic  $\text{PtPdRhAg}$  nanoframes and porous  $\text{PtCuBiMn}$  nanosheets show highly durable and active electrocatalytic performance toward the FAOR/MOR and ORR (Fig. 14e).<sup>234,325</sup> They suggested that the leaching or dealloying process was passivated due to the unique tetrametallic compositions of the nanoframes. Furthermore, in the case of the  $\text{PtCuBiMn}$  nanosheets, the introduction of the metal Bi improved the methanol tolerance of the catalyst, which showed only a 3.8% loss of mass activity at 0.9 V after 10 000 cycles. These results suggest the great potential of ternary and quaternary alloy nanoframeworks as robust electrocatalysts.

Despite a few successful demonstrations of multicomponent alloys as robust electrocatalysts, theoretical predictions of alloy phase stability and catalytic activity are currently lacking. Also, rational synthetic routes to multicomponent alloy nanoparticles are seriously underdeveloped due to the complexity and difficulty in achieving the desired composition distributions within a single nanoparticle. Therefore, further study of

the theoretical prediction of alloy phase stability and catalytic activity, as well as the development of rational synthetic routes to tailored multicomponent alloy nanostructures, is required.

## 4.2. Structurally-fortified nanocrystals

Well-defined three-dimensional nanoparticle structures show distinct structural features such as corners, edges, and facets, but they are prone to degrade under harsh conditions. The preservation of the structural integrity of catalytically active surface structures has been attempted by (1) the fortification of the most inherently vulnerable sites, namely the vertices, *via* alloying or heterostructure formation and (2) the insertion of supporting material into the nanoframework to maintain the overall high surface area of the structure without seriously sacrificing the exposed surface area on the extremities of the nanostructure.<sup>36–38,226,298</sup>

**4.2.1. Structurally fortified nanoframes.** Due to their very high surface energies, the vertices of a nanoframe are vulnerable to structural degradation during the chemical etching process or electrocycling tests, which are important steps in the formation of nanoframe structures. Several groups have reported synthetic methodologies to reduce the vulnerability of the vertices by growing additional metals on the active vertices, which results in either heteronanostructure formation at the vertices or alloying of the vertices.<sup>36,226</sup> In 2014, Wu *et al.* grew Au islands on the vertices of a Pt–Ni nanoframework through a galvanic replacement reaction (Fig. 15a).<sup>226</sup> The overgrown Au sites impeded the structural deformation of the Pt–Ni nanoframes during the MOR, and the catalytic activity of  $\text{Pt}_3\text{Ni}$  nanoframes with 10% Au remained unchanged after 3000 cycles. Kwon *et al.* reported that Co doping at the vertices of a PtCu nanoframe to form a PtCuCo alloy phase enhanced the structural robustness of the catalyst toward the ORR and MOR during the electrocycling test (Fig. 15b).<sup>36</sup>

**4.2.2. Insertion of structural support into the nanoframework.** Oh *et al.* reported the synthesis of an octahedral PtNi nanoframe with inner-residing three mutually perpendicular Pt-rich axes.<sup>37</sup> The skeletal nanoframeworks were obtained by carbon monoxide (CO) induced phase segregation within *in situ* formed facet-controlled octahedral  $\text{Pt}@\text{Ni}$  core–shell nanoparticles. Due to the geometrically highly symmetric phase-segregated PtNi nanostructure, the inner Pt phase underwent further diffusion to form three intersecting perpendicular Pt axes, driven by the difference in the surface binding strength between Pt–CO and Ni–CO. Ultimately, the inner Pt-rich axes supported the outer nanoframe, enhancing the stability of the catalyst toward the ORR reaction. By adopting a similar concept, Park *et al.* synthesized radially phase segregated  $\text{PtCu}@\text{PtCuNi}$  dendrite@frame nanocatalysts *via* the co-decomposition of three kinds of precursors (Fig. 15c).<sup>38</sup> The diffusion of Pt atoms through the Ni matrix to the outer active sites of the initially formed seeds facilitated reduction of residual Cu precursor on the Pt-rich edges, resulting in the formation of a PtCuNi nanoframe on the Ni matrix. The highly active and durable PtCuNi ternary alloy phase was supported by the inner-lying PtCu dendrite, and the  $\text{PtCu}@\text{PtCuNi}$

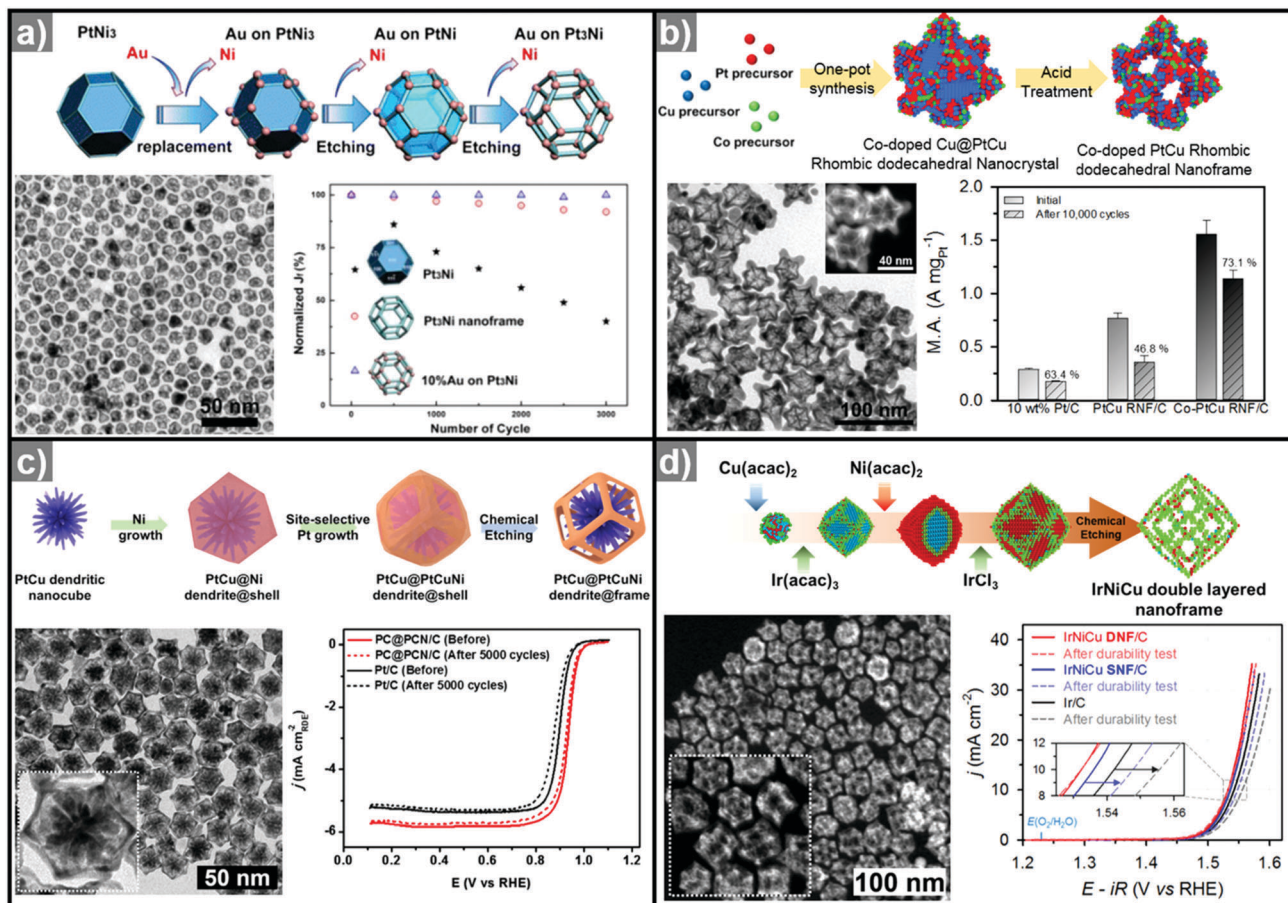


Fig. 15 Schematic illustration of synthetic routes to structurally-fortified nanoparticles and their electrocatalytic performance. (a) TEM image and loss of peak current density of Au islands on Pt–Ni nanoframe dependent on the number of cycling test toward MOR. Reproduced with permission from ref. 226. Copyright 2014 American Chemical Society. (b) TEM image of Co-doped PtCu nanoframe (inset: STEM image) and its electrocatalytic stability compared to PtCu and commercial Pt/C after 10 000 cycles toward ORR. Reproduced with permission from ref. 36. Copyright 2018 Wiley–VCH. (c) TEM image of PtCuNi@PtCu (PC@PCN) dendrite@frame and ORR polarization curves of PC@PCN and commercial Pt/C before and after the cycling test for 5000 cycles. Reproduced with permission from ref. 38. Copyright 2017 American Chemical Society. (d) TEM image of IrNiCu double layered nanoframe and OER polarization curves of IrNiCu double layered nanoframe and single layered nanoframe before and after durability test of 2500 potential cycles. Reproduced with permission from ref. 298. Copyright 2017 American Chemical Society.

dendrite@frame nanostructures exhibited excellent catalytic activity and stability toward the ORR. Park *et al.* also developed Ir-based multimetallic double layered nanoframes by leveraging the different kinetics of Ir precursors of  $\text{Ir}(\text{acac})_3$  and  $\text{IrCl}_3$  and dual transition metal templates consisting of Ni and Cu (Fig. 15d).<sup>298</sup> A core–shell type nanoframe@nanoframe structure was generated in a simple one-step synthesis and was subsequently transformed into a ternary IrNiCu frame@frame nanostructure. Although the Ir and  $\text{IrO}_2$  phases had different unit cell structures, the latter being formed during the oxidative electro-cycling test, it was demonstrated that the inner-lying nanoframe could support the outer-framework morphology even after the OER stability test.<sup>298</sup>

## 5. Outlook

Thus far, a number of hollow nanostructures with novel compositions have demonstrated superb electrocatalytic activities

toward the ORR, HER, and OER, benefitting from the increased number of active sites provided by the inherently high surface area structure. Accordingly, the number of hollow nanocatalysts is increasing rapidly due to the intense synthetic efforts and resulting accumulation of synthetic knowledge for this unique class of materials. However, rational synthetic routes to these nanostructures are still underdeveloped, and the true origins of catalytic the activity and stability of multi-component materials are not well understood. Therefore, in order to facilitate the development of hollow nanostructure-based catalysts for energy applications, the following points must be addressed.

### 5.1. Enhancing the intrinsic catalytic activity of hollow nanostructures by modulating the energy states of the active sites

The open structures of hollow nanostructures provide access to numerous active sites and remarkably enhance electrocatalytic

performance. While this strategy for increasing the number of active sites is undoubtedly beneficial for catalysis, a more important issue in catalyst development is enhancement of the intrinsic activity of catalytically active sites.<sup>288</sup> Recent advances in this area show that it is feasible to modulate the electronic state of the active sites at which the reactants are adsorbed and desorbed, through nanostructural engineering.<sup>151,171,326</sup> For example, the strain on the nanoparticle surface induced by the interface lattice mismatch between the core and the shell can greatly affect the surface energy states.<sup>202,326</sup> The strain can be further modulated by controlling the alloy composition of the core or the thickness of the shell.<sup>242,245,327</sup> Most recently, Bu *et al.* reported the synthesis of biaxially strained PtPb/Pt core/shell nanoplates with enhanced oxygen reduction catalysis performance.<sup>326</sup> They found that the core–shell structural features lead to a large tensile strain that optimizes the Pt–O bond strength, which is crucial for the ORR. In addition, Li *et al.* synthesized ultrafine jagged platinum nanowires with state-of-the-art mass activity at 0.9 V toward the ORR.<sup>223</sup> They suggested that the superior electrocatalytic activity originated from the atomic stress in the nanowires, based on a reactive molecular dynamics study. Considering these examples, the synthesis of hollow nanostructures featuring surface strain is an appealing strategy for the development of active catalysts. Furthermore, studies show that ternary or even quaternary alloy systems can exhibit greatly enhanced catalytic activity and material stability.<sup>234,325,328</sup> Therefore, hollow nanostructures with exotic alloy compositions might usher in the widespread usage of electrochemical water splitting and fuel cell technologies.

## 5.2. Development of theoretical tools to understand the true origin of the catalytic activity of multicomponent hollow nanostructures

Theoretical studies using the optimal simulation models for nanocrystals are crucial for understanding the reaction mechanism, and they should involve the assessment of the surface energy of the exposed nanoparticle or the binding energy between reactant intermediates and the catalyst surface. Armed with this knowledge, it would be feasible to design next generation nanocatalysts with an acceptable level of catalytic activity and stability. Recently, Bacq *et al.* reported the atomic vacancies or defects generating during the surface restructuring of hollow nanostructures are pivotal in determining high electrocatalytic performance of hollow nanostructure after durability test and proved the true origin of the sustained catalytic activity by DFT calculation.<sup>172</sup> However, current studies are mostly confined to facet-controlled bimetallic nanoparticles, and the understanding of the atom arrangements of ternary or quaternary alloy phases during catalysis and their interaction with reaction intermediates is virtually non-existent, due to the difficulties encountered with numerous plausible surface atom configurations. Therefore, the development of methods to greatly simplify the theoretical calculation of complex atomistic arrangements might greatly aid our understanding of the origin of catalytic activity and the development of nanoalloy particles with optimal compositions.

## 5.3. Understanding the dynamics of atomic rearrangement within nanocatalysts during the electrocycling test

As discussed in Section 4, the surface migration of atoms during the electrocycling test might induce enhanced electrocatalytic performance, but it can deteriorate the catalytic stability at the same time. In the case of a few bimetallic alloy systems, it was feasible to identify certain factors affecting the phase segregation phenomena by observing the changes in their atomic arrangement with *ex situ* TEM techniques. Recently, intra-particle atom movements have been followed using *in situ* TEM techniques.<sup>329–332</sup> However, in this case, the condition that led to the real-time atom movement, *i.e.* simple heating, is not relevant to the catalytic setting. Therefore, the development of *in situ* cell designs and the observation of real time atom movements in catalyst nanoparticles during catalysis would greatly elevate the level of our understanding of nanoparticle phase conversion and catalyst stability as well as the origin of catalytic activity.

## 5.4. Considering the actual catalysis operating condition which is to be practically used

The thermodynamically stable alloy phase is a little bit different between during the synthesis and during the electrocatalytic test as already discussed in previous chapter. Until now, some efforts have raised to consider the electrochemical performance measured at high electrochemical potential or elevated temperature, which are similar conditions compared to practical PEMFC application or water electrolyzers. Dubau *et al.* the stability test of hollow nanostructures at elevated temperatures greatly affected the structural degradation of the hollow nanostructure.<sup>150,333,334</sup> The hollow PtNi/C nanoparticles retained their morphologies and compositions during accelerated stress testing at 25 °C, however, the dissolution of Ni atoms was extremely accelerated with increasing the temperature (>80 °C). Although the specific dissolution of the alloying transition metal could be observed, the electrocatalytic performance of hollow PtNi/C nanoparticles toward the ORR still exhibits higher than that of solid PtNi/C nanoparticles. They proposed that the origin of retained electrocatalytic activity is driven from the atomic vacancies contained in the PtNi shell and grain boundaries.<sup>170</sup>

In addition, mass-transport limitations of hollow nanostructures in real membrane electrode assemblies are also critical issue. Snyder, Erlebacher *et al.* discovered that the ECSA of hollow nanostructures could be remarkably different dependent on the range of overpotential.<sup>335</sup> At low overpotential, the oxygen molecules could be diffused into the inner surfaces of hollow nanoparticles, however, they are suppressed to be diffused into the inner surfaces at higher overpotential. Due to this result, we expected that the large surface area of hollow nanostructures might be diminished in actual operating condition. Several recently reported documents proposed that using ionic liquid instead of aqueous solution could offer higher oxygen solubility by filling the inner surface area of hollow nanostructures.<sup>38,143,207,336</sup> This concept also proved the

advantage of hollow structural feature, but it is important to take into account when we used in actual condition. Therefore, profound understanding of dealloying procedure and limitation of mass-transport in the actual condition is recommended in order to make sustainable electrocatalysts.

## 6. Conclusion

As described in this review, the structural advantage of hollow nanostructures as electrocatalysts for the HER, OER, and ORR does not originate only from their inherent high surface area. A detailed understanding of the mechanistic aspects of the catalytic events suggests that facet control and alloy composition control can also greatly improve the chance of widespread societal penetration of these energy conversion technologies. The design concept of hollow nanostructures can evolve further to incorporate ternary or quaternary alloy systems into the nanoframeworks as well as the additional structural features of lattice-mismatched interfaces or twinning. Despite the great potential benefits of multicomponent nanoframe structures as electrocatalysts, we have only recently embarked on the journey of nanoscale alloy formation and phase segregation, and thus our synthetic tools for the fabrication of alloy nanoframes are still primitive. Therefore, there is a huge research potential in the area of multicomponent hollow nanostructures with greater complexity than binary or ternary systems as electrocatalysts. Additionally, examples of hollow nanostructures of many catalytically important metal compounds, such as metal oxides, sulfides, and phosphides, are very rare. Eventually, catalysts should be extremely atom efficient, and the recent development of single atom catalysts is certainly a promising research direction. It is utterly intriguing to envisage hollow nanostructures featuring the novel design concepts of single atom catalysis and nano-features that modify the surface energy, such as lattice-mismatch or twinning. Therefore, it is not difficult to imagine the advent of next generation hollow electrocatalysts incorporating some of these exciting structural features in the near future.

## Conflicts of interest

There are no conflicts to declare.

## Acknowledgements

This work was supported by IBS-R023-D1, NRF-2017R1A2B3005682, and Korea University Future Research Grant. S. H. J. and H. Y. K. were supported by the NRF of Korea (NRF-2017R1A2B2008464).

## References

- 1 H. B. Gray, *Nat. Chem.*, 2009, **1**, 7.
- 2 M. G. Walter, E. L. Warren, J. R. McKone, S. W. Boettcher, Q. Mi, E. A. Santori and N. S. Lewis, *Chem. Rev.*, 2010, **110**, 6446–6473.
- 3 T. R. Cook, D. K. Dogutan, S. Y. Reece, Y. Surendranath, T. S. Teets and D. G. Nocera, *Chem. Rev.*, 2010, **110**, 6474–6502.
- 4 J. Qi, W. Zhang and R. Cao, *Adv. Energy Mater.*, 2018, **8**, 1701620.
- 5 I. E. L. Stephens, J. Rossmeisl and I. Chorkendorff, *Science*, 2016, **354**, 1378–1379.
- 6 Y. Jiao, Y. Zheng, M. Jaroniec and S. Z. Qiao, *Chem. Soc. Rev.*, 2015, **44**, 2060–2086.
- 7 J. H. Montoya, L. C. Seitz, P. Chakthranont, A. Vojvodic, T. F. Jaramillo and J. K. Nørskov, *Nat. Mater.*, 2017, **16**, 70–81.
- 8 S. Anantharaj, S. R. Ede, K. Sakthikumar, K. Karthick, S. Mishra and S. Kundu, *ACS Catal.*, 2016, **6**, 8069–8097.
- 9 T. Reier, H. N. Nong, D. Teschner, R. Schlögl and P. Strasser, *Adv. Energy Mater.*, 2017, **7**, 1601275.
- 10 Y. Xia and X. Yang, *Acc. Chem. Res.*, 2017, **50**, 450–454.
- 11 F. Calle-Vallejo, M. D. Pohl, D. Reinisch, D. Loffreda, P. Sautet and A. S. Bandarenka, *Chem. Sci.*, 2017, **8**, 2283–2289.
- 12 J. K. Nørskov, T. Bligaard, J. Rossmeisl and C. H. Christensen, *Nat. Chem.*, 2009, **1**, 37–46.
- 13 K. S. Exner and H. Over, *Acc. Chem. Res.*, 2017, **50**, 1240–1247.
- 14 M. M. Montemore, M. A. van Spronsen, R. J. Madix and C. M. Friend, *Chem. Rev.*, 2017, **118**, 2816–2862.
- 15 V. R. Stamenkovic, D. Strmenik, P. P. Lopes and N. M. Markovic, *Nat. Mater.*, 2017, **16**, 57–69.
- 16 W. Gao, Z. D. Hood and M. Chi, *Acc. Chem. Res.*, 2017, **50**, 787–795.
- 17 I. E. L. Stephens, A. S. Bondarenko, U. Grønbjerg, J. Rossmeisl and I. Chorkendorff, *Energy Environ. Sci.*, 2012, **5**, 6744.
- 18 V. R. Stamenkovic, B. S. Mun, M. Arenz, K. J. J. Mayrhofer, C. A. Lucas, G. Wang, P. N. Ross and N. M. Markovic, *Nat. Mater.*, 2007, **6**, 241–247.
- 19 J. Greeley and M. Mavrikakis, *Nat. Mater.*, 2004, **3**, 810.
- 20 A. R. Tao, S. Habas and P. Yang, *Small*, 2008, **4**, 310–325.
- 21 M. Chen, B. Wu, J. Yang and N. Zheng, *Adv. Mater.*, 2012, **24**, 862–879.
- 22 M. B. Gawande, A. Goswami, T. Asefa, H. Guo, A. V. Biradar, D.-L. Peng, R. Zboril and R. S. Varma, *Chem. Soc. Rev.*, 2015, **44**, 7540–7590.
- 23 B. T. Sneed, A. P. Young and C.-K. Tsung, *Nanoscale*, 2015, **7**, 12248–12265.
- 24 R. Ghosh Chaudhuri and S. Paria, *Chem. Rev.*, 2012, **112**, 2373–2433.
- 25 R. Schlögl, *Angew. Chem., Int. Ed.*, 2015, **54**, 3465–3520.
- 26 S. Schauermann, N. Nilius, S. Shaikhutdinov and H.-J. Freund, *Acc. Chem. Res.*, 2013, **46**, 1673–1681.
- 27 S. M. S. Kumar, N. Hidayat, J. S. Herrero, S. Irusta and K. Scott, *Int. J. Hydrogen Energy*, 2011, **36**, 5453–5465.
- 28 J. Cho, L. Xu, C. Jo and R. Ryoo, *Chem. Commun.*, 2017, **53**, 3810–3813.
- 29 S. H. Joo, S. J. Choi, I. Oh, J. Kwak, Z. Liu, O. Terasaki and R. Ryoo, *Nature*, 2001, **412**, 169.
- 30 Y. Keereeta, S. Thongtem and T. Thongtem, *Powder Technol.*, 2015, **284**, 85–94.

31 S. S. Park, S.-W. Chu, C. Xue, D. Zhao and C.-S. Ha, *J. Mater. Chem.*, 2011, **21**, 10801–10807.

32 W. Wang, M. Dahl and Y. Yin, *Chem. Mater.*, 2013, **25**, 1179–1189.

33 B. D. Anderson and J. B. Tracy, *Nanoscale*, 2014, **6**, 12195–12216.

34 H. J. Fan, U. Gösele and M. Zacharias, *Small*, 2007, **3**, 1660–1671.

35 V. Beermann, M. Gocyla, E. Willinger, S. Rudi, M. Heggen, R. E. Dunin-Borkowski, M. G. Willinger and P. Strasser, *Nano Lett.*, 2016, **16**, 1719–1725.

36 T. Kwon, M. Jun, H. Y. Kim, A. Oh, J. Park, H. Baik, S. H. Joo and K. Lee, *Adv. Funct. Mater.*, 2018, **28**, 1706440.

37 A. Oh, H. Baik, D. S. Choi, J. Y. Cheon, B. Kim, H. Kim, S. J. Kwon, S. H. Joo, Y. Jung and K. Lee, *ACS Nano*, 2015, **9**, 2856–2867.

38 J. Park, M. Kanti Kabiraz, H. Kwon, S. Park, H. Baik, S.-I. Choi and K. Lee, *ACS Nano*, 2017, **11**, 10844–10851.

39 K. Lee, M. Kim and H. Kim, *J. Mater. Chem.*, 2010, **20**, 3791–3798.

40 B. Lim, J. Wang, P. H. Camargo, M. Jiang, M. J. Kim and Y. Xia, *Nano Lett.*, 2008, **8**, 2535–2540.

41 B. Lim, M. Jiang, P. H. Camargo, E. C. Cho, J. Tao, X. Lu, Y. Zhu and Y. Xia, *Science*, 2009, **324**, 1302–1305.

42 F. R. Fan, D. Y. Liu, Y. F. Wu, S. Duan, Z. X. Xie, Z. Y. Jiang and Z. Q. Tian, *J. Am. Chem. Soc.*, 2008, **130**, 6949–6951.

43 T. Kim, J. Park, H. Jin, A. Oh, H. Baik, S. H. Joo and K. Lee, *Nanoscale*, 2018, **10**, 9845–9850.

44 M. Zhao, L. Figueroa-Cosme, A. O. Elnabawy, M. Vara, X. Yang, L. T. Roling, M. Chi, M. Mavrikakis and Y. Xia, *Nano Lett.*, 2016, **16**, 5310–5317.

45 M. Zhao, A. O. Elnabawy, M. Vara, L. Xu, Z. D. Hood, X. Yang, K. D. Gilroy, L. Figueroa-Cosme, M. Chi, M. Mavrikakis and Y. Xia, *Chem. Mater.*, 2017, **29**, 9227–9237.

46 S. Xie, N. Lu, Z. Xie, J. Wang, M. J. Kim and Y. Xia, *Angew. Chem., Int. Ed.*, 2012, **51**, 10266–10270.

47 B. T. Sneed, C. N. Brodsky, C. H. Kuo, L. K. Lamontagne, Y. Jiang, Y. Wang, F. F. Tao, W. Huang and C. K. Tsung, *J. Am. Chem. Soc.*, 2013, **135**, 14691–14700.

48 W. Ye, S. Kou, X. Guo, F. Xie, H. Sun, H. Lu and J. Yang, *Nanoscale*, 2015, **7**, 9558–9562.

49 N. Fan, Y. Yang, W. Wang, L. Zhang, W. Chen, C. Zou and S. Huang, *ACS Nano*, 2012, **6**, 4072–4082.

50 L. Zhang, L. T. Roling, X. Wang, M. Vara, M. Chi, J. Liu, S. I. Choi, J. Park, J. A. Herron, Z. Xie, M. Mavrikakis and Y. Xia, *Science*, 2015, **349**, 412–416.

51 X. Wang, L. Figueroa-Cosme, X. Yang, M. Luo, J. Liu, Z. Xie and Y. Xia, *Nano Lett.*, 2016, **16**, 1467–1471.

52 J. Park, H. Wang, M. Vara and Y. Xia, *ChemSusChem*, 2016, **9**, 2855–2861.

53 H. Ye, Q. Wang, M. Catalano, N. Lu, J. Vermeylen, M. J. Kim, Y. Liu, Y. Sun and X. Xia, *Nano Lett.*, 2016, **16**, 2812–2817.

54 D. S. He, D. He, J. Wang, Y. Lin, P. Yin, X. Hong, Y. Wu and Y. Li, *J. Am. Chem. Soc.*, 2016, **138**, 1494–1497.

55 S. Bang, D. Yoon, J. Kim, H. Baik, H. Yang and K. Lee, *CrystEngComm*, 2015, **17**, 4084–4088.

56 H. Jin, K. W. Lee, N. T. Khi, H. An, J. Park, H. Baik, J. Kim, H. Yang and K. Lee, *Small*, 2015, **11**, 4462–4468.

57 L. Yu, H. Hu, H. B. Wu and X. W. D. Lou, *Adv. Mater.*, 2017, **29**, 1604563.

58 X. Lai, J. Li, B. A. Korgel, Z. Dong, Z. Li, F. Su, J. Du and D. Wang, *Angew. Chem., Int. Ed.*, 2011, **50**, 2738–2741.

59 X. Lai, J. E. Halpert and D. Wang, *Energy Environ. Sci.*, 2012, **5**, 5604–5618.

60 J. Wang, N. Yang, H. Tang, Z. Dong, Q. Jin, M. Yang, D. Kisailus, H. Zhao, Z. Tang and D. Wang, *Angew. Chem., Int. Ed.*, 2013, **52**, 6417–6420.

61 G. Zhang and X. W. D. Lou, *Angew. Chem., Int. Ed.*, 2014, **53**, 9041–9044.

62 Y. Guo, L. Yu, C.-Y. Wang, Z. Lin and X. W. D. Lou, *Adv. Funct. Mater.*, 2015, **25**, 5184–5189.

63 P. M. Arnal, M. Comotti and F. Schüth, *Angew. Chem., Int. Ed.*, 2006, **45**, 8224–8227.

64 X. W. Lou, C. M. Li and L. A. Archer, *Adv. Mater.*, 2009, **21**, 2536–2539.

65 R. Jin, Y. Yang, Y. Xing, L. Chen, S. Song and R. Jin, *ACS Nano*, 2014, **8**, 3664–3670.

66 X. W. Lou, C. Yuan and L. A. Archer, *Adv. Mater.*, 2007, **19**, 3328–3332.

67 X. W. Lou and L. A. Archer, *Adv. Mater.*, 2008, **20**, 1853–1858.

68 Z. Wang, D. Luan, F. Y. Boey and X. W. Lou, *J. Am. Chem. Soc.*, 2011, **133**, 4738–4741.

69 Z. Wang and X. W. D. Lou, *Adv. Mater.*, 2012, **24**, 4124–4129.

70 H. Hu, L. Yu, X. Gao, Z. Lin and X. W. Lou, *Energy Environ. Sci.*, 2015, **8**, 1480–1483.

71 L. Zhang, T. Liu, K. Liu, L. Han, Y. Yin and C. Gao, *Nano Lett.*, 2015, **15**, 4448–4454.

72 B. Y. Guan, L. Yu, J. Li and X. W. Lou, *Sci. Adv.*, 2016, **2**, e1501554.

73 H. J. Fan, M. Knez, R. Scholz, D. Hesse, K. Nielsch, M. Zacharias and U. Gösele, *Nano Lett.*, 2007, **7**, 993–997.

74 Y. Yin, R. M. Rioux, C. K. Erdonmez, S. Hughes, G. A. Somorjai and A. P. Alivisatos, *Science*, 2004, **304**, 711–714.

75 Y. Yin, C. K. Erdonmez, A. Cabot, S. Hughes and A. P. Alivisatos, *Adv. Funct. Mater.*, 2006, **16**, 1389–1399.

76 A. Cabot, V. F. Puntes, E. Shevchenko, Y. Yin, L. Balcells, M. A. Marcus, S. M. Hughes and A. P. Alivisatos, *J. Am. Chem. Soc.*, 2007, **129**, 10358–10360.

77 S. Peng and S. Sun, *Angew. Chem., Int. Ed.*, 2007, **46**, 4155–4158.

78 R.-K. Chiang and R.-T. Chiang, *Inorg. Chem.*, 2007, **46**, 369–371.

79 J. Park, H. Zheng, Y. W. Jun and A. P. Alivisatos, *J. Am. Chem. Soc.*, 2009, **131**, 13943–13945.

80 C.-H. Kuo, Y.-T. Chu, Y.-F. Song and M. H. Huang, *Adv. Funct. Mater.*, 2011, **21**, 792–797.

81 J. Kim, H. Jin, A. Oh, H. Baik, S. H. Joo and K. Lee, *Nanoscale*, 2017, **9**, 15397–15406.

82 S. G. Bratsch, *J. Phys. Chem. Ref. Data*, 1989, **18**, 1–21.

83 Y. G. Sun, B. T. Mayers and Y. N. Xia, *Nano Lett.*, 2002, **2**, 481–485.

84 Y. Sun and Y. Xia, *Science*, 2002, **298**, 2176–2179.

85 X. Sun, J. Kim, K. D. Gilroy, J. Liu, T. A. F. König and D. Qin, *ACS Nano*, 2016, **10**, 8019–8025.

86 Y. Choi, S. Hong, L. Liu, S. K. Kim and S. Park, *Langmuir*, 2012, **28**, 6670–6676.

87 J. Chen, B. Wiley, Z. Y. Li, D. Campbell, F. Saeki, H. Cang, L. Au, J. Lee, X. Li and Y. Xia, *Adv. Mater.*, 2005, **17**, 2255–2261.

88 X. Lu, L. Au, J. McLellan, Z. Y. Li, M. Marquez and Y. Xia, *Nano Lett.*, 2007, **7**, 1764–1769.

89 Y. Sun and Y. Xia, *J. Am. Chem. Soc.*, 2004, **126**, 3892–3901.

90 L. Vitos, A. V. Ruban, H. L. Skriver and J. Kollar, *Surf. Sci.*, 1998, **411**, 186–202.

91 C. M. Cobley and Y. Xia, *Mater. Sci. Eng., R*, 2010, **70**, 44–62.

92 X. Xia, Y. Wang, A. Ruditskiy and Y. Xia, *Adv. Mater.*, 2013, **25**, 6313–6333.

93 E. González, J. Arbiol and V. F. Puntes, *Science*, 2011, **334**, 1377–1380.

94 J. W. Hong, S. W. Kang, B.-S. Choi, D. Kim, S. B. Lee and S. W. Han, *ACS Nano*, 2012, **6**, 2410–2419.

95 M. Liu, Y. Zheng, S. Xie, N. Li, N. Lu, J. Wang, M. J. Kim, L. Guo and Y. Xia, *Phys. Chem. Chem. Phys.*, 2013, **15**, 11822.

96 S. Xie, M. Jin, J. Tao, Y. Wang, Z. Xie, Y. Zhu and Y. Xia, *Chem. – Eur. J.*, 2012, **18**, 14974–14980.

97 L. Han, P. Wang, H. Liu, Q. Tan and J. Yang, *J. Mater. Chem. A*, 2016, **4**, 18354–18365.

98 M. H. Oh, T. Yu, S. H. Yu, B. Lim, K. T. Ko, M. G. Willinger, D. H. Seo, B. H. Kim, M. G. Cho, J. H. Park, K. Kang, Y. E. Sung, N. Pinna and T. Hyeon, *Science*, 2013, **340**, 964–968.

99 M. D. Susman, R. Popovitz-Biro, A. Vaskevich and I. Rubinstein, *Small*, 2015, **11**, 3942–3953.

100 A. López-Ortega, A. G. Roca, P. Torruella, M. Petrecca, S. Estradé, F. Peiró, V. Puntes and J. Nogués, *Chem. Mater.*, 2016, **28**, 8025–8031.

101 D. Yoon, S. Bang, J. Park, J. Kim, H. Baik, H. Yang and K. Lee, *CrystEngComm*, 2015, **17**, 6843–6847.

102 Z. Niu, N. Becknell, Y. Yu, D. Kim, C. Chen, N. Kornienko, G. A. Somorjai and P. Yang, *Nat. Mater.*, 2016, **15**, 1188–1194.

103 D. Yoon, S. Park, J. Park, J. Kim, H. Baik, H. Yang and K. Lee, *Nanoscale*, 2014, **6**, 12397–12402.

104 J. Park, J. Kim, Y. Yang, D. Yoon, H. Baik, S. Haam, H. Yang and K. Lee, *Adv. Sci.*, 2016, **3**, 1500252.

105 H. Kobayashi, K. Kusada and H. Kitagawa, *Acc. Chem. Res.*, 2015, **48**, 1551–1559.

106 G. Bruni, *Chem. Rev.*, 1925, **1**, 345–375.

107 B. Huang, H. Kobayashi, T. Yamamoto, S. Matsumura, Y. Nishida, K. Sato, K. Nagaoka, S. Kawaguchi, Y. Kubota and H. Kitagawa, *J. Am. Chem. Soc.*, 2017, **139**, 4643–4646.

108 Z. Swiatkowska-Warkocka, A. Pyatenko, F. Krok, B. R. Jany and M. Marszalek, *Sci. Rep.*, 2015, **5**, 9849.

109 K. Kusada, H. Kobayashi, R. Ikeda, Y. Kubota, M. Takata, S. Toh, T. Yamamoto, S. Matsumura, N. Sumi, K. Sato, K. Nagaoka and H. Kitagawa, *J. Am. Chem. Soc.*, 2014, **136**, 1864–1871.

110 D. Srikanth, A. Gargi, K. Sanket Ranjan, K. Sanjeet and C. Abhijit, *Modell. Simul. Mater. Sci. Eng.*, 2017, **25**, 085011.

111 M. Cui, H. Lu, H. Jiang, Z. Cao and X. Meng, *Sci. Rep.*, 2017, **7**, 41990.

112 L. L. Wang and D. D. Johnson, *J. Am. Chem. Soc.*, 2009, **131**, 14023–14029.

113 S. Xiong, W. Qi, B. Huang and M. Wang, *ChemPhysChem*, 2011, **12**, 1317–1324.

114 W. H. Qi, B. Y. Huang and M. P. Wang, *Phys. B*, 2009, **404**, 1761–1765.

115 W. H. Qi, M. P. Wang and Q. H. Liu, *J. Mater. Sci.*, 2005, **40**, 2737–2739.

116 A. Christensen, P. Stoltze and J. K. Norskov, *J. Phys.: Condens. Matter*, 1995, **7**, 1047.

117 G. Guisbiers, S. Khanal, F. Ruiz-Zepeda, J. Roque de la Puente and M. Jose-Yacaman, *Nanoscale*, 2014, **6**, 14630–14635.

118 M. Cui, H. Lu, H. Jiang, Z. Cao and X. Meng, *Sci. Rep.*, 2017, **7**, 41990.

119 G. Guisbiers, R. Mendoza-Pérez, L. Bazán-Díaz, R. Mendoza-Cruz, J. J. Velázquez-Salazar and M. José-Yacamán, *J. Phys. Chem. C*, 2017, **121**, 6930–6939.

120 H. Liao, A. Fisher and Z. J. Xu, *Small*, 2015, **11**, 3221–3246.

121 R. Ferrando, J. Jellinek and R. L. Johnston, *Chem. Rev.*, 2008, **108**, 845–910.

122 A. Zaleska-Medynska, M. Marchelek, M. Diak and E. Grabowska, *Adv. Colloid Interface Sci.*, 2016, **229**, 80–107.

123 B.-J. Hwang, L. S. Sarma, J.-M. Chen, C.-H. Chen, S.-C. Shih, G.-R. Wang, D.-G. Liu, J.-F. Lee and M.-T. Tang, *J. Am. Chem. Soc.*, 2005, **127**, 11140–11145.

124 N. Becknell, C. D. Zheng, C. Chen and P. D. Yang, *Surf. Sci.*, 2016, **648**, 328–332.

125 A. Oh, Y. J. Sa, H. Hwang, H. Baik, J. Kim, B. Kim, S. H. Joo and K. Lee, *Nanoscale*, 2016, **8**, 16379–16386.

126 F. Calvo, *Phys. Chem. Chem. Phys.*, 2015, **17**, 27922–27939.

127 J. Suntivich, Z. Xu, C. E. Carlton, J. Kim, B. Han, S. W. Lee, N. Bonnet, N. Marzari, L. F. Allard, H. A. Gasteiger, K. Hamad-Schifferli and Y. Shao-Horn, *J. Am. Chem. Soc.*, 2013, **135**, 7985–7991.

128 S.-Y. Lee, N. Jung, J. Cho, H.-Y. Park, J. Ryu, I. Jang, H.-J. Kim, E. Cho, Y.-H. Park, H. C. Ham, J. H. Jang and S. J. Yoo, *ACS Catal.*, 2014, **4**, 2402–2408.

129 K. J. Andersson, F. Calle-Vallejo, J. Rossmeisl and I. Chorkendorff, *J. Am. Chem. Soc.*, 2009, **131**, 2404–2407.

130 K. J. J. Mayrhofer, V. Juhart, K. Hartl, M. Hanzlik and M. Arenz, *Angew. Chem., Int. Ed.*, 2009, **48**, 3529–3531.

131 G. E. Ramírez-Caballero, Y. Ma, R. Callejas-Tovar and P. B. Balbuena, *Phys. Chem. Chem. Phys.*, 2010, **12**, 2209.

132 R. Mu, X. Guo, Q. Fu and X. Bao, *J. Phys. Chem. C*, 2011, **115**, 20590–20595.

133 F. Tao, M. E. Grass, Y. Zhang, D. R. Butcher, J. R. Renzas, Z. Liu, J. Y. Chung, B. S. Mun, M. Salmeron and G. A. Somorjai, *Science*, 2008, **322**, 932–934.

134 A. J. Logsdail, L. O. Paz-Borbon and C. A. Downing, *J. Phys. Chem. C*, 2018, **122**, 5721–5730.

135 A. Lopes, G. Tréglia, C. Mottet and B. Legrand, *Phys. Rev. B: Condens. Matter Mater. Phys.*, 2015, **91**, 035407.

136 W. Niu, L. Zhang and G. Xu, *ACS Nano*, 2010, **4**, 1987–1996.

137 X. He, S.-E. Zhang, F. Cheng and Z.-X. Chen, *Chem. Commun.*, 2018, **54**, 638–641.

138 Y. G. Chen, Z. J. Yu, Z. Chen, R. A. Shen, Y. Wang, X. Cao, Q. Peng and Y. D. Li, *Nano Res.*, 2016, **9**, 2632–2640.

139 C. Li, K. Eid, H. J. Wang, Y. Y. Deng, S. L. Lu, X. N. Li, L. Wang and H. W. Gu, *New J. Chem.*, 2018, **42**, 798–801.

140 F. Nosheen, Z. C. Zhang, J. Zhuang and X. Wang, *Nanoscale*, 2013, **5**, 3660–3663.

141 J. Pei, J. Mao, X. Liang, C. Chen, Q. Peng, D. Wang and Y. Li, *Chem. Commun.*, 2016, **52**, 3793–3796.

142 J. Ding, L. Bu, S. Guo, Z. Zhao, E. Zhu, Y. Huang and X. Huang, *Nano Lett.*, 2016, **16**, 2762–2767.

143 C. Chen, Y. Kang, Z. Huo, Z. Zhu, W. Huang, H. L. Xin, J. D. Snyder, D. Li, J. A. Herron, M. Mavrikakis, M. Chi, K. L. More, Y. Li, N. M. Markovic, G. A. Somorjai, P. Yang and V. R. Stamenkovic, *Science*, 2014, **343**, 1339–1343.

144 C. Wang, L. Zhang, H. Yang, J. Pan, J. Liu, C. Dotse, Y. Luan, R. Gao, C. Lin, J. Zhang, J. P. Kilcrease, X. Wen, S. Zou and J. Fang, *Nano Lett.*, 2017, **17**, 2204–2210.

145 H. Hwang, T. Kwon, H. Y. Kim, J. Park, A. Oh, B. Kim, H. Baik, S. H. Joo and K. Lee, *Small*, 2018, **14**, 1702353.

146 G. Chen, S. Desinan, R. Rosei, F. Rosei and D. Ma, *Chem. Commun.*, 2012, **48**, 8009.

147 S. J. Bae, S. J. Yoo, Y. Lim, S. Kim, Y. Lim, J. Choi, K. S. Nahm, S. J. Hwang, T.-H. Lim, S.-K. Kim and P. Kim, *J. Mater. Chem.*, 2012, **22**, 8820–8825.

148 H. Bönnemann, G. Braun, W. Brijoux, R. Brinkmann, A. S. Tilling, K. Seevogel and K. Siepen, *J. Organomet. Chem.*, 1996, **520**, 143–162.

149 B. Helmut, B. Werner, B. Rainer, J. Thomas, K. Barbara and D. Eckard, *Angew. Chem., Int. Ed. Engl.*, 1991, **30**, 1312–1314.

150 T. Asset, R. Chattot, M. Fontana, B. Mercier-Guyon, N. Job, L. Dubau and F. Maillard, *ChemPhysChem*, 2018, **19**, 1552–1567.

151 J. X. Wang, C. Ma, Y. Choi, D. Su, Y. Zhu, P. Liu, R. Si, M. B. Vukmirovic, Y. Zhang and R. R. Adzic, *J. Am. Chem. Soc.*, 2011, **133**, 13551–13557.

152 L. Dubau, M. Lopez-Haro, J. Durst, L. Guetaz, P. Bayle-Guillemaud, M. Chatenet and F. Maillard, *J. Mater. Chem. A*, 2014, **2**, 18497–18507.

153 L. Dubau, T. Asset, R. Chattot, C. Bonnaud, V. Vanpeene, J. Nelayah and F. Maillard, *ACS Catal.*, 2015, **5**, 5333–5341.

154 R. Chattot, T. Asset, J. Drnec, P. Bordet, J. Nelayah, L. Dubau and F. Maillard, *Nano Lett.*, 2017, **17**, 2447–2453.

155 T. Asset, R. Chattot, J. Drnec, P. Bordet, N. Job, F. Maillard and L. Dubau, *ACS Appl. Mater. Interfaces*, 2017, **9**, 25298–25307.

156 L. Han-Pu, Z. Hui-Min, H. Jin-Song, G. Yu-Guo, W. Li-Jun and B. Chun-Li, *Angew. Chem., Int. Ed.*, 2004, **43**, 1540–1543.

157 L. Dubau, J. Durst, F. Maillard, L. Guétaz, M. Chatenet, J. André and E. Rossinot, *Electrochim. Acta*, 2011, **56**, 10658–10667.

158 M. Lopez-Haro, L. Dubau, L. Guétaz, P. Bayle-Guillemaud, M. Chatenet, J. André, N. Caqué, E. Rossinot and F. Maillard, *Appl. Catal., B*, 2014, **152–153**, 300–308.

159 M. K. Debe, *Nature*, 2012, **486**, 43–51.

160 M. Shao, Q. Chang, J.-P. Dodelet and R. Chenitz, *Chem. Rev.*, 2016, **116**, 3594–3657.

161 M. Carmo, D. L. Fritz, J. Merge and D. Stolten, *Int. J. Hydrogen Energy*, 2013, **38**, 4901–4934.

162 N. S. Lewis, *Science*, 2016, **351**, aad1920.

163 F. Gutierrez-Martin and I. Guerrero-Hernandez, *Int. J. Hydrogen Energy*, 2012, **37**, 1151–1161.

164 K. Zeng and D. K. Zhang, *Prog. Energy Combust. Sci.*, 2010, **36**, 307–326.

165 P. C. K. Vesborg, B. Seger and I. Chorkendorff, *J. Phys. Chem. Lett.*, 2015, **6**, 951–957.

166 Z. W. Seh, J. Kibsgaard, C. F. Dickens, I. Chorkendorff, J. K. Nørskov and T. F. Jaramillo, *Science*, 2017, **355**, eaad4998.

167 F. Calle-Vallejo, J. Tymoczko, V. Colic, Q. H. Vu, M. D. Pohl, K. Morgenstern, D. Loffreda, P. Sautet, W. Schuhmann and A. S. Bandarenka, *Science*, 2015, **350**, 185–189.

168 A. Tristan, C. Raphaël, N. Jaysen, J. Nathalie, D. Laetitia and M. Frédéric, *ChemElectroChem*, 2016, **3**, 1591–1600.

169 T. Asset, N. Job, Y. Busby, A. Crisci, V. Martin, V. Stergiopoulos, C. Bonnaud, A. Serov, P. Atanassov, R. Chattot, L. Dubau and F. Maillard, *ACS Catal.*, 2018, **8**, 893–903.

170 L. Dubau, J. Nelayah, S. Moldovan, O. Ersen, P. Bordet, J. Drnec, T. Asset, R. Chattot and F. Maillard, *ACS Catal.*, 2016, **6**, 4673–4684.

171 R. Chattot, T. Asset, P. Bordet, J. Drnec, L. Dubau and F. Maillard, *ACS Catal.*, 2017, **7**, 398–408.

172 L. B. Olivier, P. Alain, C. Raphaël, P. Bruno, N. Jaysen, A. Tristan, D. Laetitia and M. Frédéric, *ChemCatChem*, 2017, **9**, 2324–2338.

173 W. Wang, B. Lei and S. Guo, *Adv. Energy Mater.*, 2016, **6**, 1600236.

174 M. C. Luo and S. J. Guo, *Nat. Rev. Mater.*, 2017, **2**, 17059.

175 S. Sui, X. Y. Wang, X. T. Zhou, Y. H. Su, S. Riffat and C. J. Liu, *J. Mater. Chem. A*, 2017, **5**, 1808–1825.

176 N. M. Markovic, R. R. Adzic, B. D. Cahan and E. B. Yeager, *J. Electroanal. Chem.*, 1994, **377**, 249–259.

177 N. M. Markovic, T. J. Schmidt, V. Stamenkovic and P. N. Ross, *Fuel Cells*, 2001, **1**, 105–116.

178 V. R. Stamenkovic, B. Fowler, B. S. Mun, G. Wang, P. N. Ross, C. A. Lucas and N. M. Markovic, *Science*, 2007, **315**, 493–497.

179 N. Hoshi, M. Nakamura and A. Hitotsuyanagi, *Electrochim. Acta*, 2013, **112**, 899–904.

180 Z. Quan, Y. Wang and J. Fang, *Acc. Chem. Res.*, 2012, **46**, 191–202.

181 B. Y. Xia, H. B. Wu, X. Wang and X. W. D. Lou, *Angew. Chem., Int. Ed.*, 2013, **52**, 12337–12340.

182 J. Wu and H. Yang, *Acc. Chem. Res.*, 2013, **46**, 1848–1857.

183 T. Sheng, N. Tian, Z.-Y. Zhou, W.-F. Lin and S.-G. Sun, *ACS Energy Lett.*, 2017, **2**, 1892–1900.

184 X. Xu, X. Zhang, H. Sun, Y. Yang, X. Dai, J. Gao, X. Li, P. Zhang, H. H. Wang, N. F. Yu and S. G. Sun, *Angew. Chem., Int. Ed.*, 2014, **53**, 12522–12527.

185 X. Huang, Z. Zhao, J. Fan, Y. Tan and N. Zheng, *J. Am. Chem. Soc.*, 2011, **133**, 4718–4721.

186 Q. Chen, Y. Jia, S. Xie and Z. Xie, *Chem. Soc. Rev.*, 2016, **45**, 3207–3220.

187 Y. Jia, Y. Jiang, J. Zhang, L. Zhang, Q. Chen, Z. Xie and L. Zheng, *J. Am. Chem. Soc.*, 2014, **136**, 3748–3751.

188 Q. Chen, Z. Cao, G. Du, Q. Kuang, J. Huang, Z. Xie and L. Zheng, *Nano Energy*, 2017, **39**, 582–589.

189 J. Zhang, Q. Kuang, Y. Jiang and Z. Xie, *Nano Today*, 2016, **11**, 661–677.

190 T. Yu, Y. Kim, H. Zhang and Y. Xia, *Angew. Chem.*, 2011, **123**, 2825–2829.

191 T. Toda, H. Igarashi, H. Uchida and M. Watanabe, *J. Electrochem. Soc.*, 1999, **146**, 3750–3756.

192 J. Greeley, I. E. L. Stephens, A. S. Bondarenko, T. P. Johansson, H. A. Hansen, T. F. Jaramillo, J. Rossmeisl, I. Chorkendorff and J. K. Nørskov, *Nat. Chem.*, 2009, **1**, 552–556.

193 V. Čolić and A. S. Bandarenka, *ACS Catal.*, 2016, **6**, 5378–5385.

194 Y. Bing, H. Liu, L. Zhang, D. Ghosh and J. Zhang, *Chem. Soc. Rev.*, 2010, **39**, 2184.

195 V. R. Stamenkovic, B. S. Mun, M. Arenz, K. J. J. Mayrhofer, C. A. Lucas, G. Wang, P. N. Ross and N. M. Markovic, *Nat. Mater.*, 2007, **6**, 241.

196 E. Toyoda, R. Jinnouchi, T. Hatanaka, Y. Morimoto, K. Mitsuhashi, A. Visikovskiy and Y. Kido, *J. Phys. Chem. C*, 2011, **115**, 21236–21240.

197 V. Viswanathan, H. A. Hansen, J. Rossmeisl and J. K. Nørskov, *ACS Catal.*, 2012, **2**, 1654–1660.

198 H. F. Lv, D. G. Li, D. Strmenik, A. P. Paulikas, N. M. Markovic and V. R. Stamenkovic, *Nano Energy*, 2016, **29**, 149–165.

199 F. H. B. Lima, J. Zhang, M. H. Shao, K. Sasaki, M. B. Vukmirovic, E. A. Ticianelli and R. R. Adzic, *J. Phys. Chem. C*, 2007, **111**, 404–410.

200 P. Strasser and S. Kuhl, *Nano Energy*, 2016, **29**, 166–177.

201 L. Gan, C. Cui, M. Heggen, F. Dionigi, S. Rudi and P. Strasser, *Science*, 2014, **346**, 1502–1506.

202 P. Strasser, S. Koh, T. Anniyev, J. Greeley, K. More, C. Yu, Z. Liu, S. Kaya, D. Nordlund, H. Ogasawara, M. F. Toney and A. Nilsson, *Nat. Chem.*, 2010, **2**, 454–460.

203 D. Wang, Y. Yu, J. Zhu, S. Liu, D. A. Muller and H. D. Abruna, *Nano Lett.*, 2015, **15**, 1343–1348.

204 S. Koh and P. Strasser, *J. Am. Chem. Soc.*, 2007, **129**, 12624–12625.

205 S. Koh, N. Hahn, C. Yu and P. Strasser, *J. Electrochem. Soc.*, 2008, **155**, B1281–B1288.

206 J. Durst, M. Lopez-Haro, L. Dubau, M. Chatenet, Y. Soldo-Olivier, L. Guétaz, P. Bayle-Guillemaud and F. Maillard, *J. Phys. Chem. Lett.*, 2014, **5**, 434–439.

207 H. Kwon, M. K. Kabiraz, J. Park, A. Oh, H. Baik, S.-I. Choi and K. Lee, *Nano Lett.*, 2018, **18**, 2930–2936.

208 L. Wang, W. Gao, Z. Liu, Z. Zeng, Y. Liu, M. Giroux, M. Chi, G. Wang, J. Greeley, X. Pan and C. Wang, *ACS Catal.*, 2017, **8**, 35–42.

209 C. Wang, M. Chi, D. Li, D. Strmenik, D. van der Vliet, G. Wang, V. Komanicky, K. C. Chang, A. P. Paulikas, D. Tripkovic, J. Pearson, K. L. More, N. M. Markovic and V. R. Stamenkovic, *J. Am. Chem. Soc.*, 2011, **133**, 14396–14403.

210 L. Gan, M. Heggen, C. Cui and P. Strasser, *ACS Catal.*, 2015, **6**, 692–695.

211 S. Lu and Z. Zhuang, *J. Am. Chem. Soc.*, 2017, **139**, 5156–5163.

212 B. Han, C. E. Carlton, A. Kongkanand, R. S. Kukreja, B. R. Theobald, L. Gan, R. O’Malley, P. Strasser, F. T. Wagner and Y. Shao-Horn, *Energy Environ. Sci.*, 2015, **8**, 258–266.

213 M. Ahmadi, F. Behafarid, C. Cui, P. Strasser and B. R. Cuenya, *ACS Nano*, 2013, **7**, 9195–9204.

214 M. Ahmadi, C. Cui, H. Mistry, P. Strasser and B. Roldan Cuenya, *ACS Nano*, 2015, **9**, 10686–10694.

215 L. Wang and Y. Yamauchi, *J. Am. Chem. Soc.*, 2013, **135**, 16762–16765.

216 T. Fu, J. Fang, C. S. Wang and J. B. Zhao, *J. Mater. Chem. A*, 2016, **4**, 8803–8811.

217 H. Zhang, M. Jin, H. Liu, J. Wang, M. J. Kim, D. Yang, Z. Xie, J. Liu and Y. Xia, *ACS Nano*, 2011, **5**, 8212–8222.

218 C. Cui, L. Gan, M. Heggen, S. Rudi and P. Strasser, *Nat. Mater.*, 2013, **12**, 765–771.

219 Y. Xia, X. Xia and H. C. Peng, *J. Am. Chem. Soc.*, 2015, **137**, 7947–7966.

220 Z. Zhang, Z. Luo, B. Chen, C. Wei, J. Zhao, J. Chen, X. Zhang, Z. Lai, Z. Fan, C. Tan, M. Zhao, Q. Lu, B. Li, Y. Zong, C. Yan, G. Wang, Z. J. Xu and H. Zhang, *Adv. Mater.*, 2016, **28**, 8712–8717.

221 L. Han, H. Liu, P. L. Cui, Z. J. Peng, S. J. Zhang and J. Yang, *Sci. Rep.*, 2014, **4**, 6414.

222 J. Ding, X. Zhu, L. Bu, J. Yao, J. Guo, S. Guo and X. Huang, *Chem. Commun.*, 2015, **51**, 9722–9725.

223 M. Li, Z. Zhao, T. Cheng, A. Fortunelli, C. Y. Chen, R. Yu, Q. Zhang, L. Gu, B. V. Merinov, Z. Lin, E. Zhu, T. Yu, Q. Jia, J. Guo, L. Zhang, W. A. Goddard, 3rd, Y. Huang and X. Duan, *Science*, 2016, **354**, 1414–1419.

224 S. Luo and P. K. Shen, *ACS Nano*, 2016, **11**, 11946–11953.

225 E. Antolini, J. R. C. Salgado and E. R. Gonzalez, *J. Power Sources*, 2006, **160**, 957–968.

226 Y. Wu, D. Wang, G. Zhou, R. Yu, C. Chen and Y. Li, *J. Am. Chem. Soc.*, 2014, **136**, 11594–11597.

227 X. W. Yu and P. G. Pickup, *J. Power Sources*, 2008, **182**, 124–132.

228 A. S. Arico, S. Srinivasan and V. Antonucci, *Fuel Cells*, 2001, **1**, 133–161.

229 S. Wasmus and A. Küver, *J. Electroanal. Chem.*, 1999, **461**, 14–31.

230 J. N. Tiwari, R. N. Tiwari, G. Singh and K. S. Kim, *Nano Energy*, 2013, **2**, 553–578.

231 K. Jiang, Q. Shao, D. Zhao, L. Bu, J. Guo and X. Huang, *Adv. Funct. Mater.*, 2017, **27**, 1700830.

232 S. Luo, M. Tang, P. K. Shen and S. Ye, *Adv. Mater.*, 2017, **29**, 1601687.

233 L.-M. Lyu, Y.-C. Kao, D. A. Cullen, B. T. Snead, Y.-C. Chuang and C.-H. Kuo, *Chem. Mater.*, 2017, **29**, 5681–5692.

234 M. A. Ud Din, F. Saleem, B. Ni, Y. Yong and X. Wang, *Adv. Mater.*, 2017, **29**, 1604994.

235 S. I. Choi, S. Xie, M. Shao, J. H. Odell, N. Lu, H. C. Peng, L. Protsailo, S. Guerrero, J. Park, X. Xia, J. Wang, M. J. Kim and Y. Xia, *Nano Lett.*, 2013, **13**, 3420–3425.

236 N. Zhang, Y. Feng, X. Zhu, S. Guo, J. Guo and X. Huang, *Adv. Mater.*, 2017, **29**, 1603774.

237 L. Bu, Q. Shao, E. Bin, J. Guo, J. Yao and X. Huang, *J. Am. Chem. Soc.*, 2017, **139**, 9576–9582.

238 L. Luo, F. Zhu, R. Tian, L. Li, S. Shen, X. Yan and J. Zhang, *ACS Catal.*, 2017, **7**, 5420–5430.

239 C. Zhang, W. Sandorf and Z. Peng, *ACS Catal.*, 2015, **5**, 2296–2300.

240 X. Sun, K. Jiang, N. Zhang, S. Guo and X. Huang, *ACS Nano*, 2015, **9**, 7634–7640.

241 B. A. Lu, T. Sheng, N. Tian, Z. C. Zhang, C. Xiao, Z. M. Cao, H. B. Ma, Z. Y. Zhou and S. G. Sun, *Nano Energy*, 2017, **33**, 65–71.

242 X. Wang, S.-I. Choi, L. T. Roling, M. Luo, C. Ma, L. Zhang, M. Chi, J. Liu, Z. Xie, J. A. Herron, M. Mavrikakis and Y. Xia, *Nat. Commun.*, 2015, **6**, 7594.

243 J. Gu, G. X. Lan, Y. Y. Jiang, Y. S. Xu, W. Zhu, C. H. Jin and Y. W. Zhang, *Nano Res.*, 2015, **8**, 1480–1496.

244 J. H. Jang, E. Lee, J. Park, G. Kim, S. Hong and Y. U. Kwon, *Sci. Rep.*, 2013, **3**, 2872.

245 J. Park, L. Zhang, S.-I. Choi, L. T. Roling, N. Lu, J. A. Herron, S. Xie, J. Wang, M. J. Kim, M. Mavrikakis and Y. Xia, *ACS Nano*, 2015, **9**, 2635–2647.

246 X. Wang, M. Vara, M. Luo, H. Huang, A. Ruditskiy, J. Park, S. Bao, J. Liu, J. Howe, M. Chi, Z. Xie and Y. Xia, *J. Am. Chem. Soc.*, 2015, **137**, 15036–15042.

247 A. L. Strickler, A. Jackson and T. F. Jaramillo, *ACS Energy Lett.*, 2016, **2**, 244–249.

248 S. K. Kamarudin, F. Achmad and W. R. W. Daud, *Int. J. Hydrogen Energy*, 2009, **34**, 6902–6916.

249 A. Heinzel and V. M. Barragan, *J. Power Sources*, 1999, **84**, 70–74.

250 S. Gottesfeld and J. Pafford, *J. Electrochem. Soc.*, 1988, **135**, 2651–2652.

251 T. Tamaki, A. Yamauchi, T. Ito, H. Ohashi and T. Yamaguchi, *Fuel Cells*, 2011, **11**, 394–403.

252 P. Xinsheng, K. Kallum and C. Aicheng, *Nanotechnology*, 2007, **18**, 305605.

253 C. Dai, Y. Yang, Z. Zhao, A. Fisher, Z. Liu and D. Cheng, *Nanoscale*, 2017, **9**, 8945–8951.

254 S. J. Yoo, T.-Y. Jeon, K. S. Kim, T.-H. Lim and Y.-E. Sung, *Phys. Chem. Chem. Phys.*, 2010, **12**, 15240.

255 S. Şen, F. Şen and G. Gökağaç, *Phys. Chem. Chem. Phys.*, 2011, **13**, 6784.

256 S. Stolbov, M. A. Ortigoza, R. Adzic and T. S. Rahman, *J. Chem. Phys.*, 2009, **130**, 124714.

257 L. Guo, L. B. Huang, W. J. Jiang, Z. D. Wei, L. J. Wan and J. S. Hu, *J. Mater. Chem. A*, 2017, **5**, 9014–9021.

258 X. Q. Huang, Y. Chen, E. B. Zhu, Y. X. Xu, X. F. Duan and Y. Huang, *J. Mater. Chem. A*, 2013, **1**, 14449–14454.

259 H. H. Li, Q. Q. Fu, L. Xu, S. Y. Ma, Y. R. Zheng, X. J. Liu and S. H. Yu, *Energy Environ. Sci.*, 2017, **10**, 1751–1756.

260 B. Y. Xia, H. B. Wu, X. Wang and X. W. Lou, *J. Am. Chem. Soc.*, 2012, **134**, 13934–13937.

261 K. Jiang, H.-X. Zhang, S. Zou and W.-B. Cai, *Phys. Chem. Chem. Phys.*, 2014, **16**, 20360–20376.

262 V. Mazumder and S. Sun, *J. Am. Chem. Soc.*, 2009, **131**, 4588–4589.

263 X. W. Yu and P. G. Pickup, *J. Appl. Electrochem.*, 2011, **41**, 589–597.

264 S. Ha, R. Larsen and R. I. Masel, *J. Power Sources*, 2005, **144**, 28–34.

265 M. Jin, H. Zhang, Z. Xie and Y. Xia, *Energy Environ. Sci.*, 2012, **5**, 6352–6357.

266 V. Mazumder, M. Chi, M. N. Mankin, Y. Liu, O. Metin, D. Sun, K. L. More and S. Sun, *Nano Lett.*, 2012, **12**, 1102–1106.

267 Z. Yin, L. Lin and D. Ma, *Catal. Sci. Technol.*, 2014, **4**, 4116–4128.

268 Z. Wang, H. Wang, Z. Zhang, G. Yang, T. He, Y. Yin and M. Jin, *ACS Nano*, 2016, **11**, 163–170.

269 D. Liu, M. L. Xie, C. M. Wang, L. W. Liao, L. Qiu, J. Ma, H. Huang, R. Long, J. Jiang and Y. J. Xiong, *Nano Res.*, 2016, **9**, 1590–1599.

270 R. Li, H. Hao, W.-B. Cai, T. Huang and A. Yu, *Electrochem. Commun.*, 2010, **12**, 901–904.

271 M. J. Ren, J. Chen, Y. Li, H. F. Zhang, Z. Q. Zou, X. M. Li and H. Yang, *J. Power Sources*, 2014, **246**, 32–38.

272 D. Chen, P. Cui, H. Liu and J. Yang, *Electrochim. Acta*, 2015, **153**, 461–467.

273 D. Chen, P. Cui, H. He, H. Liu and J. Yang, *J. Power Sources*, 2014, **272**, 152–159.

274 H. Xiaoqing, Z. Huihui, G. Changyou, Z. Zhiyou and Z. Nanfeng, *Angew. Chem., Int. Ed.*, 2009, **48**, 4808–4812.

275 C. Spöri, J. T. H. Kwan, A. Bonakdarpour, D. P. Wilkinson and P. Strasser, *Angew. Chem., Int. Ed.*, 2017, **56**, 5994–6021.

276 L. Giordano, B. Han, M. Risch, W. T. Hong, R. R. Rao, K. A. Stoerzinger and Y. Shao-Horn, *Catal. Today*, 2016, **262**, 2–10.

277 S. M. Alia, S. Shulda, C. Ngo, S. Pylypenko and B. S. Pivovar, *ACS Catal.*, 2018, **8**, 2111–2120.

278 Y.-H. Fang and Z.-P. Liu, *J. Am. Chem. Soc.*, 2010, **132**, 18214–18222.

279 H.-S. Oh, H. N. Nong, T. Reier, A. Bergmann, M. Gliech, J. Ferreira de Araújo, E. Willinger, R. Schlögl, D. Teschner and P. Strasser, *J. Am. Chem. Soc.*, 2016, **138**, 12552–12563.

280 S. Cherevko, S. Geiger, O. Kasian, N. Kulyk, J.-P. Grote, A. Savan, B. R. Shrestha, S. Merzlikin, B. Breitbach, A. Ludwig and K. J. J. Mayrhofer, *Catal. Today*, 2016, **262**, 170–180.

281 X. Xu, F. Song and X. Hu, *Nat. Commun.*, 2016, **7**, 12324.

282 J. Xie, X. Zhang, H. Zhang, J. Zhang, S. Li, R. Wang, B. Pan and Y. Xie, *Adv. Mater.*, 2017, **29**, 1604765.

283 E. Antolini, *ACS Catal.*, 2014, **4**, 1426–1440.

284 D. Friebel, M. W. Louie, M. Bajdich, K. E. Sanwald, Y. Cai, A. M. Wise, M.-J. Cheng, D. Sokaras, T.-C. Weng, R. Alonso-Mori, R. C. Davis, J. R. Bargar, J. K. Nørskov, A. Nilsson and A. T. Bell, *J. Am. Chem. Soc.*, 2015, **137**, 1305–1313.

285 F. Song and X. Hu, *Nat. Commun.*, 2014, **5**, 4477.

286 B. Zhang, X. Zheng, O. Voznyy, R. Comin, M. Bajdich, M. Garcia-Melchor, L. Han, J. Xu, M. Liu, L. Zheng, F. P. Garcia de Arquer, C. T. Dinh, F. Fan, M. Yuan, E. Yassitepe, N. Chen, T. Regier, P. Liu, Y. Li, P. De Luna, A. Janmohamed, H. L. Xin, H. Yang, A. Vojvodic and E. H. Sargent, *Science*, 2016, **352**, 333–337.

287 K. A. Stoerzinger, L. Qiao, M. D. Biegalski and Y. Shao-Horn, *J. Phys. Chem. Lett.*, 2014, **5**, 1636–1641.

288 L. C. Seitz, C. F. Dickens, K. Nishio, Y. Hikita, J. Montoya, A. Doyle, C. Kirk, A. Vojvodic, H. Y. Hwang, J. K. Nørskov and T. F. Jaramillo, *Science*, 2016, **353**, 1011–1014.

289 Y. Ping, R. J. Nielsen and W. A. Goddard, *J. Am. Chem. Soc.*, 2017, **139**, 149–155.

290 M. Escudero-Escribano, A. F. Pedersen, E. A. Paoli, R. Frydendal, D. Friebel, P. Malacrida, J. Rossmeisl, I. E. L. Stephens and I. Chorkendorff, *J. Phys. Chem. B*, 2018, **122**, 947–955.

291 Y. Lee, J. Suntivich, K. J. May, E. E. Perry and Y. Shao-Horn, *J. Phys. Chem. Lett.*, 2012, **3**, 399–404.

292 C. Wang, Y. Sui, M. Xu, C. Liu, G. Xiao and B. Zou, *ACS Sustainable Chem. Eng.*, 2017, **5**, 9787–9792.

293 H. N. Nong, H.-S. Oh, T. Reier, E. Willinger, M.-G. Willinger, V. Petkov, D. Teschner and P. Strasser, *Angew. Chem., Int. Ed.*, 2015, **54**, 2975–2979.

294 H. Jin, Y. Hong, J. Yoon, A. Oh, N. K. Chaudhari, H. Baik, S. H. Joo and K. Lee, *Nano Energy*, 2017, **42**, 17–25.

295 C. Wang, Y. M. Sui, G. J. Xiao, X. Y. Yang, Y. J. Wei, G. T. Zou and B. Zou, *J. Mater. Chem. A*, 2015, **3**, 19669–19673.

296 J. Feng, F. Lv, W. Zhang, P. Li, K. Wang, C. Yang, B. Wang, Y. Yang, J. Zhou, F. Lin, G.-C. Wang and S. Guo, *Adv. Mater.*, 2017, **29**, 1703798.

297 T. Kwon, H. Hwang, Y. J. Sa, J. Park, H. Baik, S. H. Joo and K. Lee, *Adv. Funct. Mater.*, 2017, **27**, 1604688.

298 J. Park, Y. J. Sa, H. Baik, T. Kwon, S. H. Joo and K. Lee, *ACS Nano*, 2017, **11**, 5500–5509.

299 J. Lim, S. Yang, C. Kim, C.-W. Roh, Y. Kwon, Y.-T. Kim and H. Lee, *Chem. Commun.*, 2016, **52**, 5641–5644.

300 W. Sun, Y. Song, X.-Q. Gong, L.-m. Cao and J. Yang, *Chem. Sci.*, 2015, **6**, 4993–4999.

301 H.-S. Oh, H. N. Nong, T. Reier, M. Gliech and P. Strasser, *Chem. Sci.*, 2015, **6**, 3321–3328.

302 H. N. Nong, L. Gan, E. Willinger, D. Teschner and P. Strasser, *Chem. Sci.*, 2014, **5**, 2955–2963.

303 P. Lettenmeier, L. Wang, U. Golla-Schindler, P. Gazdzicki, N. A. Cañas, M. Handl, R. Hiesgen, S. S. Hosseiny, A. S. Gago and K. A. Friedrich, *Angew. Chem., Int. Ed.*, 2016, **55**, 742–746.

304 A. B. Laursen, K. R. Patraju, M. J. Whitaker, M. Retuerto, T. Sarkar, N. Yao, K. V. Ramanujachary, M. Greenblatt and G. C. Dismukes, *Energy Environ. Sci.*, 2015, **8**, 1027–1034.

305 J. Kibsgaard, T. F. Jaramillo and F. Besenbacher, *Nat. Chem.*, 2014, **6**, 248.

306 J. Kibsgaard, Z. Chen, B. N. Reinecke and T. F. Jaramillo, *Nat. Mater.*, 2012, **11**, 963.

307 M. A. Lukowski, A. S. Daniel, F. Meng, A. Forticaux, L. Li and S. Jin, *J. Am. Chem. Soc.*, 2013, **135**, 10274–10277.

308 L. Lin, N. Miao, Y. Wen, S. Zhang, P. Ghosez, Z. Sun and D. A. Allwood, *ACS Nano*, 2016, **10**, 8929–8937.

309 B. Seo, G. Y. Jung, Y. J. Sa, H. Y. Jeong, J. Y. Cheon, J. H. Lee, H. Y. Kim, J. C. Kim, H. S. Shin, S. K. Kwak and S. H. Joo, *ACS Nano*, 2015, **9**, 3728–3739.

310 D. Yoon, B. Seo, J. Lee, K. S. Nam, B. Kim, S. Park, H. Baik, S. H. Joo and K. Lee, *Energy Environ. Sci.*, 2016, **9**, 850–856.

311 M. Liu and J. Li, *ACS Appl. Mater. Interfaces*, 2016, **8**, 2158–2165.

312 E. J. Popczun, C. G. Read, C. W. Roske, N. S. Lewis and R. E. Schaak, *Angew. Chem., Int. Ed.*, 2014, **53**, 5427–5430.

313 J. F. Callejas, J. M. McEnaney, C. G. Read, J. C. Crompton, A. J. Biacchi, E. J. Popczun, T. R. Gordon, N. S. Lewis and R. E. Schaak, *ACS Nano*, 2014, **8**, 11101–11107.

314 J. Xu, J. Cui, C. Guo, Z. Zhao, R. Jiang, S. Xu, Z. Zhuang, Y. Huang, L. Wang and Y. Li, *Angew. Chem., Int. Ed.*, 2016, **55**, 6502–6505.

315 C. Zhang, Y. Liu, Y. Chang, Y. Lu, S. Zhao, D. Xu, Z. Dai, M. Han and J. Bao, *ACS Appl. Mater. Interfaces*, 2017, **9**, 17326–17336.

316 D. Yoon, J. Lee, B. Seo, B. Kim, H. Baik, S. H. Joo and K. Lee, *Small*, 2017, **13**, 1700052.

317 Z. Cao, H. Li, C. Zhan, J. Zhang, W. Wang, B. Xu, F. Lu, Y. Jiang, Z. Xie and L. Zheng, *Nanoscale*, 2018, **10**, 5072–5077.

318 M. Escudero-Escribano, P. Malacrida, M. H. Hansen, U. G. Vej-Hansen, A. Velazquez-Palenzuela, V. Tripkovic, J. Schiotz, J. Rossmeisl, I. E. Stephens and I. Chorkendorff, *Science*, 2016, **352**, 73–76.

319 K. J. J. Mayrhofer, J. C. Meier, S. J. Ashton, G. K. H. Wiberg, F. Kraus, M. Hanzlik and M. Arenz, *Electrochem. Commun.*, 2008, **10**, 1144–1147.

320 T. Reier, M. Oezaslan and P. Strasser, *ACS Catal.*, 2012, **2**, 1765–1772.

321 P. Jovanovic, N. Hodnik, F. Ruiz-Zepeda, I. Arcon, B. Jozinovic, M. Zorko, M. Bele, M. Sala, V. S. Selih, S. Hocevar and M. Gaberscek, *J. Am. Chem. Soc.*, 2017, **139**, 12837–12846.

322 X. Huang, Z. Zhao, L. Cao, Y. Chen, E. Zhu, Z. Lin, M. Li, A. Yan, A. Zettl, Y. M. Wang, X. Duan, T. Mueller and Y. Huang, *Science*, 2015, **348**, 1230–1234.

323 D. Mocatta, G. Cohen, J. Schattner, O. Millo, E. Rabani and U. Banin, *Science*, 2011, **332**, 77–81.

324 L. Cao and T. Mueller, *Nano Lett.*, 2016, **16**, 7748–7754.

325 F. Saleem, B. Ni, Y. Yong, L. Gu and X. Wang, *Small*, 2016, **12**, 5261–5268.

326 L. Bu, N. Zhang, S. Guo, X. Zhang, J. Li, J. Yao, T. Wu, G. Lu, J. Y. Ma, D. Su and X. Huang, *Science*, 2016, **354**, 1410–1414.

327 S. Xie, S.-I. Choi, N. Lu, L. T. Roling, J. A. Herron, L. Zhang, J. Park, J. Wang, M. J. Kim, Z. Xie, M. Mavrikakis and Y. Xia, *Nano Lett.*, 2014, **14**, 3570–3576.

328 A. Mahmood, N. Xie, M. A. Ud Din, F. Saleem, H. Lin and X. Wang, *Chem. Sci.*, 2017, **8**, 4292–4298.

329 C. W. Han, T. Choksi, C. Milligan, P. Majumdar, M. Manto, Y. Cui, X. Sang, R. R. Unocic, D. Zemlyanov, C. Wang, F. H. Ribeiro, J. Greeley and V. Ortalan, *Nano Lett.*, 2017, **17**, 4576–4582.

330 T. Avanesian, S. Dai, M. J. Kale, G. W. Graham, X. Pan and P. Christopher, *J. Am. Chem. Soc.*, 2017, **139**, 4551–4558.

331 A. P. LaGrow, D. C. Lloyd, P. L. Gai and E. D. Boyes, *Chem. Mater.*, 2018, **30**, 197–203.

332 M. Vara, L. T. Roling, X. Wang, A. O. Elnabawy, Z. D. Hood, M. Chi, M. Mavrikakis and Y. Xia, *ACS Nano*, 2017, **11**, 4571–4581.

333 L. Dubau, M. Lopez-Haro, J. Durst and F. Maillard, *Catal. Today*, 2016, **262**, 146–154.

334 L. Dubau, J. Nelayah, T. Asset, R. Chattot and F. Maillard, *ACS Catal.*, 2017, **7**, 3072–3081.

335 J. Snyder and J. Erlebacher, *ECS Trans.*, 2011, **41**, 1021–1030.

336 J. Snyder, T. Fujita, M. W. Chen and J. Erlebacher, *Nat. Mater.*, 2010, **9**, 904.